Atom lithography : creating patterned magnetic layers

Atom lithography:
Creating patterned magnetic layers

Proefschrift

ter verkrijging van de graad van doctor aan de
Technische Universiteit Eindhoven, op gezag van
de rector magnificus, prof.dr.ir. C.J. van Duijn,
voor een commissie aangewezen door het College van
Promoties in het openbaar te verdedigen
op maandag 23 januari 2012 om 16.00 uur

door

Thijs Meijer

geboren te Kerkrade

Dit proefschrift is goedgekeurd door de promotor:

prof.dr. K.A.H. van Leeuwen

Copromotor:
dr.ir. E.J.D. Vredenbregt

A catalogue record is available from the Eindhoven University of Technology Library

ISBN: 978-90-386-3093-9

The work described in this thesis has been carried out in the Coherence and Quantum Technology group at the Eindhoven University of Technology, Department of Applied Physics and is part of the research programme of the Foundation for Fundamental Research on Matter (FOM), which is part of the Netherlands Organisation for Scientific Research (NWO).

Summary

Atom lithography: creating patterned magnetic layers

Atom lithography is a technique to structure layers of atoms during deposition, using interactions of near-resonant light fields with neutral atoms. The basic scheme uses a standing wave light field, aligned just above a substrate, while a beam of atoms impinges perpendicularly on the standing wave light field. The interaction of the light field and the atoms focuses the atoms towards the crests or troughs of the standing wave intensity, dependent on the tuning of the light field. The focused atoms are subsequently deposited on the substrate, resulting in an array of lines, whose periodicity is determined by the wavelength of the light field. The standing wave light field can therefore be seen as an array of lenses, focusing the atom beam into an array of lines. The first experiments on atom lithography were performed in the 1990s with sodium and chromium. In this thesis experiments with iron are described, which is a magnetic element and thus allows for the creation of magnetic nanostructures.

To focus atom beams into structures using atom lithography, well-colimated atom beams are required. The most common technique to create collimated atom beams is transverse laser cooling, but iron has no closed optical transition suitable for laser cooling. Fortunately Smeets and Te Sligte found that even then atom lithography of iron is possible. If the standing wave light field is considered to be an array of lenses, the focusing of the atom beam on a single lens is determined by the local collimation of the atom beam at that position. This local collimation is determined by the geometry of the beam source and the distance of the beam source to the standing wave lens. Using a small beam source (e.g. 1 mm diameter) positioned far from the standing wave (e.g. 1 m), the geometrically collimated atom beam is suitable for atom lithography.

Chapter 3 shows what the implications of geometric collimation are on the structure formation in atom lithography. The geometric effects that locally collimate the atom beam on the sample also introduce local offset angles of the atom beam with respect to the focusing light field. Structure formation has been observed with lines of up to 7 nm high on a background layer of 15 nm average height, over areas of up to 400 μm $\times$ 6 mm. This indicates that the offset angles can vary over an 8 mrad range, which is more than an order of magnitude larger than the local angle of collimation. The offset angle influence the local geometry of the deposited structures: an increasing offset angle decreases the local line height, increases the width and creates a skewness in the local line shape.

The local geometry of the lines has been modelled with a Monte Carlo particle tracking model and the results were compared to experiments. It was found that the highest and narrowest lines suffer from significant broadening due to surface diffusion

in experiments, limiting the achievable structure width of iron on SiOx samples to about 80 nm. We have also found that in atom lithography without laser cooling, each standing wave lens is effectively imaging the source geometry onto the substrate. We therefore propose using structured atom beam sources to image more complex patterns on sub-wavelength scales in a parallel way.

The reason to use iron in atom lithography, is the option to create magnetic nanostructures. However, in previous experiments no clear magnetic signature of the atom lithographic structuring of iron was found. Therefore in Chapter 4 firstly the magnetic properties of unstructured layers of iron (Fe), nickel (Ni) and Fe_xNi_{1-x} are investigated. These layers are all ferromagnetic, but with a reduced magnetic moment compared to bulk values due to contaminations and crystal growth effects. As a reference for periodic atom lithography structures, periodic line structures are created with interference lithography in a polymer layer and onto these structures thin layers of Fe_xNi_{1-x} are shadow deposited, thereby creating a layer periodically modulated in both height and elemental composition. This periodic modulation in composition has been observed with SEM-EDX on sub-micron scales. The structures showed a clear magnetic anisotropy with an easy axis along the direction of the lines, in accordance with expectations.

In Chapter 5, the magnetic properties of atom lithographic iron line structures are presented. Using MOKE microscopy, direct comparison of structured and unstructured parts of a sample is possible, which allows for the observation of clear magnetic signatures due to the atom lithographic structuring. In layers of an average thickness of about 15 nm, no anisotropy is induced by the line structures, while a magnetic easy axis along the direction of the lines is expected. The line structures introduce an isotropic increase in the coercivity of the layers, indicating that the line structures can be considered as isotropic corrugations instead of directional line structures. For layers of 30 nm average thickness and thus higher line structures, a clear magnetic anisotropy is observed for the highest line structures. This anisotropy can be seen as a magnetic easy axis along the direction of the lines, as expected for line structures. However, we also observe a sharp increase in coercivity for applied fields perpendicular to the lines. This phenomenon is intriguing and may be explained by a pinning of head-to-head domain walls along the direction of the lines.

In Chapter 5, we also report on the first results of co-deposition of Fe_xNi_{1-x}, where the Fe is structured into lines using atom lithography, while the Ni is deposited uniformly, thereby creating an alloy of modulating composition. Magnetic analysis of these structures indicates that these structures are anisotropic, both the coercivity and the shape of domain walls is dependent on the angle of the applied field relative to the line structures.

Finally in Chapter 6, we investigate the possibilities to focus a thermal beam of atoms into a single 100 nm spot using light fields, thereby creating a nanopencil suitable for deposition of nanostructures. A Monte Carlo particle tracking program was developed to model the all optical focusing or funneling of 10 μm sized atom beams to a 100 nm spot. This model included effects of initial beam divergence, magnetic

substructure, laser cooling, and spontaneous as well as stimulated diffusion and it was applied to a number of promising light field configurations. The best results obtained for experimentally realistic settings are a beam focused to a full width at half maximum of *FWHM* = 0.55 μm in a blue detuned hollow beam where atoms are focused towards the dark center, or a *FWHM* = 0.31 μm in a red detuned axicon light field, where atoms are focused towards the maximum intensity at the heart line. However, in the latter case the focused beam has a flux only 25 times larger than the background flux, which is unpractical for applications. The limiting factors of all schemes are heating due to stimulated diffusion and the limited interaction time available for a thermal beam of atoms. A nanopencil could be possible if it were based on the focussing of a slow and / or monochromatic atom beam, but this would seriously complicate the practical application of such a device.

About the author

Thijs Meijer was born on 19 december 1980 in Kerkrade, the Netherlands. After finishing from the Christiaan Huygens College (VWO) in Eindhoven in 1999, he started the study Applied Physics at the Eindhoven University of Technology. As part of this study he did an internship at the School of Physics of the University of Melbourne in Australia under guidance of prof.dr. R.E. Scholten. During his studies he was also active in various student groups, e.g., as member of the board of the students association for Applied Physics "J.D. van der Waals", as member of the board of korfball club "ESKV Attila" and as member of the University Counsil.

He received his Master's degree in 2006. His Master's thesis was on "Optical properties of inkjet printed and μ-transfer printed structures of reactive mesogens" at the faculty of Applied Chemistry under guidance of prof. dr. C.W.M. Bastiaansen. This research formed part of the basis technology of Validus Technologies B.V., a spin-off of the Eindhoven University of Technology in the field of developing and commercializing inkjet printable liquid crystalline based security features. Thijs was co-founder and Chief Science Officer of Validus Technologies from 2007 until 2011. In 2010 he also obtained a Master in Business Innovation of the TIAS-Nimbas business school.

In 2006 he started a Ph.D. with the Foundation for Fundamental Research (FOM) on the project "New directions in atom lithography" under guidance of prof.dr. K.A.H. van Leeuwen and dr.ir. E.J.D. Vredenbregt in the Coherence and Quantum Technology group at the faculty of Applied Physics. The result of these studies are described in this thesis.

Acknowledgements

After several years of working on atom lithography, this thesis has now nearly reached its completion, needing only these words of gratitude to be finished. First of all I would like to thank you, the reader of this text, for your interest, but most of all I would like to spend this page to thank those that have made it possible for me to achieve this result and who have supported me all these years while working at the Eindhoven University of Technology.

I would like to thank the FOM, who have both funded my project allowed me to enter the academic world, but who also were always very supportive about my work for Validus Technology. However, the real scientific support came most of all from my promotor, Ton van Leeuwen and co-promotor, Edgar Vredenbregt, thank you for the many hours of discussion on atom lithography and Edgar, thank you for your practical hands-on help on many occasions. Of course I would also like to thank the other member of the reading committee, Wim Vassen, Markus Oberthaler and Bert Koopmans, whom I would like to thank especially for the discussions on magnetism.

During the project I also had the support of a wonderfull Dutch-Ozzie connection: Corine, thank you for your help on the deposition sources and for creating the link to Australia. Josh, your support and especially your infinite patience with the fiber coupling have always been a great example that any laser setup will work eventually! Furthermore I would like to thank the students that worked with me: Jan-Pieter, Taco, Remy, Joep and Cornee. I hope you all enjoyed working with me, you have surely always been inspiring to me!

The scientific work in this thesis would have never been possible without the technical support of both the technicians of the group: Louis van Moll, Jolanda van de Ven, Eddy Rietman, Harry van Doorn, Ad Kemper and Iman Koole. I would also like to mention specifically Frans van Setten for his help with the electronic control systems, it significantly improved the quality of the setup!

The work of this thesis is of course not only on atom lithography, but also has elements of surface characterisation magnetism and interference lithography. Fortunately I had the chance to work with the M2N group for the surface characterisation. Martijn Kemerink, thank you for letting me use your AFM equipment and I would also like to thank Simon Mathijssen and Erik Roeling for their help with the AFM and the wonderful discussions on atom lithography and many other things. At the FNA group I had the opportunity to do the magnetic characterisation of the samples and have discussions on the magnetic properties. Beatriz Barcones Campo, Reinoud Lavrijssen, Mark Hoeijmakers and especially Jeroen Franken thank you very much for your help! Finally I would also like to thank An Prenen at the Chemistry department for her help in creating samples with interference lithography.

Off course the work of a Ph.D. is not only in direct scientific cooperation, but also in working together in a group and at the CQT group I had wonderfull Ph.D. colleagues:

Gabriel, Stefan, Nicola, Adam, Xavier, Kenian, Maarten, Merijn, Thijs, Willem, Walter, Peter en Peter, Wouter, Maikel and Rick. Stefan, Nicola, you were perfect room mates, always in for either a joke or a good discussion; Gabriel, thank you for getting me to Amsterdam more often; Rick thanks fro all the great hiking trips; and all of you: thank you for the good times and I wish you all the very best! This wish is also extended to the permanent staff of CQT: Jom, Servaas, Seth, Peter, Jaap and Betty. Betty, thank you for all the practical help on ever so many things!

Now I come to those that may have not added so much to my academic career, but certainly to my experiences of the last years. The times with Validus Technologies, starting up a company, consisted often of trial-and-error experiments, but have most of all shown me the life outside academia. Nico, Robert, I am very happy that at my graduation you will be my paranymphs, our cooperation has been a great experience. Also to all others that have worked at Validus, it was nice to work with you! Xiao and Kenny, it was a pleasure coaching your graduation projects and I'm happy to see that you have both gave your career a good start.

Now at the end I would like to thank all my friends, at Rust Roest, Attila and elsewhere, who have had to listen to some occasional physics frustration but still allowed me to retain a life outside of work. I would like to thank my family, my parents, Jan, Judith, Irene, Roland and Maud: thank you for being there for me. Also to the Koekoek family, thank you for making me feel always at home! En tenslotte is er nog maar een over, Mariëtte, bedankt voor al je ondersteuning, je scherpe observaties en heldere commentaar, maar bovenal voor je liefde.

Thijs Meijer, Eindhoven, december 2011

Contents

Chapter 1

Introduction

1.1 Light and matter.

The view we have today of matter and light was established at the end of the 19th and the start of the 20th century and it describes matter and light down to the nanoscale. However, already in the Roman Empire did artisans create optical phenomena caused by gold nanoparticles dispersed in glass, creating wonderful colour effects in the glass [1]. These craftsmen thus already created optical effects on a nanometer scale, long before a proper knowledge of the nature of light or matter on these scales was developed.

Our current understanding of light is based on the fact that light has a dual character of both a wave and a particle. In Maxwell's equations light is described as a wave, while Planck and Einstein developed the view that light is composed of particles with a quantized character, photons. This quantization of the light field formed the basis for the development of quantum mechanics. In quantum mechanics all particles, such as atoms, or electrons also have a wave character. Louis de Broglie derived the wavelength of particles and he found that the wave character of electrons orbiting an atomic nucleus only allowed for discrete orbitals in the Bohr model. As an electron can only be in specific orbitals, which correspond to specific energy levels, a change in orbital can take place when a photon is absorbed or emitted, whose energy (and corresponding wavelength) matches the energy difference of the levels of the electron. This explained why atoms absorb or emit photons of specific wavelengths that are resonant with an atomic transition.

In 1933 Otto Frisch performed an experiment that showed that the absorption of single photons can have a mechanical effect on single atoms [2]. A schematic of the experiment is shown in Figure 1.1. Frisch created a beam of neutral sodium atoms in a vacuum, that was collimated using slits into a beam of a few mm height and some tens of μm wide. This beam of sodium atoms was then illuminated from the side by a sodium lamp, emitting light of 589 nm at the D-line of sodium. Moving neutral sodium atoms absorb a photon and thereby both the energy and the momentum of the photon, deflecting the atom from its original path. During illumination about one in three atoms could absorb a photon and indeed one third of the atom beam was deflected. Although the deflection found in this experiment was only 0.01 mm, it did show the basic concept of the manipulation of atom beams with light fields.

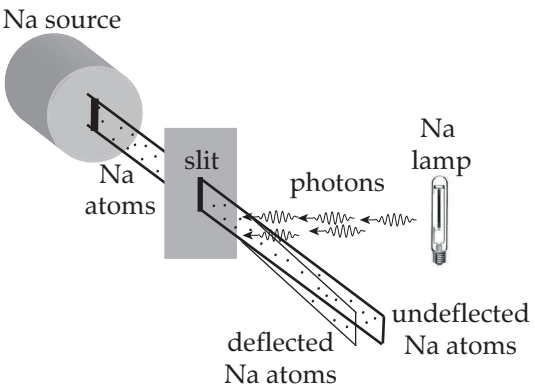

Figure 1.1: *Schematic of the experiment by Frisch [2] in 1933 to deflect a beam of sodium (Na) atoms by the absorption of a single photon and its momentum.*

The results obtained by Frisch can be understood in classic mechanics as a transfer of momentum of a photon to an atom. Since then, the development of high power, coherent light sources in the form of lasers allowed for the development of atom optics, a field of physics that studies the interactions of light and atoms, often in a quantum-mechanical framework. It has led to many discoveries ranging from laser cooling of ions [3] and atoms [4] and the magneto-optical trapping of atoms [5] to Bose Einstein condensates [6] and also to atom lithography [7], the latter being the subject of this thesis.

1.2 Atom lithography

Atom lithography is a technique that uses interactions of light and atoms to create patterned atomic depositions. A schematic representation is shown in Figure 1.2. Here a beam of neutral atoms passes through a standing wave light field located just above the substrate. The light field is near resonant with an optical transition, creating an induced dipole moment in the atoms. Such dipoles will interact with the field, leading to a dipolar interaction energy given by

$$U_{dip} = -\frac{\alpha(\omega)}{2\varepsilon_0 c} I, \tag{1.1}$$

where $\alpha(\omega)$ is the dynamic polarisability of the atom at frequency ω of the light, I is the intensity of the light field and ε_0 and c are the vacuum permittivity and the speed of light. The standing wave light field shown in Figure 1.2 has a periodic intensity. It thus forms a periodic potential for atoms, focusing the atom beam into lines spaced by $\lambda/2$ defined by the wavelength of the light field, λ. The light field should be tuned close to resonance so that $\alpha(\omega)$ is non-zero, but not too close to resonance where spontaneous emission will occur. As the sign of $\alpha(\omega)$ is dependent on the detuning

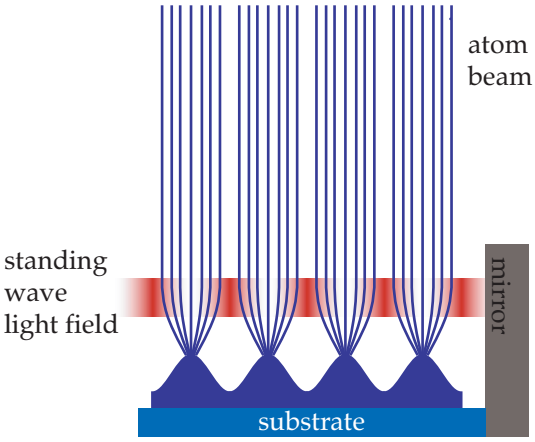

Figure 1.2: *Schematic overview of atom lithography: a near resonant standing wave light field forms an array of lenses focusing an atom beam into lines on a substrate spaced by* $\lambda/2$.

from resonance, $\Delta = \omega - \omega_0$, where ω_0 is the resonant frequency of the atom, a light field with $\Delta > 0$ will focus the atoms to the low light intensity regions, while $\Delta < 0$ will focus the atoms to the high intensity regions.

Atom lithography has several advantages compared to other techniques to create structured depositions. In atom lithography the optical diffraction limit is not the limiting factor because the atomic de Broglie wavelength is below a nanometer. A second advantage is that atom lithography is a single step deposition process, which in principle allows for the production of very clean structures that are not contaminated during other process steps. Furthermore the structures can be made extremely periodic, as the standing wave pattern of the light field is reproduced. In this thesis we use this technique to create periodic structures in thin Fe films. Another unique option of atom lithography is co-deposition, where two atomic species are deposited, only one of which is focused by a near resonant light field while the other is deposited uniformly. This allows for local changes in composition of an alloy. Options for co-deposition are explored in Chapter 5 of this thesis.

The light field configuration in atom lithography defines the resulting pattern: a single standing wave gives lines spaced by $\lambda/2$. More complex patterns have been realised such as rectangular grids [8], hexagonal arrays [9] or quasi-periodic patterns [10]. The quantum mechanical nature of the interaction of neutral atoms and resonant light even allowed for the creation of structures of $\lambda/4$ [11] or $\lambda/8$ periodicity [12]. However, for applications the restriction of periodic patterns is highly limiting. Mützel et al. performed two experiments which can allow for non-periodic patterns. First they used holographic optical patterns in atom lithography experiments [13]. Holography can be used to create random optical patterns, even though the creation of arbitrary patterns is technologically challenging. A limit of this scheme is the requirement of light field gradients for atom lithographic focusing. The distance over which an atom can be displaced in atom lithographic focusing is restricted by the

distance over which a sufficiently large intensity gradient can be maintained, while the maximum intensity is experimentally limited. This restricts the use of holographic optical patterns in atom lithography. In a second experiment an "atom pencil" was created [14], where magneto-optical forces were used to create a single 45 μm sized atom beam, which was collimated using mechanical apertures to a single 280 nm sized atom beam, which could write arbitrary patterns. In Chapter 6 of this thesis we extend this idea by exploring options to create sub-100 nm sized atom beams without the use of mechanical apertures, using only light to focus atoms and thus create a true "nanopencil" for atoms in a realistic experimental setting.

Various atomic species have been used in atom lithography. The first experiments were performed by Timp et al. [7] using sodium in 1992 and by McClelland et al. [15] using chromium in 1993. Atom lithography was also performed using Al [16], Yb [17], and Fe [18, 19]. For all these materials so-called direct deposition was used, where atoms are deposited to form structures. Atom lithography can also be used to pattern a resist layer. In this case atoms are focussed onto the resist layer thereby locally damaging the resist. This has been done with metastable atoms which have a high internal energy, such as Ar^*[20], Ne^*[21], or He^*[22] and with atoms that are chemically active such as ground state Cs [23]. However, direct deposition of chromium is the most common method in atom lithography. A major advantage of chromium is that it is stable in air, so that structures can be studied ex vacuo. Another advantage of chromium is that it has a strong, almost perfectly closed optical transition at a wavelength $\lambda = 425$ nm, which is accessible with tunable laser systems. This allows for the use of laser cooling before focusing the atom beam with atom lithography.

Laser cooling is a technique that can collimate a divergent atom beam, thereby increasing the flux and creating a collimated beam which is more suitable for focusing in atom lithography. In the experiment of Frisch it was already shown that momentum can be transferred from a photon to an atom. If a two level atom is continuously irradiated by a near resonant laser, it will absorb photons and spontaneously re-emit these photons at a scattering rate $\dot{N}$. The spontaneous emission is isotropic, therefore the emission has no average momentum transfer. If each absorbed photon carries a momentum of $\hbar \overrightarrow{k}$, where $\vec{k}$ is the wave vector with $\left|\vec{k}\right| = 2\pi/\lambda$, a scattering force of $\left\langle \overrightarrow{F} \right\rangle = \dot{N}\hbar \overrightarrow{k}$ is exerted on the atom. If two counter-propagating laser beams are applied to a stationary atom, the two scattering forces on the atom cancel exactly. However, if the atom has a velocity $\overrightarrow{v}$ the laser frequencies are Doppler shifted leading to an effective detuning $\Delta - \overrightarrow{k} \cdot \overrightarrow{v}$, so that the scattering forces are velocity dependent. For both laser beams detuned by $\Delta = -\Gamma/2$, the sum force is always opposed to the velocity, so that this scheme can cool the atom in the direction of the lasers. This Doppler cooling process is limited by the random recoils of the emitted photons, giving a minimum temperature of $T_D = \hbar\Gamma/(2k_B)$, the Doppler temperature. For a beam of Fe atoms, the element used in this thesis, transverse laser cooling to T_D equals cooling to a transverse velocity spread of 0.1 m/s. This means that thermal Fe beams can be well collimated as their forward velocity is typically 10^3 m/s.

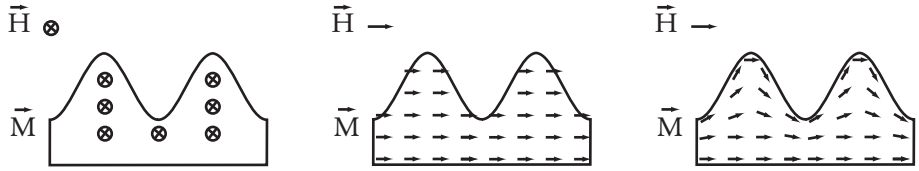

Figure 1.3: *Schematic representation of magnetisation of atom lithographic line structures on a background. Left: Applied field and uniform magnetisation directed into the plane of the paper. Center: Applied field and uniform magnetisation in the plane of the paper, inducing magnetic surface poles. Right: Applied field in the plane of the paper, with magnetisation forced along the surface structure so that* $\nabla \cdot \vec{M} \neq 0$ *in the structure.*

The basis of laser cooling is repeated absorption and emission of photons, which is only possible for atomic species with a closed transition. However, Fe does not have a suitable closed transition. The transition most suitable for both atom lithographic focusing and laser cooling, is the ${}^5D_4 \rightarrow {}^5F_5$ transition, at $\lambda = 372$ nm. This transition is not completely closed, because atoms can decay to metastable ${}^5F_5$, ${}^5F_4$ or ${}^3F_4$ states with a combined probability of 1/244. Atom lithography and laser cooling on this transition have been observed [18]. Unfortunately laser cooling was shown to lead to a negligible increase in useful flux of ground-state atoms [24]. Iron atoms that decay to other states than the ground state during laser cooling do not interact with the focusing light field and are deposited as a background layer, severely limiting the achievable contrast. Smeets [25] and Te Sligte [26] showed that atom lithography of iron is possible without laser cooling if the atom beam source is small and positioned far away from the sample. In chapter 3 of this thesis we expand on this idea by a performing a detailed investigation of the topographical structure of Fe depositions created by this geometric cooling technique.

1.3 Magnetism of ferromagnetic nanostructures

The main subject of this thesis is atom lithography of iron, which is a ferromagnetic element so that magnetic nanostructures are created. The applications of magnetism in magnetic data storage have driven an enormous research effort towards a better fundamental understanding of magnetism on small scales. In this section we will not provide a complete overview of magnetism, of which many overviews are available [27, 28], but some key aspects are presented. In Chapters 4 and 5 we present an experimental study of the properties of magnetic thin films.

The atom lithographic iron structures presented in this thesis can be schematically represented as infinite parallel lines on top of a background layer. The presence of the lines on a background can have significant effects on the magnetisation $\vec{M}$ of this structure. In Figure 1.3 a schematic cross-section of the lines is shown when an external field $\vec{H}$ is applied parallel (left) or perpendicular (centre and right) to the

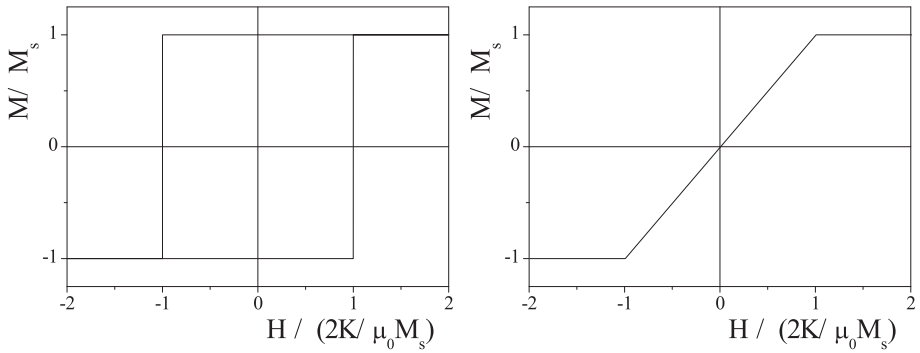

Figure 1.4: *Calculated hysteresis curves in the Stoner Wohlfahrt model, for $\vec{H}$ along the easy axis $\Theta = 0°$(left) or $\vec{H}$ along the hard axis $\Theta = 90°$*

line direction. If $\vec{H}$ is parallel to the line direction the energetically favorable magnetisation is that $\vec{M}$ is uniform throughout the sample and parallel to both $\vec{H}$ and all surfaces of the structure. If $\vec{H}$ is perpendicular to the line direction, $\vec{M}$ can be aligned uniformly throughout the sample as shown in the centre of Figure 1.3, but then the surface magnetisation is not parallel to the surface, inducing magnetic surface charges. In a situation where $\vec{M}$ is aligned parallel to all surfaces, schematically shown on the right of Figure 1.3, $\nabla \cdot \vec{M} \neq 0$ in the bulk, so that this configuration has magnetic volume charges. Both configurations with $\vec{H}$ perpendicular to the line direction have magnetic charges and therefore also have an additional magnetostatic energy compared to the configuration of $\vec{H}$ parallel to the line direction. This is the basis for shape anisotropy, which is an anisotropy of the magnetic properties due to the shape of a magnetic element. A shape anisotropy can be an input for a Stoner-Wohlfahrt model [27].

The Stoner-Wohlfahrt model is a model to explain micromagnetic behavior. The basic assumption is that the magnetization $\vec{M}$ is uniform throughout the system with constant size M_s and that there is a coherent rotation of $\vec{M}$ during magnetization reversal. This means that during magnetization reversal the exchange energy is constant so that the energy of the system is determined by the anisotropy energy. Anisotropies can be induced by e.g., shape or magneto-crystalline effects. If only a uniaxial shape anisotropy due to the line structures is included, the energy per unit volume E/V of the system is given by:

$$\frac{E}{V} = K \sin^2(\theta) - \mu_0 M_s H \cos(\theta - \Theta), \tag{1.2}$$

where θ and Θ are the angle between the line direction and respectively $\vec{M}$ and $\vec{H}$. K is the effective shape anisotropy energy per unit volume [27].

If $H = 0$ in Equation 1.2, the energy minimum is at $\theta = 0°$ or $\theta = 180°$, so that the magnetisation is along the direction of the lines, which is then called the easy-axis.

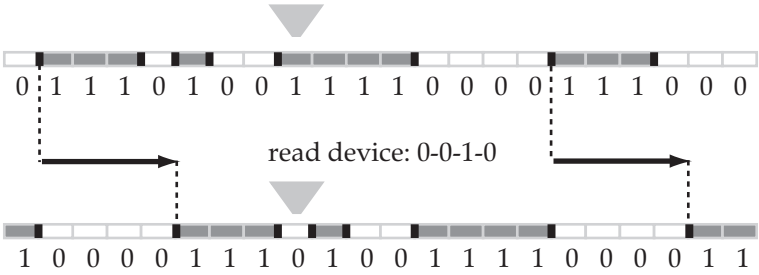

Figure 1.5: *Schematic of racetrack memory as proposed by Parkin [29]. A strip of material is divided into equally sized regions, where the magnetisation of each region stores a "0" or "1" bit. By moving all magnetic domains and domain walls through the strip, a static read device can read the data in the domains.*

The two energy minima for $H = 0$, are the cause of hysteresis of magnetisation. If a large $\vec{H}$ is applied at an angle $\Theta = 0^\circ$, $\vec{M}$ is forced along $\theta = 0^\circ$. If $\vec{H}$ is reduced to zero and then increased in the $\Theta = 180^\circ$ direction, the global energy of the system is lowest for $\theta = 180^\circ$. However, this global energy minimum can only be reached if a significantly large field is applied that removes the local energy minimum at $\theta = 0^\circ$. From Equation 1.2 we find that $\vec{M}$ only reverses sign at an applied field of size $H_C = 2K/(\mu_0 M_s)$, which is known as the coercive field. In Figure 1.4 the calculated hysteresis curves of the component of $\vec{M}$ along $\vec{H}$ are presented for $\vec{H}$ at $\Theta = 0^\circ$ and $\Theta = 90^\circ$. For $\Theta = 0^\circ$ (along the easy axis) the magnetisation switches at $H_C = 2K/(\mu_0 M_s)$. For $\vec{H}$ applied at $\Theta = 90^\circ$, which is called the hard axis, the magnetisation is along $\theta = 0^\circ$ or $\theta = 180^\circ$ when no field is applied, so that $H_C = 0$ A/m.

The magnetic switch behavior shown in Figure 1.4 based on a Stoner-Wohlfahrt model shows clear angular dependence. In Chapter 4 of this thesis, we present line structures in thin ferromagnetic layers created with a technique called shadow-lithography. These line structures introduces a strong shape anisotropy leading to the presence of an easy axis along the direction of the lines. However, in Chapter 5 we find that atom-lithographically structured Fe films do not conform to the simple easy/hard axis model of magnetisation.

Therefore we also the concepts of domain walls and domain wall movement. If two adjacent areas of a single structure have a different magnetisation, the boundary of these areas is a domain wall. Domain walls have recently attracted significant scientific attention amongst others because Parkin devised a new magnetic memory called "race track memory" [29]. In traditional magnetic data recording media, information is stored in the local magnetisation of individual areas on a sample, that we refer to as bits. These bits are read or written by mechanically positioning a read-write device on top of each bit. In the race track memory data is still stored in a series of bits on a wire or line, but now these bits can be shifted along this wire by moving all domains and domain walls while the read-write device has a fixed position as shown in Figure 1.5. In a race track memory, the domains and domain walls

are moved using spin-polarised currents, which is beyond the scope of this thesis, a description can be found in [29]. The basic concept of domain walls and domain wall movement are invoked in Chapter 5 to explain our observation of unusual magnetic properties of thin Fe films created with atom lithography.

1.4 Thesis outline

In this thesis results will be presented both regarding atom lithography as a technique as well as regarding the magnetic properties of structures created with atom lithography. In contrast with previous reports [25, 19] we find that atom lithographic structuring of Fe does influence the magnetic properties of the deposited Fe layers.

In Chapter 2 an overview of the atom lithography setup is provided, highlighting the improvements since the work of Smeets [25] and Te Sligte [26]. In Chapter 3 the structure formation in atom lithography is discussed when laser cooling is not applied to collimate the atom beams before focusing. As it is shown that laser cooling is indeed not required, the implications for atom lithography with other elements are presented and a new method to create more complex patterns is proposed.

In Chapter 4 we describe the results of reference experiments on the magnetic properties of unstructured thin layers of Fe and Fe_xNi_{1-x}. Secondly, an alternative method is presented to produce periodic magnetic Fe_xNi_{1-x} line structures based on interference lithography and shadow deposition. The magnetic properties of these structured layers are also explored in Chapter 4 as a second reference to the atom lithographic structures that are presented in Chapter 5. In Chapter 5 we show that such structuring of Fe layers influences the magnetic properties. Structuring thicker layers of Fe induces anisotropies in the magnetic properties and that cannot be explained using only shape anisotropy in a Stoner Wohlfahrt model, but seem to indicate domain wall effects. In this chapter also the first results of co-deposition of Fe_xNi_{1-x} layers structured with atom lithography are presented.

Chapter 6 presents an investigation of options to focus and compress atom beams below a 100 nm size without the use of mechanical apertures, investigating the possibilities to create a true “nanopencil” with a high writing speed. Using simulations it is shown that heating effects unfortunately prevent the creation of such small atom beams in realistic experimental settings.

Chapter 2

Experimental Setup

This chapter describes the experimental setup used to create atom lithographic structures. The basis was already described in the theses of Smeets [25] and Te Sligte [26]. This chapter is therefore brief, highlighting only the main changes to the setup. As the setup consists of generally two parts, the laser system and the deposition setup, they are discussed in separate sections.

2.1 Laser system

For atom lithography of iron a light field is required resonant with the $^5D_4 \rightarrow {}^5F_5$ transition at $\lambda = 372$ nm. To create this wavelength, a three step process is used as described by Smeets [25]. A diode-pumped solid state laser (Verdi 18 from Coherent Inc.) pumps a Titanium:Sapphire (Coherent 899-21) laser set at 744 nm, whose light is frequency doubled in a doubling cavity built at the Free University of Amsterdam. It should be noted that the diode pumped solid state laser has replaced the Ar^+ laser that was described by Smeets. A schematic of the setup is shown in Figure 2.1.

The doubling cavity is based on the design described in [31]. For the frequency doubling a 10 mm long non-linear crystal made of Lithium Triborate (LBO) is placed in the cavity. To obtain a longer lifetime of the crystal, an anti-reflection coated crystal cut at 90° angles was installed to replace an uncoated crystal cut at Brewster's angle. The coated crystal has been used for over two years, showing no sign of degradation. The new crystal does require the use of an optical isolator between the Ti:S laser and the doubling cavity to prevent back reflections into the Ti:S laser. The doubling cavity is locked using Hänsch-Couillaud locking [30].

To lock the frequency of the doubled output at 372 nm to the $^5D_4 \rightarrow {}^5F_5$ transition in iron, polarization spectroscopy [32] is used. To obtain an atomic vapor of iron suitable for spectroscopy, an Fe-Ar hollow cathode discharge is used, where atomic Fe is sputtered off the iron cathode by Ar ions from the discharge. Both the Fe-Ar hollow cathode discharge and the locking setup are discussed in detail in [33]. For the polarization spectroscopy, a circularly polarised pump and linearly polarised probe laser beam, counter-propagate through the iron vapor as shown in Figure 2.1. The circular pump beam changes the population of the magnetic substates of the iron atoms, creating a Doppler-free birefringence for the probe beam. By analysing

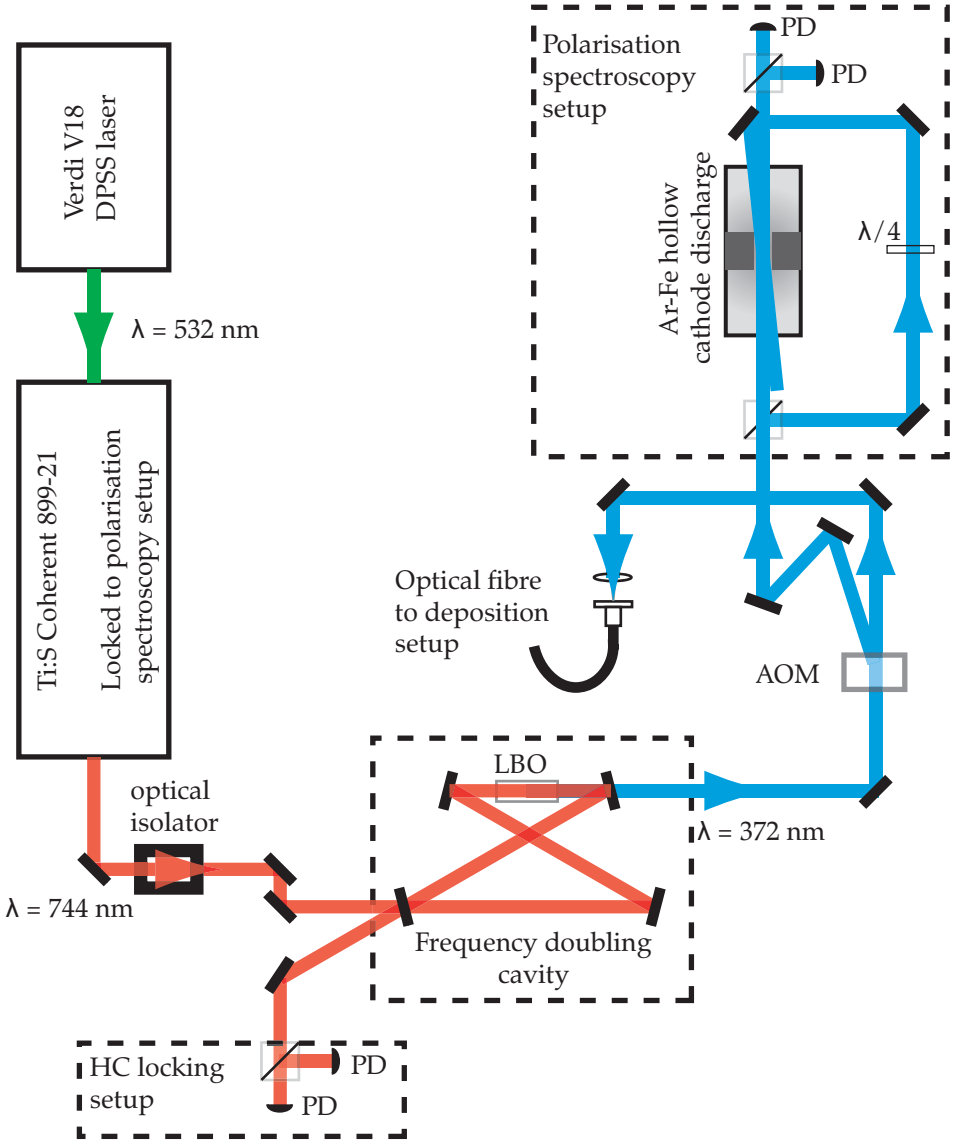

Figure 2.1: *Schematic top view of the optical setup on the optical table, showing the lasers and optics. A DPSS laser at $\lambda = 532$ nm pumps a Ti:S laser set at $\lambda = 744$ nm. This beam is frequency doubled to $\lambda = 372$ nm. The 372 nm light is sent through an acousto-optical modulator, creating a first order beam with a detuning of 150 MHz, which is sent to the polarisation spectroscopy setup. The fundamental beam is sent into an optical fiber to the deposition setup. The frequency doubling cavity is locked using Hänsch-Couillaud locking [30], the Ti:S is locked to the resonant iron transition with a detuning of 150 (2 π) MHz using the polarisation spectroscopy setup.*

the polarisation of the probe beam a dispersive signal is obtained as function of laser frequency, which can be used to lock the Ti:S laser to the transition, limiting the frequency drift to 0.2 MHz over the time scale of the deposition experiments, which is a few hours.

For the atom lithography experiments the light field is detuned by $\Delta = 150$ (2π) MHz. To this end an acousto-optical modulator (AOM) is placed in the optical path of the $\lambda = 372$ nm beam, as shown in Figure 2.1. The first order beam out of the AOM, detuned by -150 (2π) MHz, is locked to the transition at resonance, so that the fundamental beam which is used for atom lithography has an effective detuning of $+\Delta = 150$ (2π) MHz from resonance. To create a standing wave light field that has a well-defined profile and to limit effects of vibrations between the optical setup and the deposition setup, the light is transported to the deposition setup via an optical fibre. For proper in- and out-coupling the light field out of the fibre is single mode and has power levels up to 55 mW.

2.2 Deposition setup

The deposition setup was previously described in the thesis of Te Sligte [26]. This section is therefore brief on the general description and only expands on the additions to the setup. New are the option to deposit Nickel, an improved electronic control over the vacuum system as well as an improved vacuum during deposition, the use of a different type of samples and a better scheme to align and control the standing wave light field during deposition. Furthermore the deposition rates of the atom sources have been calibrated.

The deposition setup is schematically shown in Figure 2.2. It can be used to deposit thin layers of either or both Fe and Ni, from effusive sources positioned respectively perpendicularly and at 45° with respect to the sample. The sample consists of 500 μm thick Si$\langle 100 \rangle$ with a 100 nm thick oxide layer, so that the surface is SiOx, to prevent any ordered growth of Fe, which was reported on the previously used crystalline Si$\langle 100 \rangle$ with only native oxide [25]. Samples are cut to about 5 $\times$ 8 mm and ultrasonically cleaned for 15 minutes in ammonia (25% in H_2O), then in aceton and finally in isopropanol. Finally the sample is blown dry with N_2. The samples are clamped in a sample holder which also holds a mirror for the $\lambda = 372$ nm light field. The mirror is aligned ex vacuo to be perpendicular to the sample within 1 mrad. As shown in Figure 2.2, the sample holder can be placed in the vacuum so that the $\lambda = 372$ nm light can be focused onto the mirror to create a standing wave light field just above the sample, while Fe and Ni are deposited onto the sample.

The $\lambda = 372$ nm beam which is retro-reflected off the mirror in the vacuum is aligned to the incoming beam to less than 1 mrad deviation. To create a standing wave directly over the substrate, the substrate is positioned in the standing wave, such that the power in the retro-reflected beam is 50% of the maximum power reflected

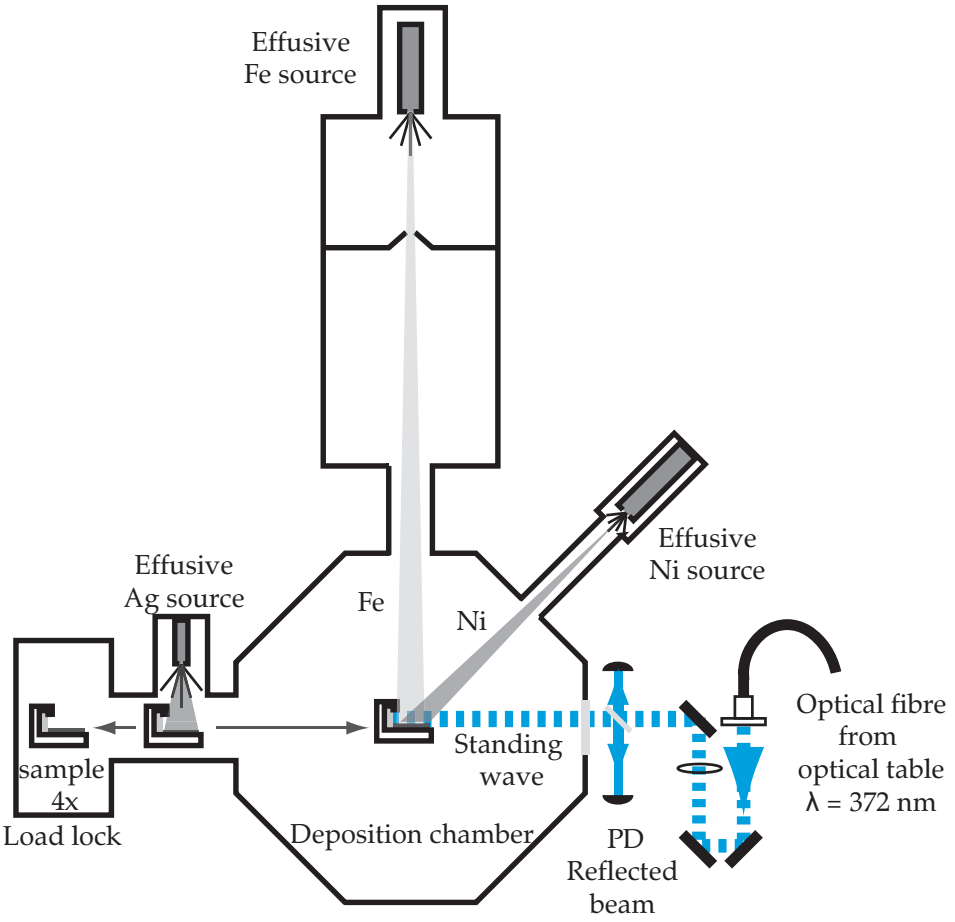

Figure 2.2: *Schematic top-view of the vacuum deposition setup. Two effusive sources of Fe and Ni deposit on the sample in the deposition chamber. The $\lambda = 372$ nm light field from the optical setup is focussed on a mirror on the sample holder in vacuum creating a standing wave just above the sample. Out of vacuum the power of incoming and reflected beam is measured using photo detectors (PD). The load lock holds up to four samples. The effusive Ag source allows for capping of the samples to protect against corrosion.*

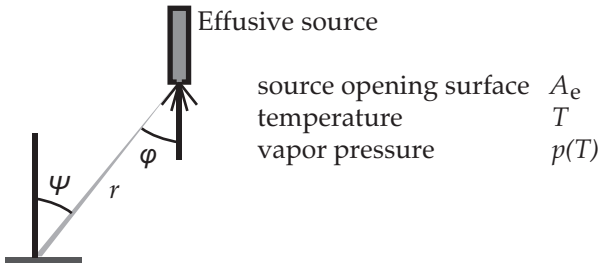

Figure 2.3: *Schematic overview of deposition from an effusive source on a sample.*

off the mirror. The retro-reflected power can be monitored during deposition. A window is placed in the light field outside the vacuum at 45° as shown in Figure 2.2, reflecting part of both the incoming and retro-reflected light field in opposite directions. The power in the retro-reflected beam deviates less than 10% during depositions of several hours.

To allow for multiple depositions without breaking the vacuum to remove samples, the setup contains a load lock which can hold up to four samples. Samples can be transported from the load lock to the deposition chamber using a linear magnetic drive. To prevent oxidation of the samples ex-vacuo, a third effusive source shown in Figure 2.2 can deposit Ag on the samples before these are removed from the vacuum. To limit oxidation and contamination of the samples in-vacuo, the vacuum system has been improved compared to the setup of Te Sligte, specifically to decrease the pressure in the deposition chamber during deposition. The improvements include on the one hand the integrated digital control of the vacuum system and the deposition sources and on the other hand an upgrade of the types of vacuum pumps and the flow restrictions used in the setup. The resulting pressure in the deposition chamber during deposition is now about $p = 5{\cdot}10^{-9}$ mbar which is an improvement of a factor 10.

To calibrate the Fe and Ni sources, all deposition rates have been measured using RBS (Rutherford Back-scattering spectrometry) with a He^+ beam in the singletron facility at Eindhoven University of Technology. RBS allows for an elemental analysis in a quantitative manner. This method is used to measure the amount of deposited material as function of deposition source setting as well as the content of materials in each sample. Measurements of both the deposition rates of the Fe and Ni sources and on the composition of Fe_xNi_{1-x} layers are presented in the remainder of this section. These measurements were performed on layers of Fe or Ni deposited on SiOx samples during two hours at different rates and capped with approximately 5 nm Ag, by depositing Ag at a rate of about 1 nm/min at a temperature of 860 °C of the Ag source.

In Figure 2.3 a schematic of deposition on a sample using an atom beam from an effusive source is given. The deposition rate R (the deposited film height per unit time) from an effusive source is given by [34]:

Table 2.1: *Values for the geometry of the effusive deposition sources for Fe, Ni and Ag. Note that values for ψ only include the part of the atom beam reaching the sample.*

	Fe	Ni	Ag
ψ	0±5 mrad	π/4±0.005 rad	0±50 mrad
φ	0±5 mrad	0±5 mrad	0±50 mrad
A_e	0.8±0.1 mm^2	0.8±0.1 mm^2	3.1±0.3 mm^2
r	0.74±0.01 m	0.38±0.01 m	0.07±0.01 m

$$R = p\sqrt{\frac{m}{2\pi k_B T}}\frac{A_e}{\rho\pi r^2}\cos(\psi)\cos(\varphi) \tag{2.1}$$

where ψ is the angle of the normal of the substrate with the atom beam, ϕ is the angle of normal of the source opening and the atom beam as indicated in Figure 2.3. The surface area of the source opening is given by A_e, r is the source-substrate distance, m is the mass of the evaporated element, ρ is the density of the element in the deposited layer, T is the source temperature and p is the partial vapor pressure, which is a known function of T for each atomic species [35].

For all three sources, values of the geometry of the source are given in Table 2.1. Values for m, ρ and $p(T)$ are known from literature [35], and for the Ni and Ag sources T is monitored during deposition. However, the home-built Fe source can only be controlled by setting the current to the heater of the source, as there is no direct measurement of its temperature. Using the Stefan-Boltzmann radiation law, the source temperature T and heating current I for ohmic heating current are related using:

$$T(I_1)/T(I_2) = (I_1/I_2)^{1/2} \tag{2.2}$$

Using this relationship and Equation 2.1, Te Sligte modelled the deposition rate of the Fe effusive source. However, Equation 2.1 requires a conversion constant from I to T that Te Sligte used to fit the model to the measurements. In Figure 2.4 the fitted values of Te Sligte are presented, together with the new results from RBS measurements. It is clear that these results do not overlap, which is a result of a replacement in the effusive Fe source of both the heating coils, the heat shielding and the crucible. Using a new conversion constant from I to T the measurements have been fitted, as shown in Figure 2.4. The average deviation of the measured data to the fit is 20%, but for currents $I \geq$33 A, used in all further depositions of Fe, the fit is accurate to within 5%.

The Ni deposition source that was added to the setup is a commercial effusive cell (HTC-40-2-180-WK-Hor, Createc Fischer & Co. GmbH), that is suitable for horizontal use, meaning that the effusive beam is in the horizontal plane. A pyrolithic

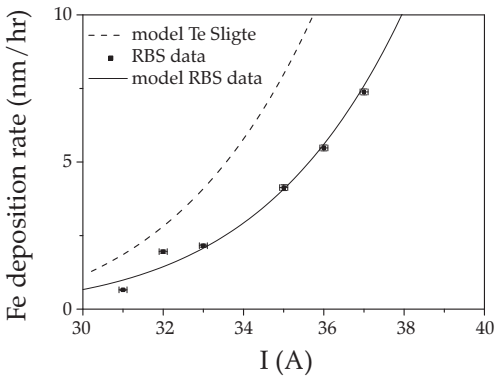

Figure 2.4: *Deposition rate of the effusive Fe source on the samples, as modelled by Te Sligte [26] (dashed line) and measured with RBS (points) and modelled based on the RBS results (solid line)*

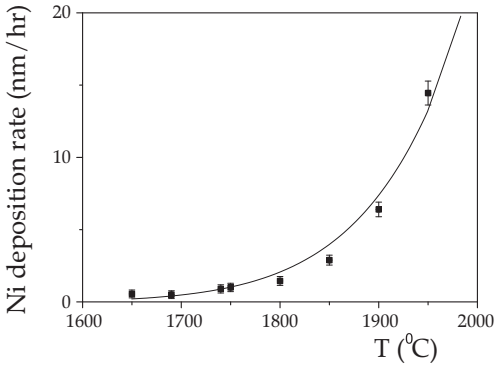

Figure 2.5: *Deposition rate of the effusive Ni source measured with RBS.*

graphite crucible is used, allowing for source temperatures up to $T = 2000$ °C. The measured deposition rate for the Ni source is shown in Figure 2.5. The measurements follow the shape of the model curve, but have significant deviations. These deviations can be as large as 40% of the deposition rate or indicate an uncertainty in temperature of up to 25°. A likely explanation for these errors is a partial clogging of the opening of the effusive cell, which is supported by the fact that the larger errors are found for higher deposition rates and that the errors are a decrease in deposition rate compared to the model. During refilling of the effusive cell any deposit obscuring the opening is therefore routinely cleaned.

In the RBS measurements the composition of the deposited films has also been investigated. Traces of carbon and oxygen have been observed in layers of more than 10 nm thick. They are less than 2 at% for carbon and less than 2.5 at% for oxygen. The origin of these traces can be either from the background gas in the deposition chamber, or from the deposition sources. The Fe source has a source

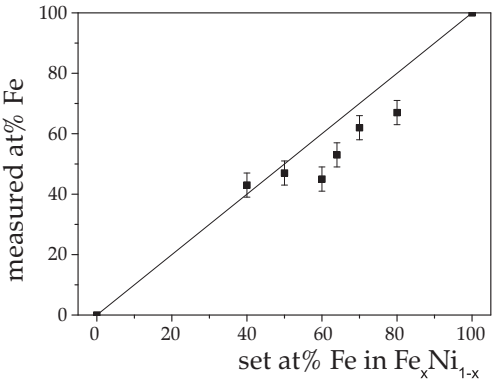

Figure 2.6: *Measured at% of Fe in Fe_xNi_{1-x} as function of composition aim based on the Fe and Ni source calibrations.*

of carbon in the carbon heating coils and a source of oxygen in the Al_2O_3 crucible. As both the heating coils and the crucible show visual signs of degradation after prolonged use, they are a likely candidate to contribute to the carbon and oxygen contaminations observed in the samples.

Based on the calibrations of the Fe and Ni source, 10 nm thick layers of Fe_xNi_{1-x} have been deposited on SiOx samples and capped with Ag varying the composition over $0.4 \leq x \leq 0.8$. The actual composition of these samples was measured using RBS; the results are shown in Figure 2.6. We find that the trend of the composition is according to expectations, but that the value for x is lower than expected for high Fe content (up to 13 percent point lower for $x_{aimed} = 0.8$). This indicates that the calibrations of our Ni and Fe sources have an error margin, which is further supported by the non-monotonous behavior in Figure 2.6 at $x_{aimed} = 0.6$, but that the composition of Fe_xNi_{1-x} layers can be tuned to within 13 percent point.

Chapter 3

Structure formation in atom lithography using geometric collimation

Atom lithography uses standing wave light fields as arrays of lenses to focus neutral atom beams into line patterns on a substrate. Laser cooled atom beams are commonly used, but an atom beam source with a small opening placed at a large distance from a substrate creates atom beams which are locally geometrically collimated on the substrate. These beams have local offset angles with respect to the substrate. We show that this affects the height, width, shape and position of the created structures. We find that simulated effects are partially obscured in experiments by substrate dependent diffusion of atoms, while scattering and interference just above the substrate limit the quality of the standing wave lens. We find that in atom lithography without laser cooling the atom beam source geometry is imaged onto the substrate by the standing wave lense. We therefore propose using structured atom beam sources to image more complex patterns on subwavelength scales in a massively parallel way.[1]

[1] * Published as: *Structure formation in atom lithography using geometric collimation.* T. Meijer, J.P. Beardmore, C.G.C.H.M. Fabrie, J.P. van Lieshout, R.P.M.J.W. Notermans, R.T. Sang, E.J.D. Vredenbregt and K.A.H. van Leeuwen, Applied Physics B: Lasers and Optics, **105** (4), 703-713, (2011), doi: 10.1007/s00340-011-4743-5

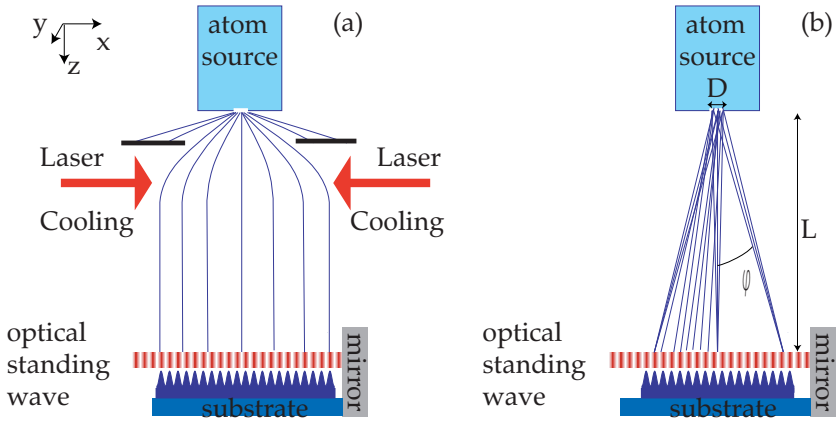

Figure 3.1: *Schematical overview of atomic nanofabrication using (a) laser cooling, creating a globally collimated atom beam, compared to (b) geometric cooling, creating a locally collimated atom beam. D is the diameter of the opening of the atom source, L is the atom source-sample distance and φ is the angle under which the atom beam locally impinges on the sample.*

3.1 Introduction

Atom lithography is a technique to structure atomic depositions, based on the use of dipole interactions of neutral atoms with near-resonant light fields. As the dipolar interaction energy is intensity dependent, a standing wave light field leads to a periodic potential. This potential can be used as an array of lenses for neutral atoms, with a periodicity of $\lambda/2$, where λ is the wavelength of the light. Pioneering experiments were performed by Timp et al. using sodium atoms [7] and by McClelland et al. using chromium [15]. In these experiments, beams of atoms were transversely laser cooled and then focused on a substrate into nanolines spaced exactly $\lambda/2$. Atom lithography experiments were also performed with other elements: Al [16], Yb [17], and Fe [18, 19]. Experiments using light fields other than a one-dimensional standing wave have been used to create structures such as rectangular grids [8], hexagonal arrays [9], quasi-periodic patterns [10] or holographically created patterns [13]. The quantum mechanical nature of the interaction of neutral atoms and resonant light allows for the creation of structures of $\lambda/4$ [11] or $\lambda/8$ periodicity [12]. Reviews of atom lithography are given in [36, 37].

In previous atom lithography experiments, atomic beams were transversely laser cooled to increase beam brightness and to minimise transverse velocity spread. The use of laser cooling can increase brightness by orders of magnitude [38], but brightness increase is much lower in many setups. Atomic species that do not have a closed atomic transition from the ground state, such as Al, Ga or In [39], are not suitable for laser cooling in atom lithographic experiments as atoms that decay to a different atomic state no longer interact with the light fields. Complex laser cooling

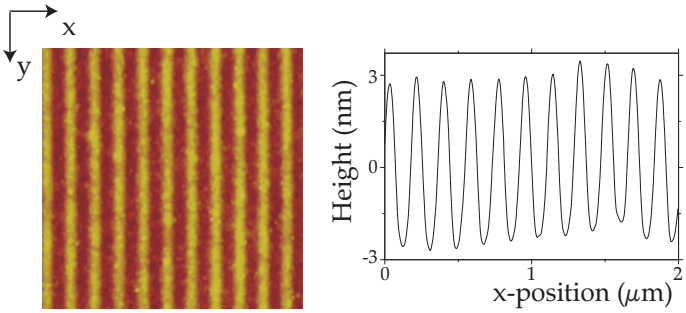

Figure 3.2: *2 × 2 μm AFM image (left) and average line cross section (right) of atom lithographic deposition of Fe without laser cooling.*

schemes can be applied, but these are experimentally challenging. The second reason for laser cooling, the minimisation of transverse velocity spread, was thought to be a key requirement for atom lithography [36], but was shown not to be essential by Smeets et al. [40].

For atom lithography the local transverse velocity spread of an atom beam impinging on a single atom lens needs to be small to enable sharp imaging. This can be achieved by geometric collimation, shown schematically in Fig. 3.1: an atom beam from a small beam source opening (e.g., 1 mm) with a large source-sample distance (e.g., 1 m), has a small local transverse velocity spread on the sample. In Fig. 3.1 we find a distinct difference between laser cooling and geometric collimation. A laser cooled beam aligns uniformly to the array of focussing lenses in the optical standing wave. However, with geometric collimation the atom beam aligns perfectly orthogonal to the focussing field at one point, but not over the entire standing wave.

In a setup without laser cooling, the transverse velocity distribution of the atom beam near the substrate is determined by the longitudinal velocity of the atom beam, the size of the atom beam source, the source-sample distance and the position on the substrate. The longitudinal velocity distribution is that of an effusive beam, with average longitudinal velocity $\langle v_{long} \rangle$. At a point on the substrate the angular distribution of an atom beam emerging from a circular hole with diameter D at a distance L from the substrate, as shown in Fig. 3.1, is in good approximation characterised by a Gaussian angular distribution with a root-mean-square width of $D/(4L)$. The transverse velocity distribution thus has an RMS spread of $\sigma v_{trans} = D/(4L) \langle v_{long} \rangle$. The local average transverse velocity, $\langle v_{trans} \rangle$, is a function of position on the substrate. At each position where the beam impinges under an angle, φ, as seen in Fig. 3.1, $\langle v_{trans} \rangle = \varphi \langle v_{long} \rangle$, as φ is small in the experimental setup.

Experimentally we have found atom lithographic structure formation of Fe over areas of up to 400 μm $\times$ 6 mm on a single substrate. An example of an atomic force microscopy (AFM) scan is shown in Fig. 3.2, where a 2 $\times$ 2 μm^2 area is shown with 186 nm periodic line structures of 6 nm height. In our setup L =0.74 m, D = 1 mm,

$\langle v_{long} \rangle = 1.0 \times 10^{3}$ m/s and $\sigma v_{trans} = 0.35$ m/s. As the total size of the structured area in x direction (perpendicular to the lines) is up to 6 mm long, φ varies over an 8 mrad range, so that $\langle v_{trans} \rangle$ varies over an 8 m/s range, more than an order of magnitude larger than σv_{trans}.

In this article we investigate the effects of $\langle v_{trans} \rangle$. We show experimental results of structure height, width and shape. We will also elaborate on two issues that influence structure formation on the surface: diffusion of atoms on the substrate after deposition and the effects of scattering and interference of the standing wave field grazing over a substrate. When we take these diffusion and interference effects into account, we can understand structure formation in a geometrically collimated atom beam using a semiclassical Monte Carlo model.

Our paper is organised as follows: we first discuss a Monte Carlo model for atom lithographic focussing and present simulations using this model with transverse velocities included. Then we present the experimental setup, show the experimental results of structure formation and compare them with simulations. We show how the effect of the light field configuration influences experimental results. Furthermore, we show what the impact on the results is of diffusion of atomic depositions on the substrate. Finally, we discuss further possibilities and improvements of atom lithography without laser cooling and propose a novel scheme for a sub-wavelength patterning technique, based on geometrically collimated atom beams.

3.2 Simulations

The potential of an atom in a near-resonant light field follows from the so-called dressed state model. The energies of dressed states $|1\rangle$ and $|2\rangle$ in a light field with a detuning Δ from resonance, are [41]:

$$E_{1,2} = -\frac{\hbar\Delta}{2} \pm \frac{\hbar}{2}\sqrt{\Delta^2 + \Gamma^2 \frac{I(\mathbf{r})}{2I_s}^2}. \tag{3.1}$$

Here $I(\mathbf{r})$ is the local intensity, I_s is the saturation intensity and Γ is the natural line width.

The light field intensity in our simulation is modelled as a Gaussian standing wave (SW):

$$I(\mathbf{r}) = \frac{8P}{\pi w^2} \sin^2(kx) \cdot \exp(-2\frac{z^2}{w^2}) \cdot \exp(-2\frac{y^2}{w^2}). \tag{3.2}$$

Here $k = 2\pi/\lambda$, w is the waist of the laser beam, P is the laser power, and x, y, z are positions as shown in Fig. 3.1. In our experiments we use focused Gaussian laser beams, but we disregard wavefront curvature because experiments are performed well within a Rayleigh length of the focus position.

Table 3.1: *Characteristics for iron and the transition used.*

Transition		$^5D_4 \rightarrow {}^5F_5$
Wavelength	λ (nm)	372.0
Linewidth	$\Gamma/2\pi$ (MHz)	2.58
Saturation intensity	I_s (W/m^2)	62
Doppler velocity	v_d (m/s)	0.1

In the experiment we use light fields with large positive detuning $\Delta \geq 50\Gamma$, so that ground state atoms entering the light field will initially be in the $|1\rangle$ dressed state adiabatically connected to the atomic ground state. This state has the lowest energy for the minimum intensity of the light and therefore atoms are focused towards a local intensity minimum.

We use Fe atoms and a $\lambda = 372$ nm light field that is near resonant with the $^5D_4 \rightarrow {}^5F_5$ transition in Fe. This transition is not fully closed, but as we use light relatively far detuned from resonance, optical pumping to other atomic states is ignored. Characteristics of the transition are given in Table 3.1.

To simulate the focussing process, we use a Monte-Carlo trajectory calculation. Each simulation uses 10^5 atoms which are considered as classical point particles moving in the dressed-state potentials. Initially all atoms are in the $|1\rangle$ dressed state at $z = -2w$. The trajectories are calculated by numerically integrating the Newtonian equation of motion in three dimensions until the atoms reach $z = w/2$. The atomic velocity distribution mimicks that of our experimental setup in both longitudinal and transverse directions.

Spontaneous emission effects are included in our model, although these effects are not large for the large detunings and moderate intensity levels in our experiments. Direct heating by the random photon recoils from the spontaneous emissions ('spontaneous diffusion') is included, as well as 'stimulated diffusion' due to dressed state changing spontaneous emissions. After each spontaneous emission, a random photon recoil momentum is added to the atom's momentum and the possibility that the atom switches to the other dressed state is taken into account.

To include the effects of magnetic substates, the atoms are uniformly distributed over the magnetic substates and the appropriate Clebsch-Gordan coefficients are assigned to each atom, assuming a linearly polarized lightfield. The local intensity is multiplied by the Clebsch-Gordan coefficient, resulting in different potentials and thus different focal lengths for each magnetic substate. The possibility that the magnetic substate of an atom changes during spontaneous emission is neglected.

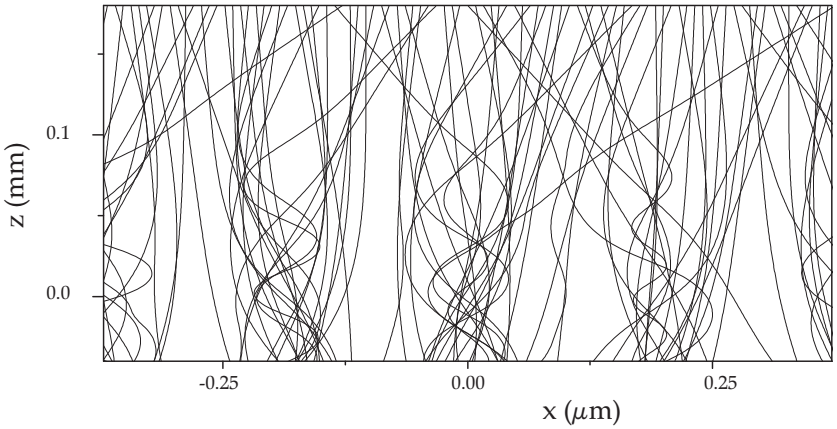

Figure 3.3: *Overview of atomic trajectories in a SW light field of $P = 20$ mW, $w = 90$ μm and $\Delta = 150$ (2π) MHz.*

3.3 Simulation results

In Fig. 3.3 we show some typical atomic trajectories of atoms moving from top to bottom through the SW potential of a light field with Δ 150 (2π)MHz, $P = 20$ mW and $w = 90$ μm. Atoms are focused towards the intensity minima at $x = 0$ nm and $x = \pm$ 0.186 μm, but the trajectories do not share a single focal point. This is partly due to the effect of the different potentials for the magnetic substates and the large chromatic abberation, as the RMS spread of v_{long} is 357 m/s.

In our experiments the substrate is positioned at the point of maximum laser intensity, $z = 0$ μm, therefore we take the simulated atomic distribution in that plane. On the left of Fig. 3.4 we show atomic distributions at $z = 0$ μm and around $x = 0$ μm (thus $\varphi = 0$ mrad) for a light field of $w = 90$ μm at several y-positions. We observe that for nonzero y-positions, where local light intensity is lower, atoms are focused less tightly resulting in lower and broader distributions. To characterize the simulation results, we fit the atomic distribution with a Gaussian, an example is shown on the right-hand panel of in Fig. 3.4. The values we find in the Gaussian fit for peak height over the pedestal, h, and the full width at half maximum, w_h, can be compared to experimental results. To convert simulated atomic distributions into height values, we take into account the Fe flux in our experiment and the fraction of atoms that are in the atomic ground state and therefore interact with the potential.

In the left-hand panel of Fig. 3.5 we show simulation results for focussing by the same light field at $y = 0$ μm, but with atom beams with different values for $\langle v_{trans} \rangle$ (thus different offset angle φ). For non-zero $\langle v_{trans} \rangle$ the maximum in the atomic density distribution shifts relative to the potential minima at $x\,(modulo\,\lambda/2) = 0$ nm by some value Δx, shown on the right of Fig. 3.5. The height of the simulated structures decreases and we find that they are no longer symmetric. To obtain a

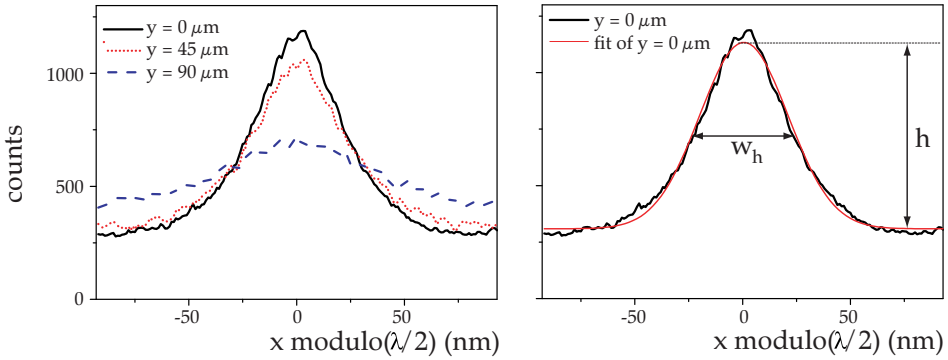

Figure 3.4: *Simulated atomic distribution of atoms around $x = 0$ μm (thus $\varphi \simeq 0$ mrad) in the plane $z = 0$ μm for atoms focused by a SW light field with $w_0 = 90$ μm, $P = 20$ mW. Left: at positions in the light field $y = 0$ μm (thick black curve), $y = 45$ μm (dotted red), $y = 90$ μm (dashed blue). Right:Gaussian fit of $y = 0$ μm (thin red), indicating peak height h and full width at half maximum w_h.*

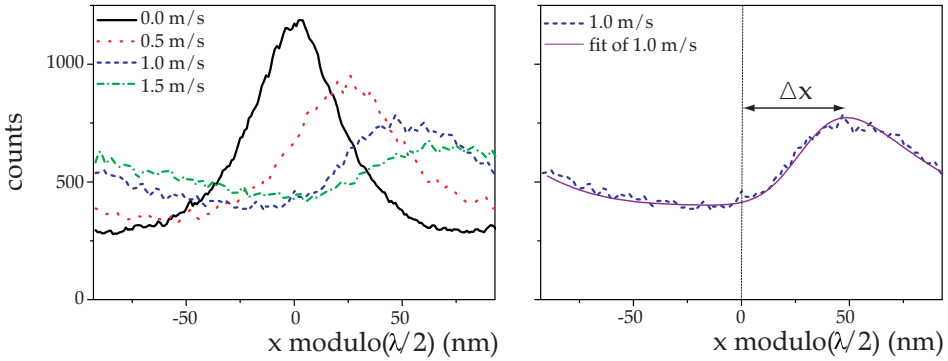

Figure 3.5: *Left: Simulated atomic distribution in the plane $z = 0$ μm and $y = 0$ μm for atoms beams with $\langle v_{trans} \rangle$ of 0 m/s (solid black curve), 0.5 m/s (dotted red), 1.0 m/s (dashed blue) and 1.5 m/s (dashed-dotted green), focused by a SW light field with $w_0 = 90$ μm and $P = 20$ mW. Note that $\langle v_{trans} \rangle = 1$ m/s is equal to $\varphi = 1$ mrad. Right: Simulated atomic distribution of $\langle v_{trans} \rangle = 1$ m/s, fitted with a skewed Gaussian and indicating peak shift Δx.*

numerical value for the asymmetry of the simulated structures, we use the skewed Gaussian distribution, described by:

$$f(x) = \frac{1}{\sqrt{2\pi}} \exp\left(\left(\frac{x - x_0}{\sqrt{2}w}\right)^2\right)\left(1 + \operatorname{erf}\left(\alpha \frac{x - x_0}{\sqrt{2}w}\right)\right). \tag{3.3}$$

The skewness parameter α is a measure for the assymmetry of the distribution. On

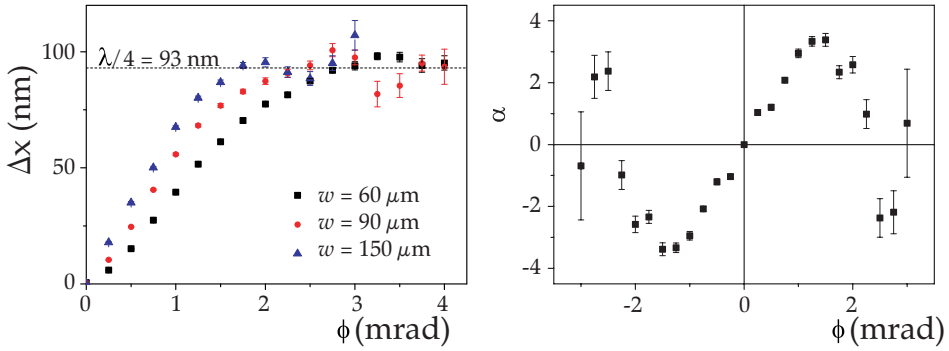

Figure 3.6: *Effects of nonzero φ on simulated atomic distributions showing on the left Δx vs φ for light fields of $w = 150$ μm and $P = 55$ mW (blue triangle); $w = 90$ μm and $P = 20$ mW (red dots); $w = 60$ μm and $P = 50$ mW (black squares); indicating $\Delta x = \lambda/4 = 93$ nm (dashed line) and on the right skewness parameter α vs φ of the deposited structures for $w = 90$ μm and $P = 20$ mW.*

the right of Fig. 3.5 we show the fit of the atomic distribution for the $\langle v_{trans} \rangle$ =1 m/s simulation with a skewed Gaussian distribution.

In Fig. 3.6 on the left we show Δx as a function of φ for simulations with different light field configurations. All three curves give a linear behaviour for small φ, until Δx levels off at $\Delta x = \lambda/4 = 93$ nm. Although we found in Fig. 3.3 that there is no single focal length of our focussing potential, the linear regime of Fig. 3.6 can be modelled with the formula $\Delta x = f \cdot \sin \varphi$, with f an effective focal length of the lens, resulting in e.g., $f = 66$ μm for $w = 150$ μm and $P = 55$ mW. It should be noted that the shift of the peak positions will be nearly impossible to observe experimentally, as the change in distance between two neighboring structures will be on the order of 10^{-11} m.

For larger φ, Δx moves towards $\lambda/4 = 93$ nm, the position where the SW potential is maximal. If atoms move beyond $\Delta x = \lambda/4$, they move through the SW potential maximum towards a neighboring potential minimum. In that case an atom is no longer focused by a single lens, but is moving through a periodic potential. Atoms are then more likely to be near the maxima of the potential where their kinetic energy and thus speed is lower. At higher values of φ, the peak position therefore remains near the maximum of the potential, thus at $\Delta x = \lambda/4 = 93$ nm.

A second effect of non zero $\langle v_{trans} \rangle$ was observed in the skewness of the lines. In the right-hand panel of Fig. 3.6 we show the skewness parameter α of line structures modelled for a SW potential of $w = 90$ μm and $P = 20$ mW; other standing waves give similar results. We find that for small φ, α increases linearly with φ up to $\varphi =$ 1.5 mrad. At this angle where we showed on the left of Fig. 3.6 that Δx changes from a linear regime to the $\Delta x = \lambda/4$ level, the skewness also changes behaviour. For larger values of φ, the skewness is ill determined and fluctuating around $\alpha = 0$.

Table 3.2: Characteristics of the atom beam

atom source diameter	D (mm)	1
atom source - sample distance	L (m)	0.74
atom source temperature	T (K)	2000
average longitudinal velocity	$\langle v_{long} \rangle$ (m/s)	$1.0 \cdot 10^3$
longitudinal velocity spread (RMS)	σv_{long} (m/s)	357
transverse velocity spread (RMS)	σv_{trans} (m/s)	0.35

3.4 Experimental setup

A schematic of our setup is shown on the right-hand side of Fig. 3.1. To be able to deposit Fe at a reasonable flux, we require temperatures up to 2000 K for which we use a home-built effusive Knudsen cell [42]. This Knudsen cell has a circular opening of 1 mm diameter and is located 740 mm from the sample. The characteristics of the atom beam and the beam geometry are given in Table 3.2. The thermal population of Fe atoms at 2000 K gives an occupation of the ground state of 47%, which is the only state that has an interaction with the light field. Substrates are exposed to the atom beam for two hours, resulting in deposited Fe films of an average thickness of approximately 15 nm.

The 372 nm light needed to excite the $^5D_4 \rightarrow {}^5F_5$ transition of Fe produced by a titanium-sapphire laser, frequency doubled with an LBO crystal in a ring cavity and frequency locked using the method described in [33]. An acousto-optical modulator is used to introduce a detuning $\Delta = 150$ (2π) MHz. The 372 nm light is passed through a single mode fiber and is then focused onto a mirror in the vacuum to create a standing wave with waist sizes between 60 and 150 μm. The retroreflected beam is aligned to the incoming beam to less than 1 mrad deviation. The substrate is positioned in the standing wave as shown top right in Fig. 3.7, such that the power in the retroreflected beam is 50% of the maximum power reflected off the mirror.

In Fig. 3.7 we show the sample holder, on which the samples are clamped and a mirror is mounted.Substrates are SiOx, which is amorphous to prevent ordered growth effects due to crystalline substrates. The mirror can be aligned perpendicular to the substrate within 1 mrad ex vacuo. The sample holder is placed in the deposition chamber, which has a typical pressure below 10^{-8} mbar. In the deposition chamber, the atom beam has a diameter of 7 mm and it impinges normal to the substrate near the centre of the substrate. In the bottom right of Fig. 3.7 we show that line structures can be created where the laser field overlaps the area of Fe deposition.

The resulting structures have been imaged using atomic force microscopy (AFM). We measured under ambient conditions on a Digital Instruments Dimension 3100 AFM in tapping mode, using Si cantilevers with a radius of curvature less than 10 nm. As our structures have typical ratios of h/w_h below 10^{-1} we disregard tip artefacts.

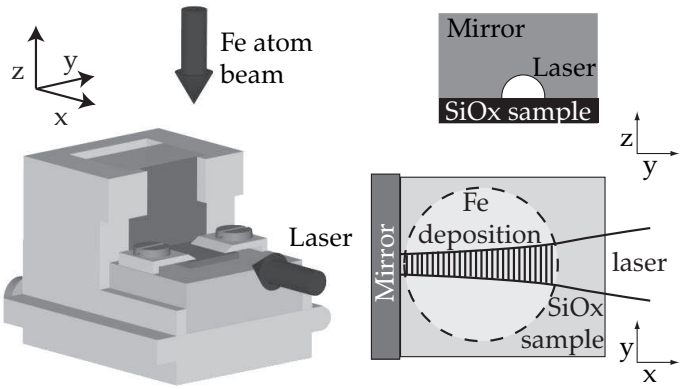

Figure 3.7: *Left: Sample holder. Top right: View along laser field showing 50% cut-off. Bottom right: View along Fe atom beam showing overlap of laser and deposition area on sample where line structures are created.*

Measuring along the y direction gives information of the influence of the local laser intensity, where we take $y = 0$ at the position of maximum laser intensity. Measuring along the x direction gives insight in the effects of the transverse velocity of the Fe atom beam, where $x = 0$ corresponds to $\langle v_{trans} \rangle = 0$. AFM measurements are performed on areas of 250 nm along the lines and 2 μm perpendicular to the lines, so that 11 lines are visible. The image is averaged over the y-direction and in the resulting cross section of the line structures each line is fitted with a Gaussian giving average and spread values of h and w_h.

3.5 Experimental results

In Fig. 3.8 we present experimental and simulation results for h and w_h of deposited lines as a function of y-position, while $x = 0$ (thus $\langle v_{trans} \rangle = 0$). Three settings of P and w are shown. In Fig. 3.9 we present experimental and simulation results of lines deposited at $y = 0$ mm, thus at the maximum intensity level of the laser field as a function of x-position, which is proportional to $\langle v_{trans} \rangle$. In our simulations the highest lines are found for the highest laser power and for an atom beam with $\langle v_{trans} \rangle = 0$. This behaviour is confirmed in our experiments.

In Fig. 3.8 we find that structure formation is influenced by the local intensity of the laser field. The simulation results show bell-shaped dependence of h on y-position, which is wider and more flat topped than the intensity profile. This indicates that the focussing is less sensitive to intensity changes at high intensity. This is confirmed by the simulation values of w_h, which are reasonably constant for $|y| \lesssim w$, while for larger y, corresponding to lower intensities, w_h increases. The experimental results for h match the simulations for the outside positions, but differ greatly for $|y| \lesssim w$.

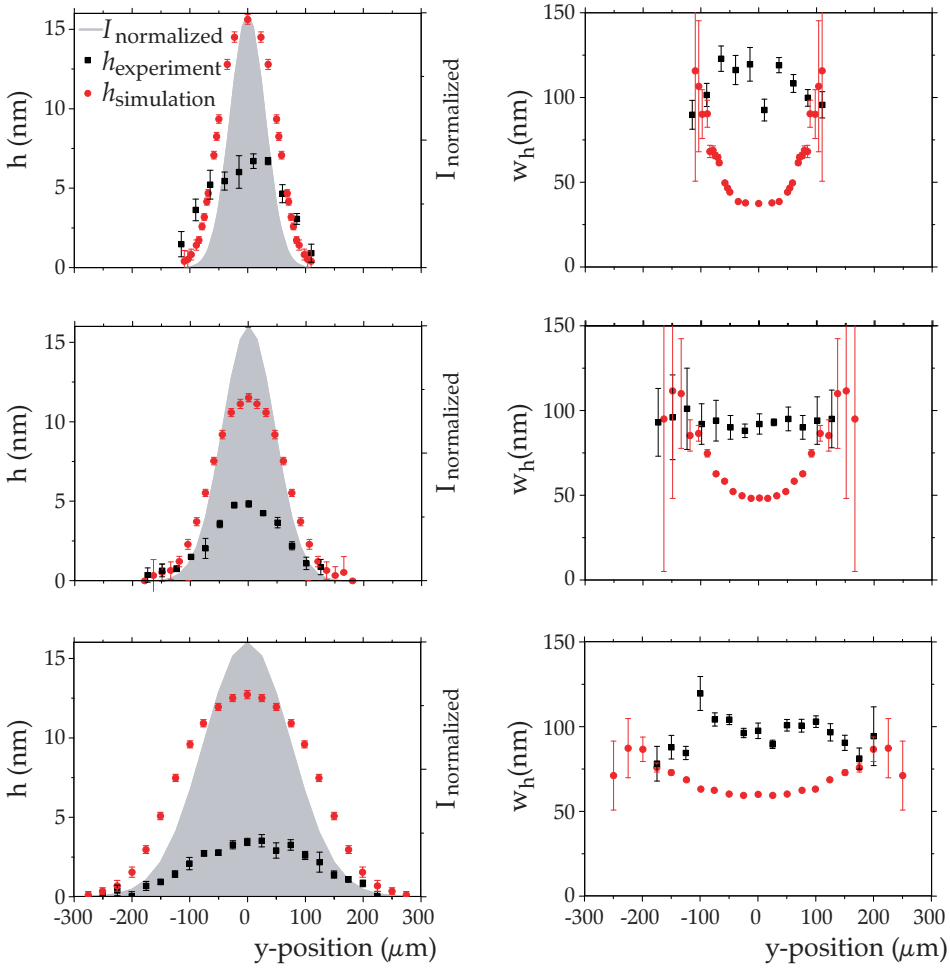

Figure 3.8: *h (left) and w_h (right) of simulated (red dots) and experimentally measured lines (black squares) for different y positions and different laserfield settings, from top to bottom $w = 60$ µm and $P = 50$ mW; $w = 90$ µm and $P = 20$ mW; $w = 150$ µm and $P = 55$ mW. A laser intensity profile normalized to the maximum intensity of the measurement is shown in the left-hand images (grey area).*

At y =0, h is two to three times smaller than expected. Experimental values of w_h hardly depend on y-position. Values of w_h are between 80 and 120 nm, which corresponds to simulation values at the extreme y-positions, but simulation values of w_h around y =0 are significantly smaller, down to 35 nm.

The influence of local $\langle v_{trans} \rangle$ on structure formation is shown in Fig. 3.9. Experimentally we observe structures even for large values of x >4 mm, corresponding to $\langle v_{trans} \rangle$ =6 m/s. This is more than an order of magnitude larger than σv_{trans} and nearly two orders of magnitude larger than the transverse velocity associated with Doppler cooled beams where $\sigma v_{trans} = v_d$ =0.1 m/s (Table 3.2). At those values for $\langle v_{trans} \rangle$, atoms in the atom beam can pass through a maximum in the focussing potential and are therefore no longer restricted to interact with a single lens.

The simulation results in Fig. 3.9 indicate that the highest and narrowest lines are deposited for x = 0 mm, where $\langle v_{trans} \rangle$ =0 m/s. These results show a sharp decrease in line height for non-zero $\langle v_{trans} \rangle$. Experimental results indeed have a maximum for h at x = 0 mm, but this peak is less pronounced than in the simulation. The measured widths, w_h, are all between 80 and 120 nm, well over the simulated values around x = 0 mm but comparable at the extreme values of x. Both Figs. 3.8 and 3.9 indicate that the simulations predict broad, low structures correctly, but fail in the case of optimal focussing, with narrow and high lines. This points towards the presense of an additional broadening mechanism not accounted for in the simulations.

This notion is confirmed by a comparison of the simulated and experimental values for the product of h and w_h, indicating the total amount of focused material. In Fig. 3.10 we show the product for one field setting, results are similar for other settings. We find that the simulated product of h and w_h of the focused lines, compares much better to the experimental results, with errors of only about 20%.

In atom lithography, broadening of structures has been found previously [43, 44]. Two explanations have been proposed: the distortion of the lightfield by the presence of the substrate and the mobility of deposited atoms on the surface.

The effect of the substrate on the light field has been modelled by Anderson et al. [43]. Following their approach we calculated the lightfield near the centre of our substrate assuming a fully reflecting surface and mirror, from an incoming Gaussian laser field cut off at maximum intensity by the substrate. We find a dark zone just above the surface of about 10 μm high, while intensity is nearly two times higher than expected at about 20 μm from the surface. Further away from the surface the intensity patterns is more similar to the incoming Gaussian pattern. The assumption that the substrate and the mirror are fully reflective is an extreme; our experiment is much more difficult to model as Fe coats our SiOx substrate during the experiment, so that reflection coefficients and associated phase terms change during the experiment.

The dark area just above the surface can allow for defocussing of the atom beam. In our simulations we find that σv_{trans} in the plane z =0 is 0.53 m/s for the strongest

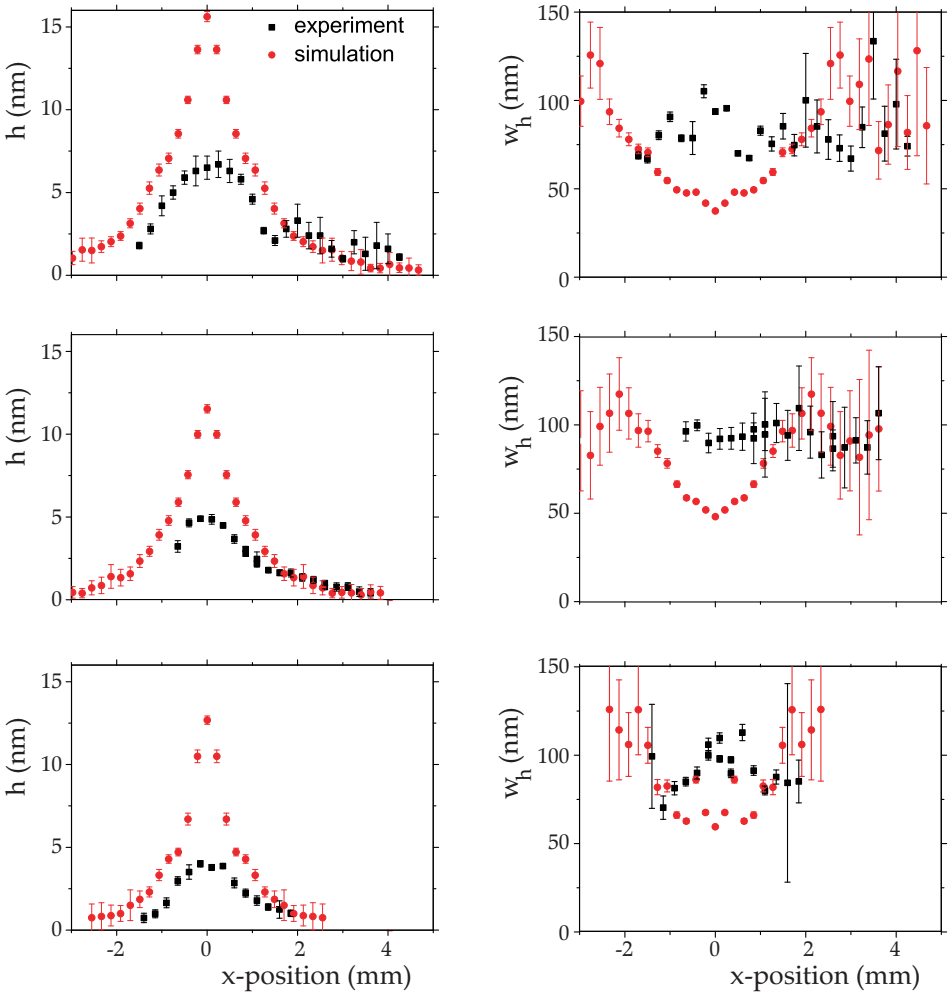

Figure 3.9: *h (left) and w_h (right) of simulated (red dots) and experimentally measured lines (black squares) for different x positions (thus different $\langle v_{trans} \rangle$) and different laserfield settings, from top to bottom $w = 60$ µm and $P = 50$ mW; $w = 90$ µm and $P = 20$ mW; $w = 150$ µm and $P = 55$ mW.*

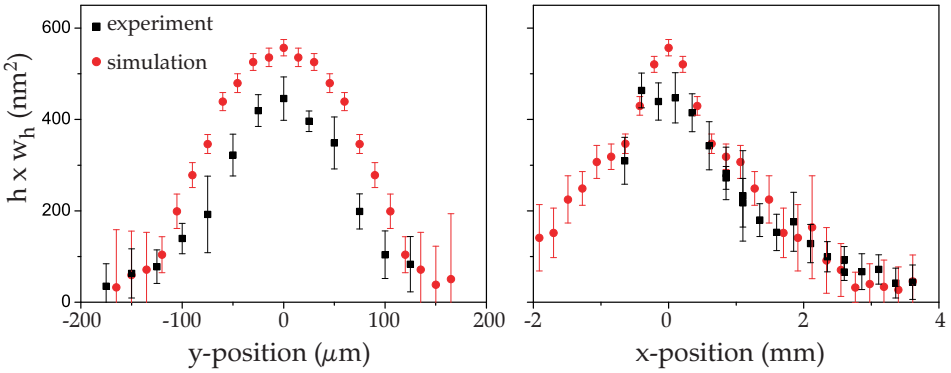

Figure 3.10: *Measured (black squares) and simulated (red circles) product of h and w_h for light field of $w = 90$ μm, $P = 20$ mW as a function of y-position (left) and x-position (right).*

focused beams, leading to a maximal broadening of 6 nm on both edges of the focused line structure in a 10 μm high dark area. As the intensity is higher just above the dark zone over the substrate, the focussing strength might be greater at some points, thus also leading to stronger defocussing. However, it seems that the divergence in the dark zone over the substrate alone cannot account for the broadening of the structures from 35 nm to over 80 nm that we observe in Figs. 3.8 and 3.9.

The mobility of atoms on a surface and the resulting blurring of structures has also been a subject of study in the field of atom lithography. Ballistic deposition models [45], terrace and step-edge diffusion [46] and polluted adatom limited diffusion [44] have been proposed. The latter was consistent with the experimental data of [43], but there is no complete understanding of atom mobility on the substrate. We have observed very clear effects in our setup while depositing structures on SiOx and Si$\langle 111 \rangle$. Previously reported Fe structures on Si$\langle 111 \rangle$ with native oxide created with a very similar setup had a typical w_h of 50 nm [40], while our current line structures deposited on SiOx have a typical w_h of over 80 nm.

As a reference experiment to the atom lithographic experiments on Si$\langle 111 \rangle$ and SiOx, we have deposited Fe through physical masks with line patterns, to deposit well defined structures onto Si$\langle 111 \rangle$ or SiOx substrates. The masks are made of 100 nm thick silicon nitride which are e-beam patterned with line patterns of 80$\pm$5 nm wide and several 100 μm long. The masks are clamped directly on the substrate, so that the mask-substrate distance is less than 10 μm. We have deposited 15 to 20 nm thick layers of Fe through these line masks and measured their geometry with AFM. In Fig. 3.11 we show cross-sections of Fe nanolines deposited on SiOx and Si$\langle 111 \rangle$. We find that there is a significant influence of the substrate. This is known in literature for other materials, e.g., Tun et al. [47] observe very different structure formation of gold deposited on various substrates through physical masks.

In Fig. 3.11 we have included the expectated deposition profile based on the geome-

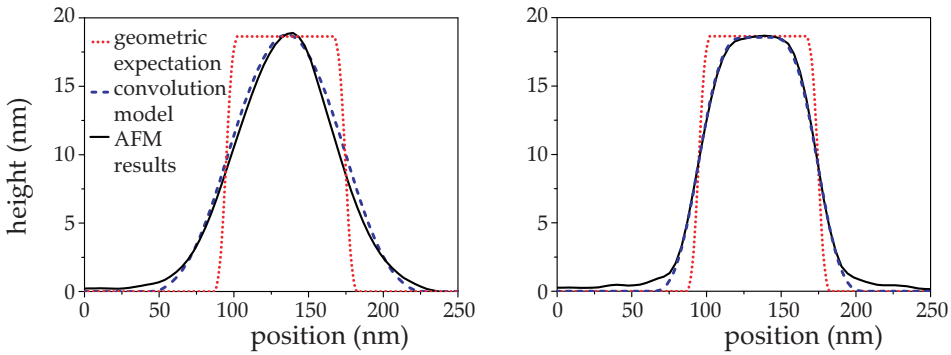

Figure 3.11: *Cross-sections of nanolines created by depositing Fe through physical masks on SiOx (left) and Si⟨111⟩ (right). Dotted red curve: geometric expected structures from the 80 nm wide mask openings. Solid black curve: measured AFM results. Dashed blue curve: a model convoluting the geometric expectation with a Gaussian of σ =23 nm (left) and σ = 12 nm (right).*

try of the mask, the divergence of the atom beam and the mask-substrate distance and find that this does not match the experimental results. We model the substrate influence as a convolution of the expectated profile with a Gaussian function, of which the standard deviation σ gives a measure for diffusion. In Fig. 3.11 we show that this gives a good match to measured profiles for σ =12 nm for Si⟨111⟩and σ =23 nm for SiOx.

The value of σ is not easily translated into an increase in width of structures in atom lithography. It should be noted that the full-width at half height in Fig. 3.11 of the expected deposition profile, the model and both measurements are nearly equal. As atom lithography creates Fe nanostructures on a Fe background, surface diffusion and broadening effects will be different from the freestanding structures shown in Fig. 3.11. However, the results indicate that diffusion effects of Fe on SiOx and Si⟨111⟩ have a range of tens of nm and we find that the value σ for SiOx is approximately twice the value for Si⟨111⟩. This matches well with the length scale over which the values of w_h of atom lithographic lines differs in simulations ($w_h \geq$35 nm) and experimental results on Si⟨111⟩ ($w_h \gtrsim$50 nm) [40] and SiOx ($w_h \gtrsim$80 nm).

Although it is likely that diffusion and broadening affects narrow and high structures more than broad structures, these results do not indicate how diffusion and broadening affects structure height and width for different deposited flux distributions. However, we have shown that substrate dependent surface diffusion effects can contribute significantly to the observed differences in w_h of our Monte Carlo model and the atom lithographic experiments.

The experiments show most of the effects found in the simulations qualitatively, although lines are broadened. We have therefore also investigated the skewness of our deposited structures, which we found in our simulations to be dependent on

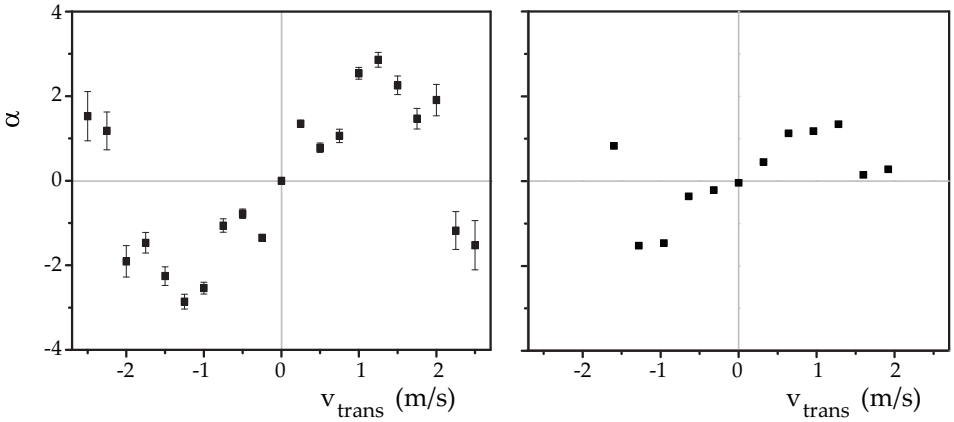

Figure 3.12: *Overview of simulated (left) and measured (right) values of skewness α of nanostructures deposited with a light field of w =150 μm and P =55 mW.*

$\langle v_{trans} \rangle$. We show the skewness parameter both for simulated and experimental results in Fig. 3.12 for structures deposited with a lightfield of w =150 μm and P =55 mW. We clearly retrieve the linear trend for values of $\langle v_{trans} \rangle$ from -1.25 to 1.25 m/s and for larger values of $\langle v_{trans} \rangle$ both simulation and experimental values break with the linear trend. Quantitatively the measured values of α are smaller than the simulation results, which is to be expected as the observed broadening of the structures in experiments will decrease skewness.

3.6 Discussion and conclusions

In this article we have shown that atom lithography is possible with atom beams that have a local $\langle v_{trans} \rangle$ of up to a few m/s. This local $\langle v_{trans} \rangle$, which corresponds to an offset angle of the atom beam with respect to the SW, influences height, width and shape of the deposited structures. These effects have been simulated and have been qualitatively observed in our samples. However, the observed structures are broader and lower than in the simulations. We find that this discrepancy can be partly explained by light scattering and interference of the light field at the reflective substrate. However, we find that our results are mostly influenced by a substrate dependent diffusion mechanism. Whereas the simulation resulted in structure sizes of $w_h \geq$35 nm, we do not find structures of $w_h <$80 nm on SiOx substrates. In our previous experiments on Si$\langle$111$\rangle$ substrates we found smaller structures of $w_h \geq$50 nm [40]. A better understanding of surface effects and choice of substrate could therefore allow for better defined structures.

As our current structuring technique does not needlaser cooling, we are no longer limited to atomic species that have closed optical transitions. This allows for the use

of technologically interesting elements such as Ga, In and Si [39] where laser cooling was shown to be experimentally challenging. We calculated the achievable flux densities without laser cooling for some elements of group III and IV (Al, Ga, In, Si, Ge, Sn) in our current setup and atom beam source geometry using data from [48]. In all cases the deposition rate is at least 10 nm per hour at beam source temperatures lower than 2000 K, which we use for Fe. As in our Fe experiment, the thermal occupation of any single (hyperfine) level of these atomic beams is significantly less than 1. Therefore, e.g., optical pumping might be required to achieve good contrast in the atom lithographic focussing.

Atom lithography without laser cooling could furthermore be improved by improving the geometry of the setup and the atom beam source. We currently employ a Knudsen cell with a round opening as an atom beam source, the size of which determines the local σv_{trans} on the sample. However, for line structures, only σv_{trans} perpendicular to the lines needs to be controlled and we can thus use slit-like source openings, with a larger surface area, but a narrower size perpendicular to the lines. This allows us to increase flux with lower σv_{trans}. The source-substrate distance L also influences σv_{trans}. As σv_{trans} is inversely proportional to L, increasing L can create locally better collimated beams. However, the flux is inversely proportional with L^2, which restricts large increases of L. A second advantage of a larger L is that the offset angles φ will be smaller, so that the deposited structures are uniform over larger areas. Adjustment of the geometry of the setup and atom beam source can thus allow for faster deposition rates, lower σv_{trans} and/or a smaller influence of $\langle v_{trans} \rangle$.

Finally we propose to use atom lithography without laser cooling to image patterns in the atomic beam onto a substrate, similar to the imaging of patterns with light in classic lithography. We show the concept in Fig. 3.13. At the left an atom beam emerges out of a single D =1 mm round opening, at distance L =0.74 m, is focused by a SW lens of w =150 μm and P =55 mW as in our current setup. The magnification ratio is f/L =8.9·10^{-5}, with f =66 μm the effective focus length we obtained from Fig. 3.6. We find that this is similar to the reduction in size of the beam source opening w_h/D =6.1·10^{-5}. The SW lens thus creates an image of the beam source onto the substrate. With laser cooled atom beams, this is impossible as laser cooling removes information of the beam source. We also simulated the focused atomic distribution of an atom beam from a beam source in front of which we place two 0.33 mm wide slits spaced 0.75 mm apart, as shown on the right of Fig. 3.13. The double slit is focused to a double line pattern spaced 60 nm apart, reducing the size of the spacing by a factor 8·10^{-5} gain very similar to f/L. Using atom lithography without laser cooling to image structured beam sources allows for the creation of patterns which are repetitive over $\lambda/2$ in a massively parallel way.

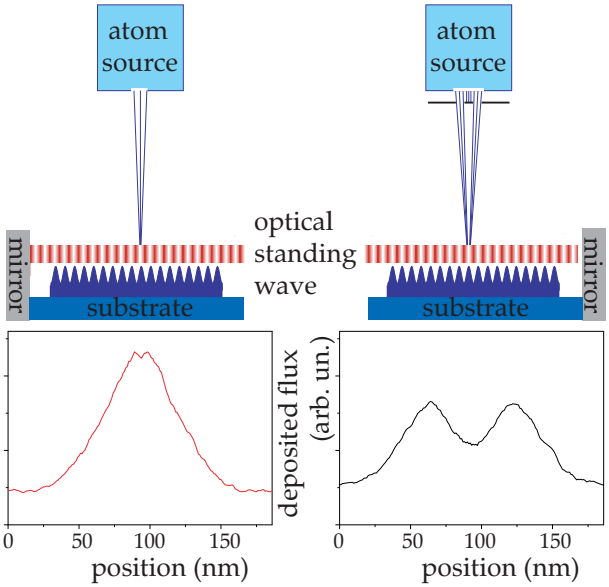

Figure 3.13: *Example of atom lithography using a patterned atom beam. Left top: atom beam impinging on a single SW lens from a 1 mm round source opening; Right top: atom beam impinging on a single SW lens from from two 0.33 mm sources positioned 0.75 mm apart. Bottom: Simulated atomic distribution after focussing of atom beams by a SW light field of $w = 150$ µm and $P = 55$ mW.*

Considering the typical w_h =80 nm of Fe on SiOx, our current setup is not very suitable for this type of experiment, as multiple features might not be discernable on an 186 nm interval. However, in atom lithography structures have been observed with sizes down to 13 nm in sodium [49] and down to 29 nm in chromium [43] allowing for more intricate patterns within the corresponding lens sizes of $\lambda_{Na}/2$ =295 nm and $\lambda_{Cr}/2$ =213 nm. More complex patterns would be possible if two perpendicular standing waves are used, creating a two dimensional array of lenses, which would allow for two dimensional patterning. This scheme will of course suffer from the large abberations that optical lenses for atoms have. Nevertheless, potential applications in the field of, e.g., nanoengineering and nanomagnetism could make this scheme technologically interesting.

Chapter 4

Magnetic effects in Fe_xNi_{1-x} layers

4.1 Introduction

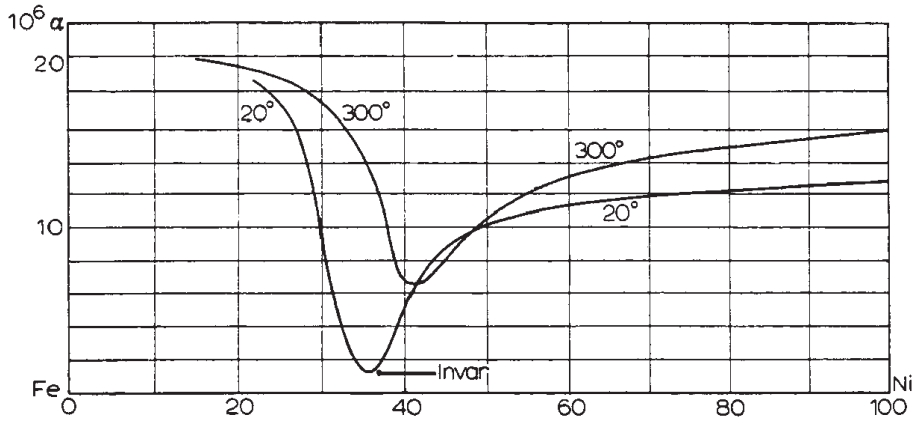

Figure 4.1: *Diagram showing the thermal expansion coefficient α of Fe_xNi_{1-x} as function of atomic nickel content for 20 °C and 300 °C. Image from the Nobel prize lecture of Ch. E. Guillaume in 1920 [50].*

Alloys of iron and nickel have been subject of extensive research, especially after the so-called Invar effect was first discovered in 1897 by Ch. E. Guillaume [51]. He found that around the $Fe_{65}Ni_{35}$ composition the thermal expansion of Fe_xNi_{1-x} alloys drops to nearly zero at room temperature, as shown in Figure 4.1. This had applications for more stable measurement standards and it has still many applications where stability over a broad temperature range is required. For his discoveries Guillaume received the Nobel prize in physics in 1920.

The Invar effect is coupled to magnetism, as it disappears when Fe_xNi_{1-x} is heated over the Curie temperature. In Figure 4.2 the magnetic moment per atom as function of Ni content is shown. The Fe_xNi_{1-x} alloy has two different crystal structures, body centered cubic (BCC) in the Fe rich phase (solid points) and face centered cubic

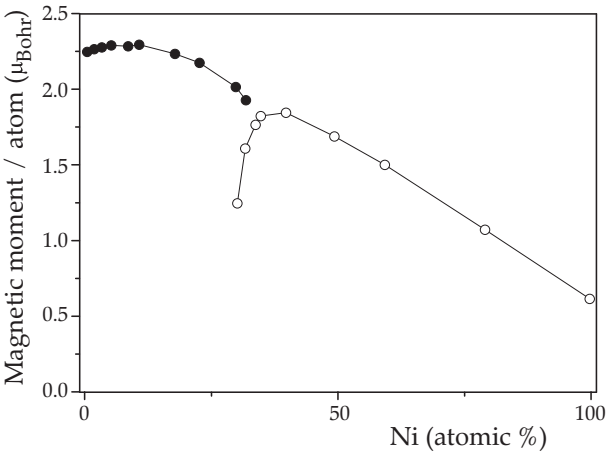

Figure 4.2: *Image adapted from Crangle and Hallam [53]: The variation of the magnetic moment per atom of BCC (solid points) and FCC (open points) with composition for* Fe_xNi_{1-x} .

(FCC) in the Ni rich phase (open points). Although the Invar effect occurs at compositions near the region where these phases coexist, the Invar effect was observed only in the FCC phase Fe_xNi_{1-x}. In Figure 4.2 it is visible as a sharp decrease in the magnetic moment per atom of the FCC phase near $Fe_{65}Ni_{35}$. Around this composition, two phases coexist in the FCC phase, one in which the Fe is ferromagnetic, having a larger atomic magnetic moment and a large volume and another in which Fe is anti-ferromagnetic having a small magnetic moment and a smaller volume. As temperature increases the relative amount of the low volume phase increases, thereby decreasing the thermal expansion. For increasing Fe content the relative amount of the anti-ferromagnetic phase also increases, decreasing the magnetic moment per atom as shown in Figure 4.2. An overview of the Invar effect is given by Wasserman in [52].

Although there are other interesting compositions of Fe_xNi_{1-x}, such as the so-called Permalloy around $Fe_{19}Ni_{81}$, where the magnetostriction vanishes [54], in this section only the region around $Fe_{65}Ni_{35}$ is considered. The deposition sources used for Fe and Ni, have higher deposition rates for Fe than for Ni, making the Invar region more accessible than the Permalloy region. In this section the magnetic properties are investigated of thin layers of pure Fe or Ni and Fe_xNi_{1-x} around the Invar region. This will allow for a better insight into the quality of the deposited magnetic materials and gives a reference for the structured layers created using atom lithography. It will also allow for testing of the effects of film thickness, film composition and interfaces.

In Chapter 5 the magnetic properties of atom lithographic structures are presented. As a reference experiment, here a method is devised to create magnetic layers of Fe_xNi_{1-x} that are modulated geometrically and in composition over length scales similar to those in atom lithography. This method uses shadow deposition of Fe and

Ni on periodically corrugated polymer films created using interference lithography. The corrugated substrate leads to shadow effects that modulate the height of the Fe_xNi_{1-x} layer. The composition of Fe_xNi_{1-x} is also periodically modulated, as one material of the alloy is deposited under an angle with respect to the substrate.

This chapter is organised as follows. First the magnetic properties are discussed of Fe and Ni layers and of Fe_xNi_{1-x} layers with various composition. Then the concept of shadow deposition is discussed and it is shown that this technique can indeed create locally modulated magnetic layers. Finally we show and discuss the magnetic anisotropic switching in the magnetic thin films created using shadow deposition.

4.2 Magnetic thin films.

Uniform magnetic thin films of Fe, Ni and FeNi are studied to test the influence of thickness and composition on the magnetic switching characteristics and saturation magnetisation. This will give information on the quality of the deposited layers and the deposition system, furthermore insight is gained enabling comparison of the unstructured thin films to structured thin films. Using effusive beam sources placed far from the surface, very thin layers of materials are deposited over long time spans, at rates of typically not more than 10 nm/hr. At the typical pressures in our deposition chamber of $5{\cdot}10^{-9}$ mbar, contaminations in our materials can be expected.

First Fe and Ni films are deposited on SiOx samples during two hours at deposition rates ranging from 10^{-1} to 10^{1} nm/hr. On top of these films a capping layer of Ag was deposited of 5 nm thickness. The deposition rates of the Fe and Ni sources was calibrated using Rutherford Back-scattering (RBS) as discussed in Chapter 2. The magnetic moment as a function of applied field of these samples was measured in a SQUID (superconducting quantum interference device) magnetometer, to obtain absolute values of the magnetic moment of each sample. The measurements at low applied fields give information on the switching characteristics of the materials. The quantitative values of the magnetic moment at high fields can be compared to the expected magnetic moment per unit volume of layers of pure Fe ($M_{sat} = 1.7$ MA/m) and Ni ($M_{sat} = 0.49$ MA/m) [27].

In Figure 4.3 the hysteresis curves measured with SQUID are shown for Fe on the left and for Ni on the right. To correct for the diamagnetic contribution of the sample, the magnetic moment was measured for applied fields up to $\mu_0 H = 5$ T. The magnetic moment for applied fields from $\mu_0 H = 0.8$ T up to $\mu_0 H = 5$ T was fitted linearly, where the intercept of the fit $\mu_0 H = 0$ T is the saturated magnetic moment, M_{sat}, and the linear term is subtracted from the measurements to correct for the diamagnetic contribution of the sample. Both Fe and Ni samples show ferromagnetic magnetization curves in the top of Figure 4.3. For each material three different curves are shown, corresponding to three typical deposition rates. While for Fe the deposition rate is controlled by setting the current to the heater of the deposition source, for

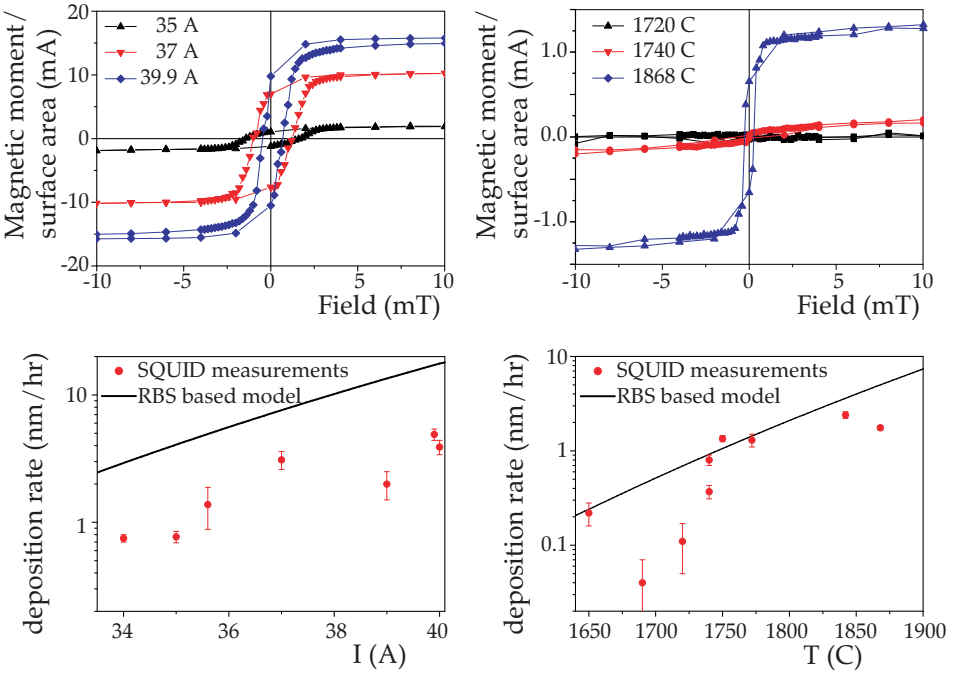

Figure 4.3: *Top: magnetic response of Fe (left) and Ni (right) measured with a SQUID magnetometer for layers of different deposition rates due to different heating currents for Fe or source temperatures for Ni. Note that the graphs are corrected for the background contribution. Bottom: comparison of deposition rates measured with RBS and deposited magnetic equivalent measured with SQUID.*

Ni the source temperature can be controlled directly, so values for current or temperature are indicated in the top images of Figure 4.3. The switch behavior of Fe and Ni is somewhat different. The Fe layers show a larger coercivity and are thus magnetically harder than the Ni layers. However, at the typical coercivities of 1 mT $\leq H_{c,Fe} \leq$ 2 mT and $H_{c,Ni} <$ 1 mT both materials are reasonably soft magnets.

For both Fe and Ni, Figure 4.3 reveals that a larger deposition rate corresponds to a larger saturated magnetic moment per unit surface area. From the values of the saturated magnetic moment per surface area, the deposited equivalent amount of pure bulk Fe or Ni is calculated, using their respective values for M_{sat}. In the lower graphs of Figure 4.3, the calculated magnetic equivalent deposition rates are compared to the real deposition rates based on RBS measurements discussed in Chapter 2. If both rates are similar, the deposited layers thus have the saturation magnetization of the bulk material.

In thin layers of Fe or Ni deposited at low deposition rates, various effects in either the bulk or at the interfaces can affect the saturation magnetisation of the samples. At the interfaces the atomic magnetic moment can be reduced due to effects of

surface roughness or contaminants at the substrate [55]. Contaminations should be limited on the cleaned SiOx substrates. However, also effects of inter-diffusion at the surface or hybridization of the electronic states of magnetic atoms over several monolayers at the interface [28] can limit the atomic magnetic moment. Inter-diffusion of Ag at the top surface is unlikely, as Ag is immiscible in Fe [56] and in Ni [57]. In the bulk of the sample, contaminations, especially oxygen, originating from either the background pressure or from the deposition sources, can limit the magnetic moment per atom, and also deviations from crystalline growth can decrease the magnetic moment per atom in Fe or Ni [58], but this is a smaller effect.

On the amorphous SiOx substrate it is likely that both Fe and Ni will not grow as mono-crystalline layers, although the crystalline structure of these layers has not been measured. Crystalline growth can be induced by growing on crystalline substrates, e.g., Cu$\langle 111 \rangle$ [59] or Si$\langle 100 \rangle$ [60]. However, these substrates do induce magneto-crystalline anisotropies in the layers which could interfere with the anisotropy effects that are expected in the atom lithographic deposited line structures. Therefore only SiOx is used as a substrate.

For Fe the SQUID results in Figure 4.3 show a similar trend as the real deposition rate, but the rates from the magnetic measurements are about four times lower than the RBS rates. We note that all samples are deposited over two hours, so that the higher deposition rates correspond to thicker magnetic layers. These results therefore indicate no surface effects, but a decrease in the saturation magnetisation of the bulk. In chapter 2 contaminations of the samples with carbon and oxygen were reported in RBS measurements, which will influence the magnetic moment of Fe, which is highly reactive to oxygen. Secondly, it is likely that the magnetic moment is also limited by deviations in the crystal structure of the Fe layers.

For Ni a different behaviour is found in Figure 4.3. For small expected deposition rates, less than 1 nm/hr, thus corresponding to layers of less than 2 nm high, the magnetisation is up to an order of magnitude smaller than expected. The values are also fluctuating and have large uncertainties due to the limited magnetic signal. At deposition rates larger than 1 nm/hr, the magnetic behaviour is similar to bulk Ni, supporting the notion of interface effects at low deposition rates, which are less relevant for thicker layers. The thicker layers of Ni are on average a factor of two off from the bulk behaviour, which is significantly better than Fe.

In Figure 4.3 both Fe and Ni show a non-monotonic increase of the amount of magnetic material for higher deposition rates, which is not within the indicated error margin resulting from the SQUID measurement. It was found that the magnetic moment of the bulk of both materials is decreased, most likely partly due to contaminations. We therefore conclude that contaminations can reduce the magnetisation of each layer, but that this reduction is not equal in each layer as the amount of contaminations is not fully controlled.

As it was shown in Figure 4.2, the magnetic moment per atom of Fe_xNi_{1-x} alloys shows a significant dip around $Fe_{35}Ni_{65}$ for the FCC phase. To investigate the behaviour, 6 samples of Fe_xNi_{1-x} layers of approximately 10 nm thick were deposited on

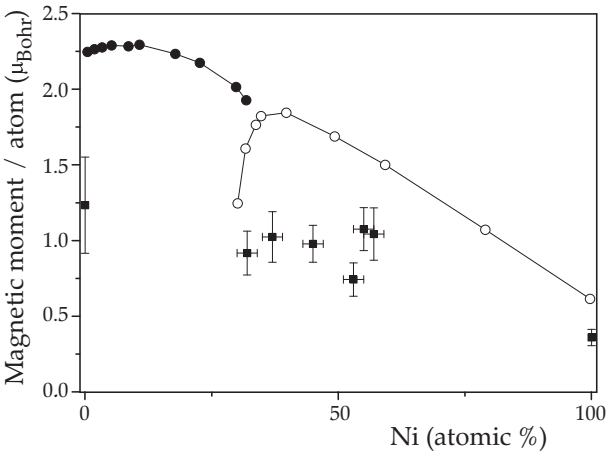

Figure 4.4: *Measured magnetic moment per atom of deposited Fe_xNi_{1-x} layers around the Invar concentration (solid squares). As a reference the data for BCC (solid dots and line) and FCC (open dots and line) phases from [53] are included.*

SiOx substrates, ranging from $Fe_{68}Ni_{32}$ to $Fe_{43}Ni_{57}$ and reference samples of pure Fe and Ni. The elemental composition and thickness was measured with RBS and the magnetic moment of the sample was determined with a SQUID magnetometer. All samples showed clear ferromagnetic behaviour. From the SQUID data the saturated magnetic moment per atom was calculated. The results are shown in Figure 4.4, presenting the measured atomic moments (filled squares) and the literature values for the BCC phase (filled dots) and the FCC phase (open dots). The comparison shows that the measured magnetic moment of the layers is significantly lower than the literature values for all compositions, similar to the results for pure Fe and Ni. There is no clear decrease in the magnetisation around the Invar composition. Additional measurements for compositions with lower Ni content could provide some more insight into any Invar effect, but as the samples are most likely contaminated and not mono-crystalline, it is not surprising that the Invar effect is not observed.

Concluding we can state that thin magnetic layers of Fe, Ni and Fe_xNi_{1-x} can be created over a height range of 10^{-1} to about 10 nm, but that these layers show a decreased magnetic moment per atom, probably due to the inclusion of contaminations in our layers and non mono-crystalline growth. For thin Ni layers, interface effects further limit the magnetic moment per atom.

4.3 Periodically structured magnetic thin films

In the previous section the magnetic properties of unstructured Fe, Ni and Fe_xNi_{1-x} thin layers were presented, which are a reference for the magnetic properties of Fe or Fe_xNi_{1-x} thin layers structured using atom lithography. These atom lithographic structures are presented in the next chapter. As a second reference for these atom lithographic structures, periodically modulated structures of thin layers of Fe_xNi_{1-x} have been created. To this end non-magnetic polymer layers are structured using interference lithography into line structures on length scales comparable to length scales typical in atom lithography. By depositing magnetic layers on top of these structures, magnetic layers are created that follow the geometric modulation of the polymer structures. Using shadow deposition of Fe_xNi_{1-x} alloys on these structures allows for the creation of a periodically modulated alloy composition, which is a novel technique.

In this section laser interference lithography is discussed as well as the geometry of the resulting structures. Then it is shown how shadow deposition allows for the creation of periodically modulated alloy compositions. Finally the magnetic properties of these structures are presented.

4.3.1 Laser interference lithography

Laser interference lithography is a technique to create large arrays of regular structures without the use of complex optics or masks. The basis is an interference pattern which is recorded into a photosensitive layer. Upon developing this photosensitive layer, the interference pattern emerges in the remaining photosensitive layer. This basic concept is shown in Figure 4.5.

In our experiments we use a negative photo-resist, which means that the areas not exposed to the light are washed away during the development, leaving the exposed areas in the developed structured layer. The photo-resist was SU8 [61] (available from MicroChem), a commonly used epoxy-based negative photo-resist, which has an exposure dose threshold of about 140 mJ/cm^2 [62]. Layers of sub-micron thickness were applied on glass substrates using spincoating. The interference pattern was generated using the setup shown in Figure 4.6 and described in more detail in [63]. A laser beam is split in two equal parts using a half wave plate and a polarising beam splitter, a second half wave plate aligns the polarisations of the two beams, that overlap and create an interference pattern on the sample. The laser beam is created from an Ar laser at 351 nm, expanded to approximately 1 cm diameter.

The period of the interference pattern is determined by the angle θ, between the two overlapping laser beams and the laser wavelength λ, leading to a period $p = \lambda/(2\sin(\theta/2))$. The lower limit on the period is therefore $p = \lambda/2$, for $\theta = 180°$.

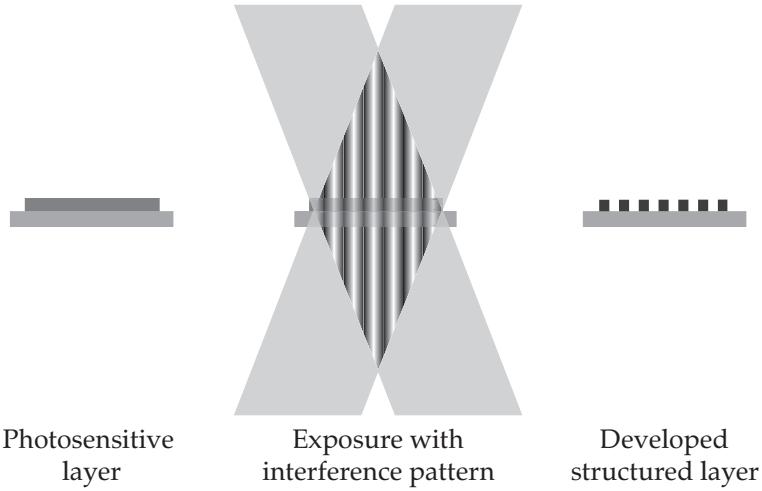

Figure 4.5: *Concept of interference lithography.*

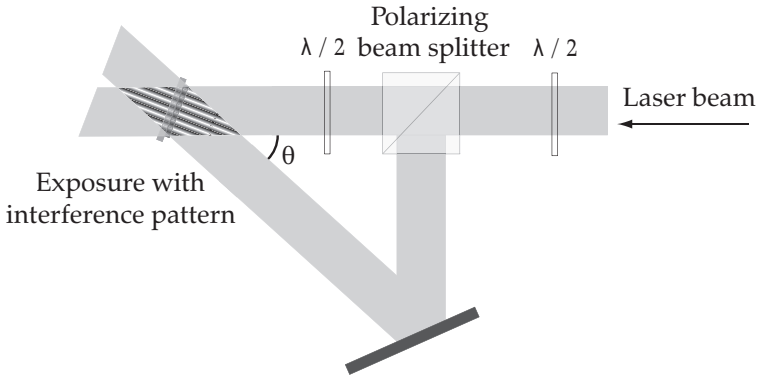

Figure 4.6: *Schematic overview of interference generation.*

However at very large angles reflections at the substrate surface also induce interference effects, limiting the effectiveness. Interference patterns have been created using angles of $\theta = 4\pm1^\circ$ and $\theta = 25\pm1^\circ$, leading to periods of $p = 5\pm2$ μm and $p = 0.81\pm0.03$ μm.

After the exposure the SU8 is heated for two minutes at 95° C, to fully cross-link the exposed SU8. The sample is then rinsed in SU8 developer (mr-dev 600, available from MicroChem) and in propanol to wash off any undeveloped SU8 and it is subsequently dried with nitrogen, leaving a polymerised mechanically stable structured layer. Diffraction measurements on the gratings with a HeNe laser gave periods of $p = 0.80\pm0.05$ μm and $p = 6.0\pm0.2$ μm, in agreement with the expected periods.

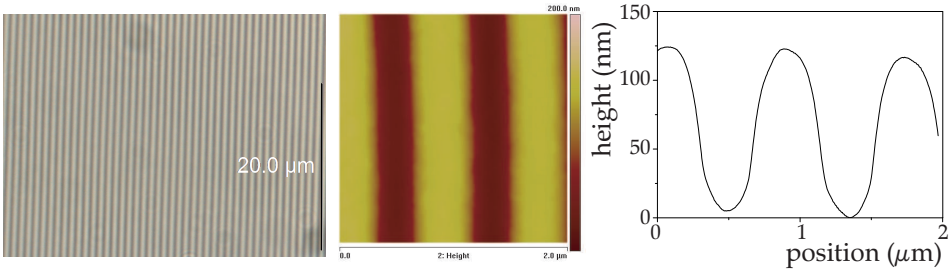

Figure 4.7: *SU8 grating with 0.8 µm spacing, from left to right: optical microscopy image of 40 × 30µm , AFM scan of 2 × 2 µm, height profile of the AFM scan.*

In Figure 4.7 we show a microscopy image and an AFM scan of one of the gratings made with $\theta = 25^\circ$ on glass. This confirms the periodicity of about $p = 0.80$ μm and shows the height to be around 100 nm. A visual inspection of the AFM scan shows that the edges of the lines are not straight, an analysis of the AFM scan on the top of the lines gives a surface roughness of 1.7$\pm$0.2 nm .

4.3.2 Depositing thin layers on corrugated surfaces: shadow deposition

When a thin layer is deposited on a periodically corrugated surface by an atom beam, the deposited layer will not only follow the shape of the corrugation, but it will also have periodic thickness variations dependent on the shape of the corrugation and the angle of the incoming atomic beam. This is schematically shown in Figure 4.8. On the left the atom beam is perpendicular to the global plane of the sample. In this case the height in vertical direction, h_z, is uniform over the entire sample. However, the thickness of the layer, defined as the height perpendicular to the local surface, $h_\perp$, is modulated. If the local surface of the corrugation has an angle α with respect to the global plane of the sample, the local height is decreased by a factor $\cos(\alpha)$.

In the center of Figure 4.8 an atom beam is deposited at an angle θ to the normal of the sample, while the projection of the atom beam is at an angle $\phi = 90^\circ$. In this case h_z is proportional to $\cos(\theta - \alpha)$. In the case that $\mid \theta - \alpha \mid > \pi/2$, there is a complete shadow effect and areas of the sample will not be reached by the atom beam. As the corrugation is drawn such that its right flank is parallel to the incoming atom beam, there is no material deposited on that flank, while deposition is maximal on the left flank of each corrugation both for h_z and $h_\perp$.

To test the concept of shadow deposition, layers of Fe_xNi_{1-x} are deposited on SU8 grating structures. Fe_xNi_{1-x} is deposited using two separate atom beams for Fe and Ni. Fe is deposited normal to the substrate, $\theta = 0^\circ$, while Ni is deposited at $\theta = 45^\circ$, $\phi = 90^\circ$, so that the line structures are positioned similar to the center of Figure 4.8. A layer of Fe_xNi_{1-x} is deposited with an expected average thickness of 10 nm and an expected average Fe:Ni ratio of 45:55.

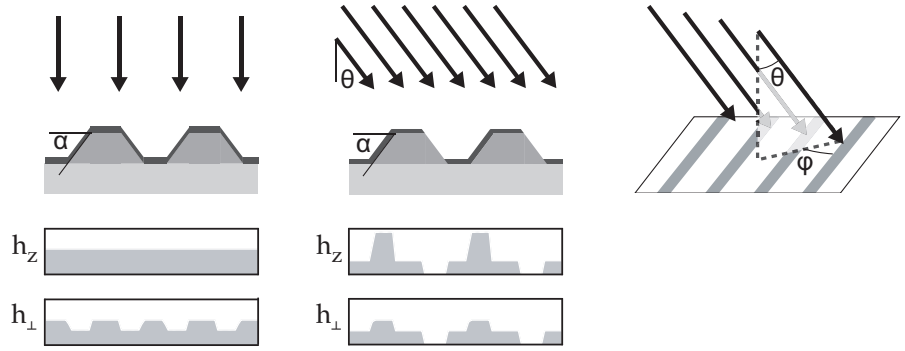

Figure 4.8: *Schematic representation of shadow deposition. Left: an atom beam is coming in perpendicular to a corrugated sample, leading to a uniform h_z, but a modulation in $h_\perp$. Center: the atom beam has an angle θ , leading to modulated h_z and $h_\perp$. Right: schematic representation of the atom beam on the corrugated sample, indicating θ and ϕ.*

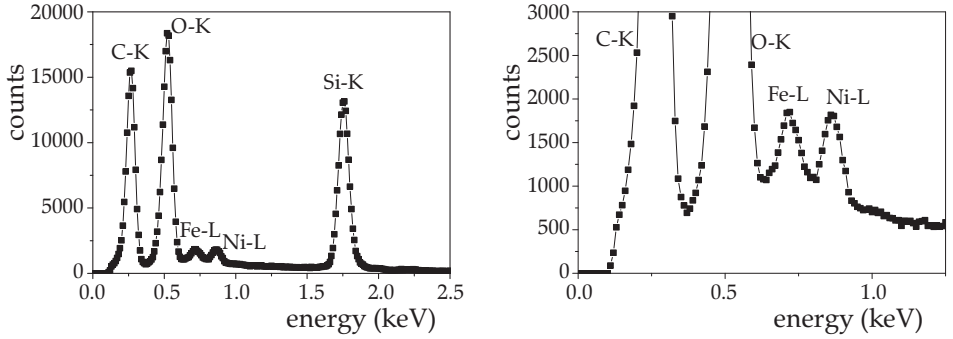

Figure 4.9: *SEM-EDX energy scan of a sample of 10 nm of Fe_xNi_{1-x} deposited on a SU8 grating on a SiOx substrate, resolving separate signals for C, O, Fe, Ni and Si. Left: full scan from 0 to 2.5 keV. Right: zoom from 0 to 1.25 keV.*

The local composition of Fe_xNi_{1-x} on the sample is measured using SEM-EDX (Scanning Electron Microscope - Energy Dispersive X-ray Spectrometry), a technique in which a beam of electrons is focussed onto a solid state sample, resulting in a a Brehmsstrahlung background signal and characteristic X-rays being emitted from the atomic species in the sample, which allow for elemental analysis. SU8 line structures on SiOx samples were used instead of SU8 on glass samples, so that in the elemental analysis only Fe, Ni, Si, O and C from the SU8 is expected. In Figure 4.9 we show an SEM-EDX energy scan of the sample, where peaks attributable to carbon (C-K), oxygen (O-K), iron (Fe-L), nickel (Ni-L) and silicon (Si-K) are clearly resolved in the left image. In the right image a zoom of the energy scan from 0 to 1.25 keV reveals more clearly the iron and nickel peaks on the Brehmsstrahlung background.

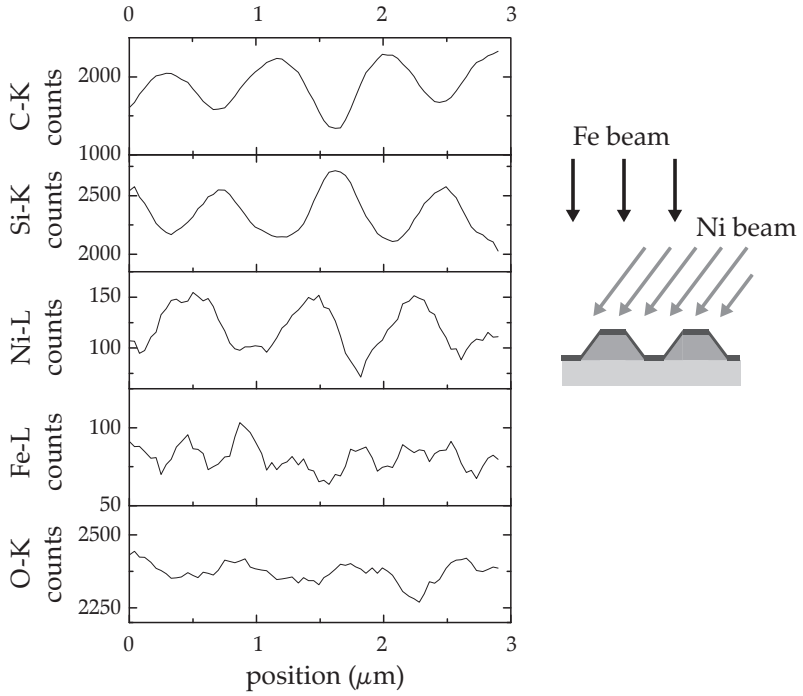

Figure 4.10: *SEM-EDX line scan over SU8 line structures on SiOx with period $p = 0.8$ μm coated with 10 nm of $Fe_{45}Ni_{55}$, measuring local background corrected C, Si, Ni, Fe and O signals. Note that all vertical axes have different offsets and scales. Inset on the right shows the orientation of Fe and Ni beams relative to the SU8 structures.*

The spatial resolution of SEM-EDX is limited by various factors, not only the size of the focused electron beam. The focused electron beam can penetrate and scatter through the sample, limiting the spatial resolution. As the thickness of the Fe_xNi_{1-x} layer is limited to about 10 nm, scattering in this layer is limited and the spatial resolution should therefore be smaller than the period of the SU8 grating. In Figure 4.10 a SEM-EDX line scan is presented over 2.9 μm perpendicular to the lines, where the signals are corrected for the Brehmsstrahung background.

The periodicity $p = 0.8$ μm of the structures is clearly visible in the C-K signal due to the carbon in the SU8. The C-K and Si-K signal are out of phase, as the SU8 structures shield the underlying SiOx substrate. Comparing the C-K and Ni-L signal shows that more nickel is present on the right flanks of the SU8 structures, confirming the concept of shadow deposition. The Fe-L signal shows no clear periodicity. In Figure 4.8, it is shown that a layer deposited at $\theta = 0°$, should have a uniform h_z, but a modulated $h_\perp$. In SEM-EDX measurements an electron beams is coming in normal to the sample and then electrons can scatter through the sample. It is therefore not a priori clear whether the signal for Fe-L should resemble h_z or $h_\perp$, or a combination of the two, so that the resulting lack of clear periodicity is not surprising. The O-K signal has a very faint periodicity, which is out of phase with the Ni-L

signal. This is probably due to shielding of the oxygen in the SU8 layer and the SiOx substrate.

The SEM-EDX scan also allows for an accurate quantitative analysis of the relative content of Fe and Ni. The Fe and Ni relative intensities are corrected for the Bremsstrahlung. However, in a binary mixture the relative intensity of the X-ray counts of an atomic species is not exactly proportional to the relative atomic content. Corrections need to be based on calibration curves based on reference measurements of well defined, comparable samples at the same conditions, which are difficult to create for our multilayer system. However, for Fe_xNi_{1-x} these corrections on the relative atomic content are known for another setup and sample, where they a less than 5 percentage points [64]. Comparing the signals corrected for the Bremsstrahlung background, we find that the spatially averaged relative intensities of the Fe-L and Ni-L signals is $I_{Ni}/I_{Fe} = 1.2 \pm 0.1$, which is the known relative composition of the sample. The background corrected relative intensities are therefore used as values for the relative composition without any further correction.

The local height of the samples measured with SEM-EDX has also been measured with AFM, using AFM tips with a radius of curvature of less than 10 nm and a full tip cone angle of less than 30° to limit tip artefacts. The AFM height data allow the modelling of the expected Fe_xNi_{1-x} concentration modulation, based on the geometry and the assumption that materials do not diffuse, using the known average Fe:Ni content of 45:55. This geometric model was already shown in Figure 4.8. In Figure 4.11 the comparison is shown of the modelled and measured Ni content in Fe_xNi_{1-x}. On the left the AFM height measurement (top) and the resulting expected Ni concentration in Fe_xNi_{1-x} are shown. On the right the results are presented of SEM-EDX measurements, using the C-K line signal (top) as a reference for the position of the SU8 structure and at the bottom the measured Ni concentration in Fe_xNi_{1-x} is given.

The results of Figure 4.11 show that shadow deposition is a method able to create thin Fe_xNi_{1-x} layers which are periodically modulated in composition. In the SEM-EDX measurements the relative Ni content is in a 46 to 69 % range, where the modelled values range from 35 to 70%. There are two main reasons for the difference. Firstly the model does not include any diffusion of material, which could lead to a decrease in the modulation. Secondly, it was already pointed out that SEM-EDX has a limited lateral resolution, limiting the measurements of highly localized composition changes.

In conclusion, we have created periodic corrugations of SU8 which can be used for shadow deposition and indeed allow for periodic modulation of the composition of a layer of FeNi. A model has been created which gives a reasonable indication of the range over which the local composition changes and this has been verified using SEM-EDX.

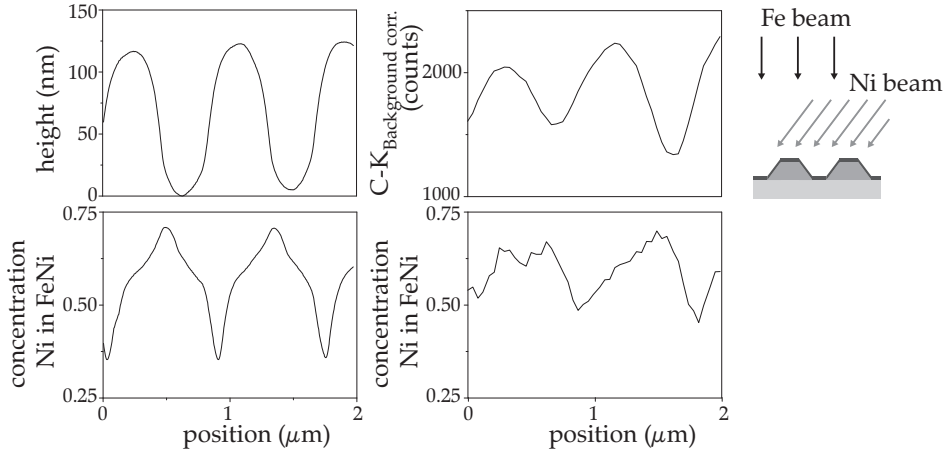

Figure 4.11: *Comparison of modelled and measured Ni concentrations in shadow deposited FeNi. Left: orientation of Fe and Ni beams relative to the SU8 structures during deposition. Top center: Height of SU8 structures measured with AFM. Bottom center: Modelled Ni concentration in FeNi in geometric model of shadow deposition. Top right: SEM-EDX measurement of carbon as a reference for the position of the SU8 structures. Bottom right: SEM-EDX measurement of Ni in FeNi.*

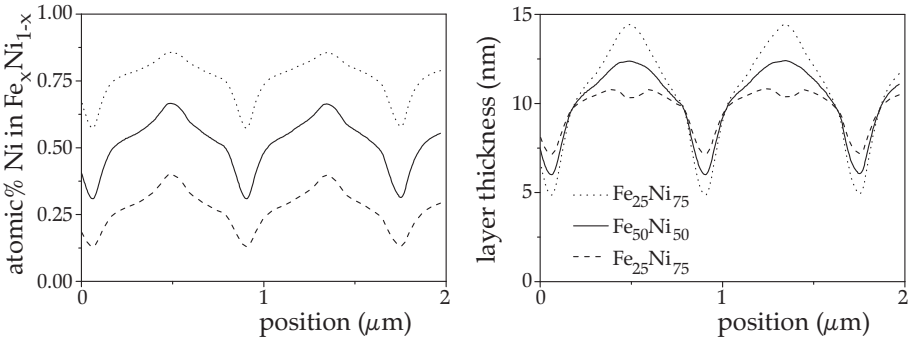

Figure 4.12: *Expected local concentration ranges (left) and local heights (right) of on average 10 nm thick layers of $Fe_{25}Ni_{75}$ (dotted line), $Fe_{50}Ni_{50}$ (solid line) and $Fe_{75}Ni_{25}$ (dashed line)*

4.3.3 Magnetic anisotropy in structured layers

We have investigated the magnetic properties of Fe_xNi_{1-x} layers deposited using shadow deposition. To find effects of the relative concentrations, 10 nm thick layers of $Fe_{25}Ni_{75}$, $Fe_{50}Ni_{50}$ and $Fe_{75}Ni_{25}$ have been deposited on SU8 structures with period $p = 0.80$ μm. Fe is deposited normal to the substrate, $\theta = 0^\circ$, while Ni is deposited at $\theta = 45^\circ$, $\phi = 90^\circ$. On the left of Figure 4.12 the local concentrations based on the geometry of the SU8 structures are shown. These three Fe_xNi_{1-x} layers give two ranges near and crossing the Invar concentration of $Fe_{35}Ni_{65}$ and one range far from that point. On the right of Figure 4.12 the height variations of the deposited Fe_xNi_{1-x} layers are presented. As the Ni is more structured in the shadow deposition than the Fe, the height variations are larger for Ni richer alloys.

To measure the magnetic properties of these layers, they have been measured using MOKE (Magneto-Optical Kerr Effect). The MOKE setup uses a laser setup of a linearly polarised HeNe laser of wavelength ($\lambda = 632.8$ nm) focused to a waist of about 100 μm on the sample. An in-plane magnetic field $\vec{H}$ is applied parallel or perpendicular to the line direction of the structured layers. The polarised light is reflected off the sample and the Kerr rotation is measured to obtain a value for the magnetisation of the sample. To prevent corrosion and contamination of the magnetic layers from either the polymer layer or the air, layers of 5 nm Ta or Pt were deposited in between the polymer and the magnetic layer and an Ag layer of 5 nm on top of the magnetic layer. In Figure 4.13 the hysteresis curves are shown of samples with intermediate layers of 5 nm Ta (A and B) and Pt (C and D) and average compositions of $Fe_{75}Ni_{25}$ (A), $Fe_{50}Ni_{50}$ (B and C) and $Fe_{25}Ni_{75}$ (D). These magnetic layers all show similar behavior. The hysteresis curve for $\vec{H}$ along the direction of the lines is square, indicating an easy axis, while for $\vec{H}$ perpendicular to the line direction we find a diagonal curve with vanishing coercivity corresponding to a hard axis. This is the behavior that is expected for line structures, as was shown in Chapter 1.

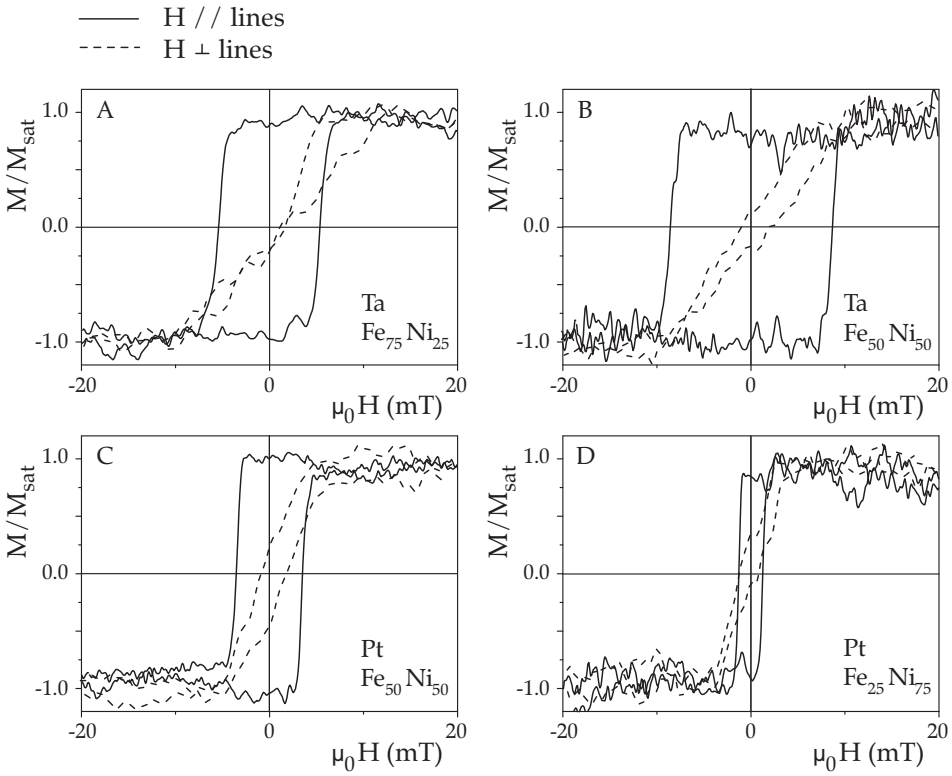

Figure 4.13: *MOKE switching behaviour of shadow deposited magnetic layers on $p = 0.80$ µm SU8 gratings, parallel to the lines (solid lines) or perpendicular to the lines (dashed lines). Intermediate layers of 5 nm Ta (A and B) and Pt (C and D) are used and average compositions of $Fe_{75}Ni_{25}$ (A), $Fe_{50}Ni_{50}$ (B and C) and $Fe_{25}Ni_{75}$ (D).*

Although the direction of hard and easy axes is similar for all samples in Figure 4.13, the coercive field for the easy axis ranges from 1.3 mT to 8.6 mT, which is nearly an order of magnitude difference. The coercive field is a value that is difficult to interpret, especially in these complex multilayer system of polymer - Ta or Pt - Fe_xNi_{1-x} - Ag layer. To find the influence of the intermediate layer on the coercivity we can compare Figure 4.13 B and C, whereas a comparison of Figure 4.13 A and B or C and D gives information of the influence of the Fe_xNi_{1-x} composition. This indicates that the influence of the intermediate layer on the coercivity is comparable to that of the Fe_xNi_{1-x} composition.

The intermediate layer is grown on the SU8 layer, which is a non-crystalline polymer, which has a roughness of 1.7 ± 0.2 nm at the top surfaces and no smooth edges as was found in the AFM scan of Figure 4.7. The intermediate layers can therefore not grow epitaxially and the layers of only 5 nm thickness will most likely be polycrystalline. It is therefore likely that the magnetic layers are also polycrystalline, so that magneto-crystalline anisotropies will not exist in our samples.

As the surface energy of Ta (3.05 mJm^{-2}[65]) is significantly larger than that of Pt (2.55 mJm^{-2} [65]), the Ta film will grow into a smoother layer than the Pt layer. Comparing the surface energies of Fe (2.55 mJm^{-2}[65]) and Ni (2.45 mJm^{-2}[65]) to Ta and Pt, we find that Fe and Ni are also more wetting on Ta than on Pt. It is therefore likely that the Fe_xNi_{1-x} layers will be less rough on the Ta intermediate layer than on Pt. As the anisotropy is decreased by roughness [66], it is expected that the anisotropy and thereby the coercivity of the Fe_xNi_{1-x} layers on Ta will be larger than on Pt.

The influence of the average Fe_xNi_{1-x} composition on the coercivity is difficult to assess. It influences the saturation magnetisation as shown in Figure 4.4. However in Figure 4.12 the average Fe_xNi_{1-x} composition also influences both the height modulation and the composition modulation. Based on the results from Figure 4.13, these effects cannot be separated clearly. In Figure 4.4 the saturation magnetisation for Ni rich compounds is lower than for Fe rich compounds. The small coercivity in Figure 4.13 D ($Fe_{25}Ni_{75}$), compared to Figure 4.13 C ($Fe_{50}Ni_{50}$), could thus be explained based on a smaller saturation magnetization of the Ni rich compound, leading to a smaller coercivity [27]. The smaller coercivity in Figure 4.13 A ($Fe_{75}Ni_{25}$), compared to Figure 4.13 B ($Fe_{50}Ni_{50}$), cannot be explained based on the saturation magnetization. The coercivity of these layers is thus influenced not only by the average composition, but also by the modulation.

From Figure 4.13 it was shown that the periodicity in geometry and composition of the magnetic layers induces an in-plane easy axis. To understand the effect of the periodicity, $Fe_{50}Ni_{50}$ layers were shadow deposited on SU8 structures with $p =$ 0.80 μm and $p = 6.0$ μm. Furthermore the effect of the composition modulation was minimised by depositing Fe at $\theta = 0^\circ$ and Ni at $\theta = 45^\circ$, $\phi = 0^\circ$, minimising the modulation of the Ni content due to shadow effects. For all samples, 10 nm of $Fe_{50}Ni_{50}$ was deposited on top of SU8 structures with an intermediate layer of Ta.

In Figure 4.14 the results are presented of MOKE measurements on $p = 0.80$ μm structures with Ni modulation (top), $p = 6.0$ μm structures with Ni modulation (middle) and $p = 6.0$ μm structures without Ni modulation (bottom). The magnetization is measured along $\vec{H}$ which was either parallel, at 45° or orthogonal to the line direction. In Figure 4.13 it was already found that the $p = 0.80$ μm structures have a clear easy axis along the direction of the lines and a hard axis perpendicular to the line. However for the $p = 6.0$ μm structures this behavior is less pronounced. The anisotropy thus decreases if the number of periods per unit length decreases. This is expected as the anisotropy vanishes for the situation of zero periods per unit length. A more complex effect is that of Ni concentration modulation. In the lower two rows of Figure 4.14 we find that the effect of alloy composition is small compared to the effect of periodicity. Comparing the coercivities of the Ni modulated results of the middle row, along the line direction $H_{C,\,par} = 2.2\pm0.1$ mT and measured perpendicular to the line direction $H_{C,\,perp} = 1.2\pm0.1$ mT. For the structures without Ni modulation in the lower row $H_{C,\,par} = 1.8\pm0.1$ mT and $H_{C,\,perp} = 1.4\pm0.1$ mT. The Ni modulated samples thus has a more pronounced easy-axis along the direction of

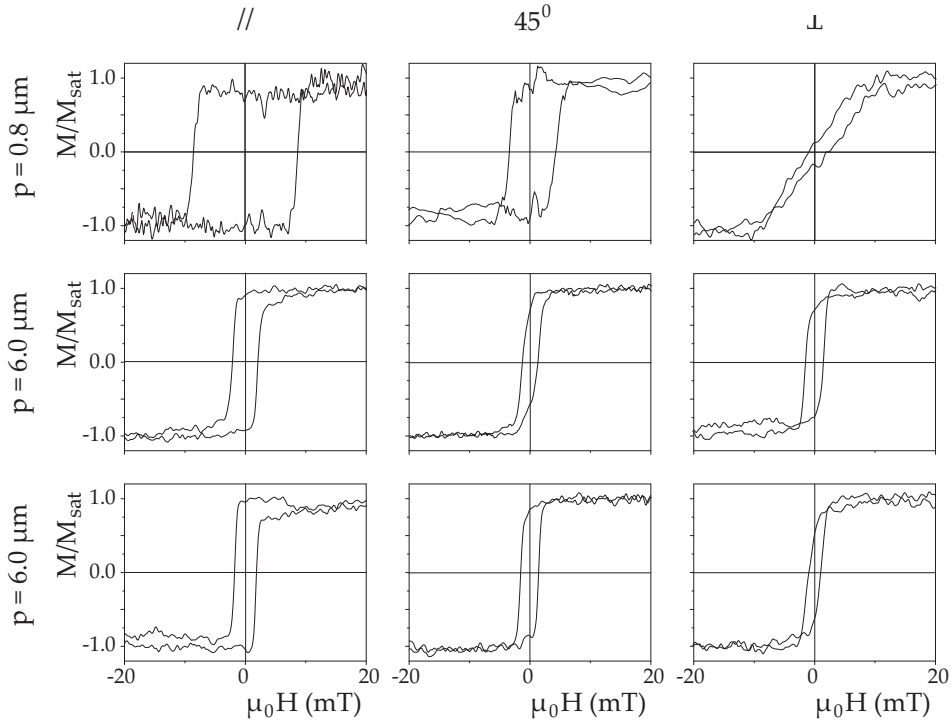

Figure 4.14: *MOKE switching behavior of shadow deposited 10nm thick $Fe_{50}Ni_{50}$ layers on 5 nm Ta intermediate layer on SU8 gratings with $p = 0.80$ µm (top row) and $p = 6.0$ µm (middle and bottom row), with modulation in Ni (top and middle row) or without Ni modulation (bottom row). The applied field and measured magnetization were measured parallel to the SU8 lines (solid lines, left column), at 45° (dotted lines, middle column) or perpendicular to the lines (dashed lines, right column).*

the lines, but the easy axis is also present when a layer of almost uniform composition is deposited on top of a substrate with a line pattern. Further investigations of non-modulated samples with small periods can provide more information on the relative strength of these effects.

We have shown that the concept of shadow deposition of magnetic Fe_xNi_{1-x} layers on pre-patterned SU8 structures can be used to induce an easy axis along the direction of the lines. The magnetic properties are dependent on the Fe_xNi_{1-x} composition, the intermediate layer and the periodicity of the structures. The easy axis behavior is due to both the geometric effect of depositing a layer on top of line structures, as well as the period modulation of the composition due to shadow deposition.

4.4 Comparing atom lithographic and shadow deposited structures.

In the previous paragraph the magnetic properties of samples created using interference lithography and shadow deposition were presented, that are a reference for atom lithographic structures, whose magnetic properties are subject of the following chapter. The anisotropy in the shadow lithographic magnetic structures is a clear reference point for the evaluation of the magnetism in atom lithographic structures. In this paragraph both types of structures are compared, to find out how well results should compare. Secondly the production techniques are compared to see what the advantages and disadvantages of each technique is for future applications.

In Figure 4.15 the geometries are compared of structures created using atom lithography with structures created with interference lithography and shadow deposition. The AFM scans give the geometries for atom lithographic Fe structures and interference lithographic SU8 structures. The geometries are somewhat similar, although the interference lithography has a larger period ($p = 0.80$ μm) compared to atom lithography ($p = 0.2$ μm) and the modulation height for interference lithographic structures is more than an order of magnitude larger then the modulation for atom lithographic structures. However, the real comparison should be between the atom lithographic Fe layer, and the Fe_xNi_{1-x} layer created with shadow deposition. This is shown on the right of Figure 4.15.

Atom lithographic Fe structures are almost flat, with nanolines of a few nanometer high on top of flat background of about 10 nm high, whereas the Fe_xNi_{1-x} layer is deposited on top of the SU8 structures which have a >100 nm high modulation. From a magnetic point of view the complexity of the shadow lithographic structures is much greater as it uses a multilayer sandwich of polymer structure - intermediate layer - magnetic layer - capping layer to create the structure, whereas atom lithography creates a single structured layer from a single material. However, we have shown in Figure 4.12 that the local thickness of the Fe_xNi_{1-x} has a modulation of less than 10 nm for a total average height of 10 nm, which is similar to atom lithographic

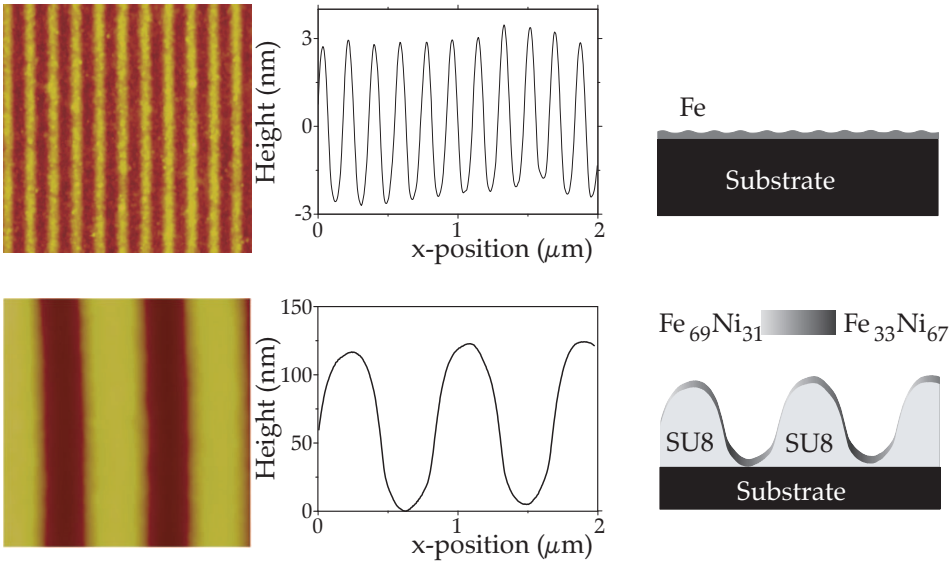

Figure 4.15: *Left: AFM measurements over 2 × 2 µm area of the geometry of atom lithographic structures (top) and SU8 structures with p = 0.80 µm created with interference lithography (bottom). Middle: corresponding height cross-sections. Right: Schematical representation of atom lithographic Fe structures and shadow lithographic $Fe_{50}Ni_{50}$ structures on top of SU8 structures, both on identical height scales (note the different horizontal and vertical scales).*

structures. As the magnetic easy-axis behavior along the length of the lines of the shadow lithographic structures is also more explicit for small period structures, this behavior is a reasonable reference for the atom lithographic structures, which have an even smaller period.

As a thin film structuring technique, interference lithography has parallels to atom lithography, as both reproduce an interference pattern created in light into a physical pattern. The working principle of both techniques is very different, which has large implications for the speed, flexibility and complexity of the techniques. Atom lithography is based on interactions of neutral atoms with near resonant light, using standing wave laser fields to create "lenses" for the atom beam, which requires tuning of laser frequencies within the MHz range. In interference lithography, the standing wave field is used to locally excite photo-initiators, allowing for the laser wavelength to deviate over a frequency range 10^6 wider than allowed in atom lithography. A second issue is writing speed. In interference lithography a pattern is written if an area has received an exposure over a threshold value of typically 0.1 J/cm^2, so that a 1 cm^2 sample can be written in 0.1 s with a laser power of 1 W, corresponding to a writing speed on the order of 10^{-3} m^2/s. For atom lithography, the writing speed is determined by the atom flux. In our setup, typical exposure times are two hours, resulting in deposited layers of 15 nm. However, patterning is only present over the area where the standing wave is present, which is about 0.2 mm wide and 5 mm

long, resulting in a writing speed of 0.5 mm^2/hr or 10^{-10} m^2/s, thus seven orders of magnitude slower than interference lithography. In interference lithography a pattern is written in a continuous undeveloped polymer layer of arbitrary thickness, which allows for consecutive writing of multiple patterns in one layer before development, without disturbing the other patterns. It also allows for the creation of structures of higher aspect ratios (height / width >10), whereas atom lithography suffers from fundamental limits to focusing and surface interactions leading to smooth structures with limited aspect ratio's (height/ width <<1).

However, if magnetic layers are required, atom lithography is a single step process to create a magnetic layer, where the patterning is created during the deposition of the material. In interference lithography the pattern is only revealed after exposure and development of a photosensitive layer and to obtain magnetic layers, an additional step is needed to deposit the intermediate and magnetic layers on top of the structured polymer layer. If this is done in the same setup used for atom lithography, the interference lithography / shadow deposition scheme is by definition a slower route as it requires the same amount of time to deposit the magnetic layer only, while all other steps require additional time. Of course it should be noted that our setup for atom lithography requires the deposition sources to be very far from the samples, creating low deposition rates and long deposition times, whereas for shadow deposition a more compact setup with much higher deposition rates could be achievable.

Compared to atom lithography, interference lithography is a much faster and more flexible option to create structures, but to create magnetic structures with shadow deposition is in fact a slower process in our current setup. As the magnetic structures are only moderately similar in geometry, and shadow deposition creates complex multilayers, any comparison of the structures will not be straightforward. Nevertheless the magnetic easy-axis behavior along the length of the lines of the shadow lithographic structures is a good starting point for the interpretation of atom lithographic structures in the following chapter.

4.5 Conclusions

In this section we have shown that our setup is able to create ultra thin ferromagnetic layers of Fe, Ni and Fe_xNi_{1-x}. These structures have a significantly decreased magnetic moment compared to literature values for bulk materials, especially the Fe rich compounds. This is probably a result of contaminations and deviations from mono-crystalline growth, while Ni layers thinner than 2 nm have a decreased magnetic moment due to interactions at the interfaces.

We have also shown that using shadow deposition on arrays of nanolines of SU8 created using interference lithography, we can create Fe_xNi_{1-x} layers that follow the geometry of the nanowires and are periodically modulated in alloy composition. This periodic modulation has been shown down to the sub-micron level using SEM-EDX. These structures show a magnetic anisotropy with an easy axis along the direction of the lines. The anisotropy is influenced by the intermediate layer between the SU8 and the Fe_xNi_{1-x}, where Ta allows for a larger anisotropy than Pt. The anisotropy is also dependent on the period of the line structures, with a smaller period leading to a larger anisotropy. We have also found that the periodic modulation of the atomic content enhances the easy axis along the direction of the lines.

Interference lithography and shadow deposition are shown to be suitable to create magnetic structures which can be used as a reference to the atom lithographic structures. Although shadow deposition does not create the exact same structures as atom lithography, the results of this chapter form a basis for the interpretation of the magnetic effects of atom lithographic structures discussed in the next chapter.

Chapter 5

Magnetic effects in atom lithographic nanostructures

5.1 Introduction

In this chapter we report on the first magnetic signature of structuring of thin iron layers using atom lithography. Over the last two decades, surface structuring using atom lithography has received considerable attention. It uses the dipolar interaction of near-resonant light fields and neutral atom beams, to focus atom beams while they are deposited on a sample into patterns using standing wave light fields. As atom lithography is a single step process, it allows for the deposition of magnetic layers without contamination of etching or rinsing processes. Because standing wave light fields as arrays of lenses to focus atom beams, the structures are highly periodic with a period of e.g., $\lambda/2$, over large areas. Atom lithography is thus a good candidate to produce magnetic nanostructures given its typical length scales, the periodicity and the ability to create clean structures, however, magnetic signatures of structures created with atom lithography of Fe have not yet been reported.

The first experiments in atom lithography were performed with sodium by Timp et al. [7] and in chromium by McClelland [15]. As light fields are required that are near-resonant with an atomic transition, the use of atom lithography with ferromagnetic elements such as Fe, Ni, Co is technologically challenging as near-resonant light sources for these elements are not readily available [25]. The first magnetic structures based on atom lithography were therefore created in a two-step process by Tulchinsky et al. [67]. An atom lithographic Cr array of nanolines was used a mask for shadow lithography, where Fe was deposited at grazing angles so that Fe nanolines were deposited on the flanks of the Cr nanolines.

In 2004 iron was the first ferromagnetic material used directly in atom lithography. Two separate groups in Eindhoven [18] and Nijmegen [19] created iron structures in the form of arrays of nanolines on top of a background layer of iron. However, no magnetic signature of the structuring has yet been found, although the magnetic properties of these structures were investigated by MOKE and MFM by both Myszkiewicz et al. in Nijmegen [19] and Smeets et al. in Eindhoven [25]. The lack of clear magnetic signature was ascribed to the presence of a magnetic Fe background layer [19] and to the presence of a substrate-induced magnetic anisotropy [25].

To find effects of the structuring, we have created arrays of Fe nanolines with atom lithography on SiOx samples. As these are non-crystalline, magneto-crystalline anisotropies in the background layer are unlikely. Using MOKE microscopy the local magnetic switching behaviour was determined in a large field of view, allowing for direct comparison of the structured and unstructured areas. This provided clear and reproducible evidence that the switching behaviour of atom lithographic nanolines differs from the background. We also show that, in retrospect, previously unpublished hysteresis curves obtained by Smeets using traditional MOKE already hint at this.

This chapter is organised as follows: first the atom lithographic structures are discussed and our setup and structures are compared to those presented in literature. Then unpublished results by Smeets et al. are shown that hint at effects of atom lithographic structuring on the magnetic properties of Fe thin films. We will present our MOKE microscopy results for samples with a Fe layer of 15 nm average height, similar to those described in Chapter 3. These samples show a clear influence of the structuring on the magnetic properties, but these samples show no clear anisotropy. Further MOKE results for thicker samples of 30 nm height are given, showing anisotropy in the structured area with magnetic easy axes both parallel and perpendicular to the line directions. We will present micromagnetic simulations and a literature overview indicating that a uniaxial behaviour is expected in line structures, however we will discuss possible mechanisms for the observed behaviour. Finally some first results of co-deposition are presented, where Fe_xNi_{1-x} structures are created where the Fe content is modulated while the Ni is uniformly deposited.

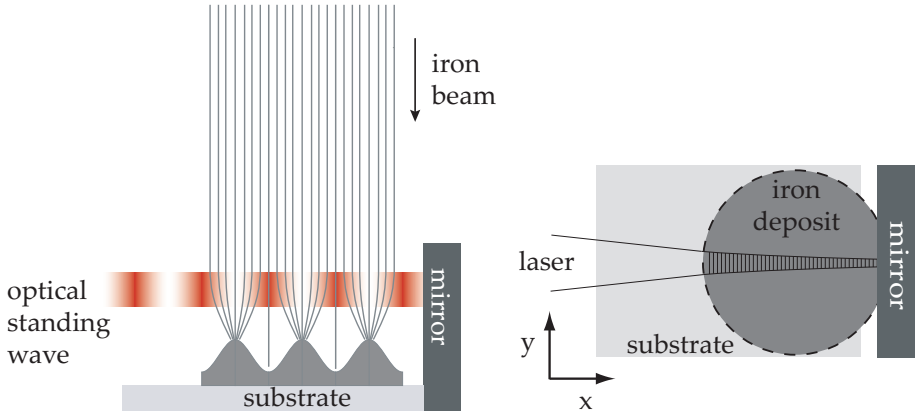

Figure 5.1: *Schematic representation of atom lithography. Left: focusing of beam of iron atom into nanolines on a substrate by a standing wave light field. Right: Position of atom lithographic structures on a sample, where the iron beam and laser overlap.*

5.2 Atom lithography of Fe nanolines

Atom lithography has been reviewed in various articles [36, 68] and the deposition of Fe nanolines using atom lithography without laser cooling has been described in Chapter 3. In this section we only recall the typical geometry of the samples we create with the techniques described in Chapter 3. Furthermore the geometric effects of capping samples with Ag are shown and a comparison is made between our setup and samples and those of Myszkiewicz et al. [19] and Smeets et al. [25].

The basis of atom lithography is shown in Figure 5.1. On the left-hand side a beam of iron atoms is focused by a standing wave of near-resonant light into lines on a substrate spaced $\lambda/2$, which in our case is 186 nm. On the right-hand side the view is along the atom beam, indicating the area where the standing wave laser field and the Fe atom beam overlap and nanoline structures are formed. The width of this structured area is determined by the size and power of the laser beam, which has a waist of about $w = 90$ μm and a power of about $P = 20$ mW in all experiments of this chapter. The resulting structured area is about 200 μm wide. The length of this structured area can be several mm long, limited by the typical size of the SiOx substrates of 5 $\times$ 8 mm. The samples thus contain arrays of over 10^4 parallel lines of 200 μm long. The image on the right-hand side of Figure 5.1 is used throughout this chapter to indicate the position of measurements on a sample relative to the atom lithographic structuring.

In Chapter 3 Fe nanostructures are presented without any corrosion protective capping. However, to be able to measure the magnetic behaviour, an Ag source is used to cap our samples with about 8 nm of Ag at a deposition rate of 1.5 nm per minute. This additional capping step has significant effects on the height of the lines

measured using atomic force microscopy (AFM). In Figure 5.2 AFM surface scans of three samples are shown. All samples have SiOx substrate, Fe is deposited at a rate of about 7.5 nm / hr and structuring is performed with similar light fields. One sample is deposited with 15 nm of Fe without capping layer, previously discussed in Chapter 3. A second sample has 15 nm of Fe and an 8 nm Ag capping layer, a third sample has 30 nm of Fe and an 8 nm Ag capping layer. Both in the surface scans and in the height cross sections of Figure 5.2 the atom lithographic lines are clear in the uncapped sample, while in the Ag capped 30 nm Fe sample the structure is somewhat visible, while in the 15 nm Fe sample with Ag capping the lines structures is only faintly visible. It is also visible that the Ag capping layer consists of grains of tens of nm in size, while the Fe layer is much less rough.

For all three samples AFM scans are performed at various points over the substrate to find the local line height of the structures shown in Figure 5.3. Along the nanolines, in y-direction, the line height of the uncapped lines has a Gaussian form, perpendicular to the nanolines, in x-direction, the line height has a peak and broad flanks. The capped samples hardly show the peaked feature in the x-direction. They have a significant decrease in height, up to a factor 4 comparing the capped and uncapped 15 nm thick Fe samples. The 30 nm thick capped sample does show higher line structures than the 15 nm thick capped sample, but the increase is less than a factor two.

We conclude that the Ag layer smoothes the underlying line structure, with the Ag grains partially filling the valleys in between the lines, thereby obscuring the line structure. Intermixing of Fe and Ag is unlikely as they do not form stable alloys. In any modelling of the structures we therefore assume that the Fe structures under the capped layer will have geometries similar to the uncapped layers, although the uncapped layers might affected by oxidation.

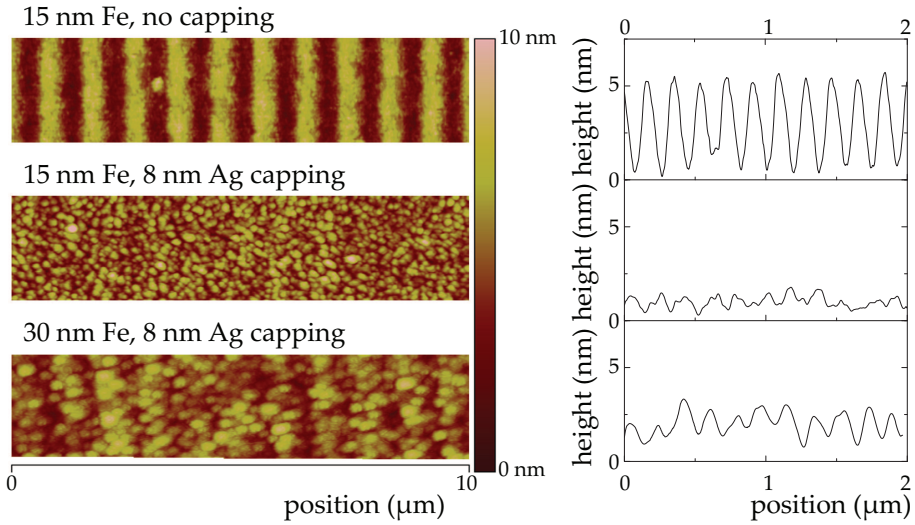

Figure 5.2: *Surface height profiles measured using AFM (left) and cross sections averaged over the direction of line structures (right). Top: Fe layer of average height of 15 nm Fe without capping. Middle: Fe layer of average height of 15 nm and capping of 8 nm of Ag. Bottom: Fe layer of average height of 30 nm and capping of 8 nm Ag.*

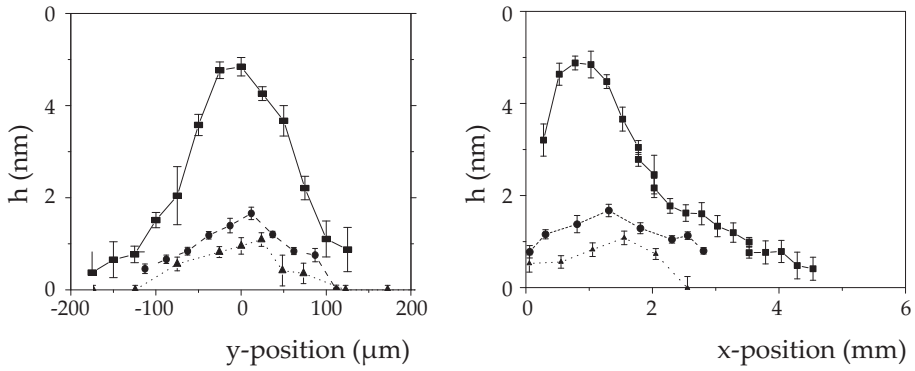

Figure 5.3: *Overview of line heights measured with AFM at different positions on samples with layers of 15 nm Fe, uncapped (squares and solid line), 15 nm Fe capped with 8 nm Ag (triangles and dotted line), 30 nm Fe capped with 8 nm Ag (circles and dashed line). Left: Line heights for different y-positions at one x-position. Right: Maximum line height for each x position.*

5.3 Previous results on atom lithography of Fe.

Experimental results on atom lithography of Fe have been reported by both Myszkiewicz et al. [19] and Smeets [25]. Both have reported on magnetic measurement on their atom lithographic structures, but only Smeets has shown actual data. Myskiewicz only notes that measurements using magnetic force microscopy (MFM) and magneto-optical Kerr effect (MOKE) have been performed and that they revealed a ferromagnetic behaviour with in-plane easy axis irrespective of the presence of nanolines [19]. Smeets reports that focused nanolines are below the resolution of the MFM [25] and with MOKE he finds an easy axis behaviour along the nanolines which is irrespective of the presence of the nanolines [25].

To compare their results with results presented in this chapter, the differences of their samples and experimental procedures are compared to our samples and experimental procedures. It should be noted that this comparison will not be complete, as there is no complete data on their setups and procedures available. There are a few distinct differences of our samples compared to the previous samples. Smeets uses crystalline Si$\langle 100 \rangle$ with native oxide as substrate, which can induce anisotropic growth. We use SiOx to prevent such effects, while Myszkiewicz used glass-ceramic substrates. A second difference is in the background pressure during deposition: Myszkiewicz reports $p \leq 10^{-6}$ mbar, while Smeets reports $p \leq 10^{-7}$ mbar and our setup has $p \leq 5{\cdot}10^{-9}$ mbar. The difference in background pressure might influence the purity of the deposited materials.

The most important difference is the method used to determine the local magnetic properties. Both Smeets and Myszkiewicz used MFM and MOKE measurements. The spatial resolution of the MOKE measurements was limited by the size of the laser beam used, which was typically 100 μm. Different position on the sample are measured in separate measurements. The spatial resolution of an MFM is better than 50 nm, which allows imaging of single nanostructures. However, in MFM the topography of a structure can interfere with the magnetic measurements and Smeets reports that the effects found in the measurements are topographic signatures [25].

In this chapter a optical microscopy technique is used to measure the local magnetisation of the sample, which was not used before for atom lithographic structures. An Evico Magnetics magneto-optical Kerr (MOKE) microscope was used. This is a polarisation sensitive reflection microscope that measures the local Kerr rotation on the sample, which is a measure of the local magnetisation. We applied magnetic fields in plane with the magnetic layer and measured the in-plane magnetisation in the direction of the applied field. The applied field can be ramped while obtaining magnetisation images at discrete intervals. Using a 20x magnification the field of view was 448×341 μm^2 which was imaged on a CCD camera where each pixel corresponds to a 0.67×0.67 μm^2 area. In one field of view both atom lithographically structured and unstructured areas can thus be monitored during the magnetisation process, allowing us to find subtle differences in their magnetic properties.

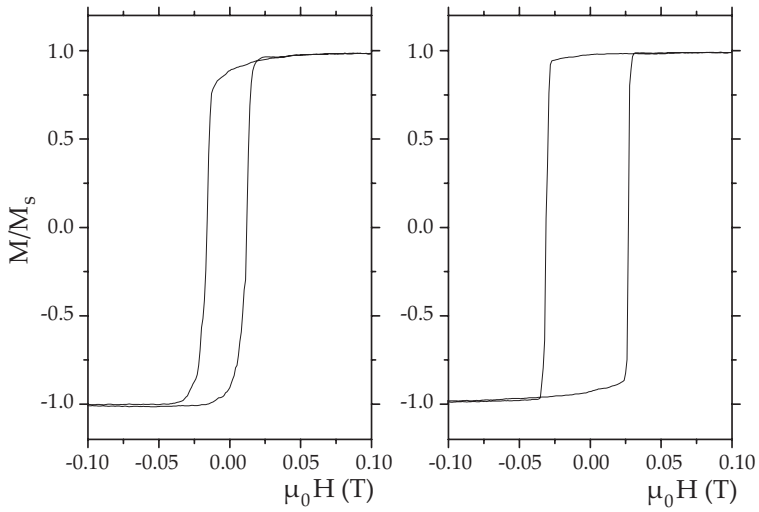

Figure 5.4: *Image from the thesis of Smeets [25]. M/M_s measured by MOKE. Left: Magnetic field parallel to the lines. Right: Magnetic field perpendicular to the lines in the plane of the substrate.*

In Figure 5.4 we show the results Smeets found for hysteresis loops of atom lithographic Fe structures measured with MOKE for an in-plane magnetic field applied parallel and perpendicular to the line direction [25]. The magnetisation is measured parallel to the applied field. The loops clearly show anisotropy, with a higher coercivity and a more squared loop measured perpendicular to the lines. However, this anisotropy was found over the entire sample and could not be linked to the structuring and was therefore considered to be a manifestation of crystalline growth of the Fe on the Si$\langle 100 \rangle$ substrate.

While reviewing other unpublished MOKE measurements performed by Smeets, some effects were found that are linked to the presence of nanolines. In Figure 5.5 the resulting hysteresis loops are shown of MOKE measurements with the magnetic field applied in-plane and parallel to the lines on positions where no structuring is present (dashed lines) and on three positions with atom lithographic structures present (solid lines). On the structured areas the coercivity increases and the curves show more kinks in the curve during switching, as indicated by the arrows. As the MOKE used in these measurements has a spatial resolution limited by the laser waist of 100 μm, any effects of single line structures are averaged out, but the kinks during the switching can be due to groups of lines switching at different applied fields than the background.

Concluding this section we find that previous measurements on atom lithographic Fe structures have not shown clear effects of the structuring on the magnetic properties. Instead a magnetic easy axis was found that was not a consequence of the atom lithographic structures but probably due to growth effects on anisotropic substrates.

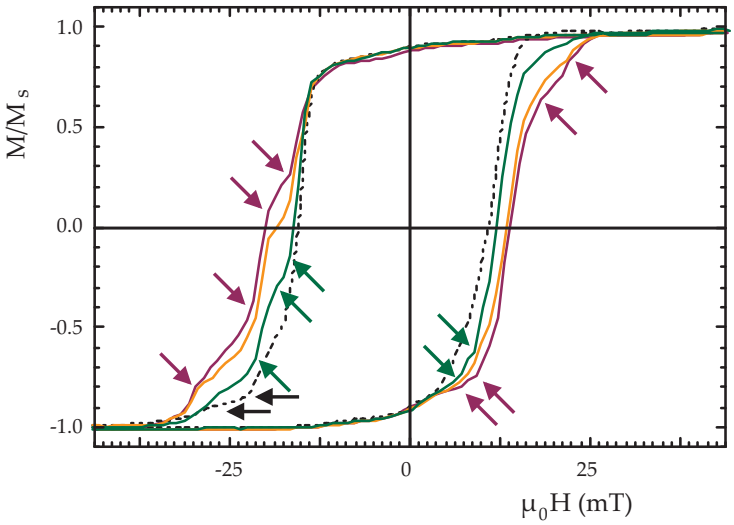

Figure 5.5: Hysteresis loops measured by Smeets with MOKE on an Fe sample with atom lithographic structuring, on three positions with structuring (solid lines) and a position without structuring (dashed line). The applied field is in-plane and parallel to the line structuring.

In retrospect, a review of hysteresis loops recorded by Smeets has given some hints of influence of the structuring on the magnetic properties.

5.4 MOKE microscopy of structured Fe

To find the influence of the atom lithographic structuring on the magnetic properties, we performed MOKE microscopy on 448$\times$341 μm areas where atom lithographic structuring was observed in part of the area with AFM. In this sub-section we discuss the measurements on samples with a Fe layer with an average thickness of 15 nm, similar to those presented in Chapter 3. We applied an external in-plane magnetic field that was ramped from +5 mT to -5 mT and back in 0.2 mT steps, taking a microscopy image at each step. In Figure 5.6 we show the images for the magnetisation in the direction of the applied field, when the angle between the applied magnetic field and the direction of the nanolines is $\theta = 0^\circ$. In the top of Figure 5.6 we indicate the position of the field of view on the sample. In Figure 5.6 in the centre row we show the MOKE microscopy images of the sample at three fields during the field ramp from +5 mT to -5 mT, in the bottom row we show three images during the field ramp from -5 mT to +5 mT. The dark areas indicate magnetisation in one direction, light areas indicate a magnetisation in the other direction. These two series of images show that a vertical band in the centre switches its magnetisation later than

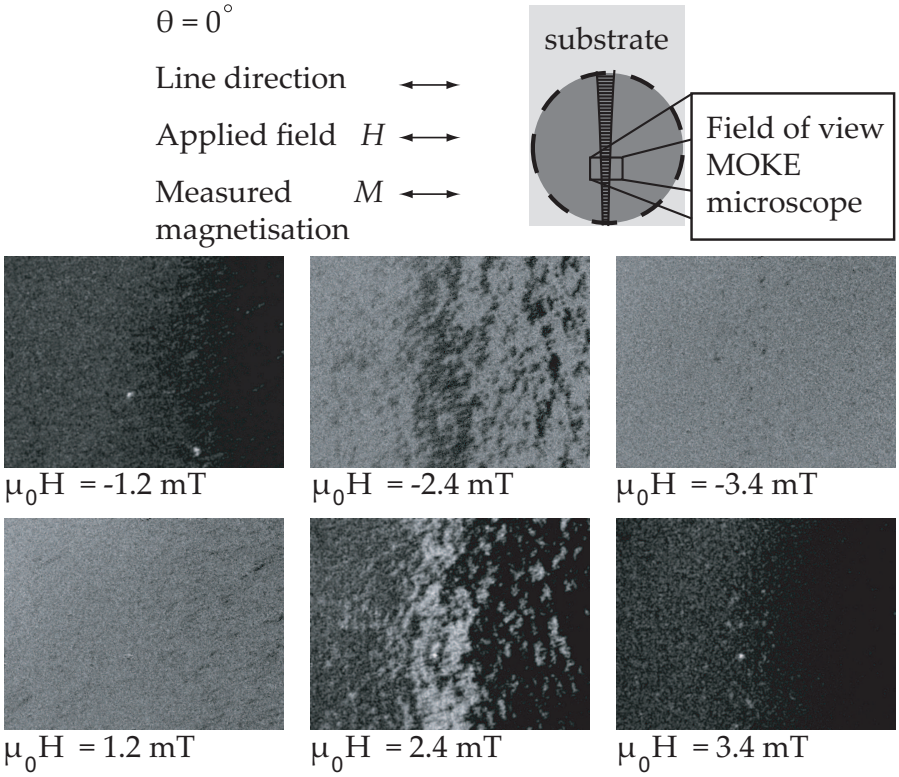

Figure 5.6: *Typical MOKE microscopy images of the switching behaviour of a 15 nm thick Fe sample. The inset at the top shows the field of view of each image of 448×341 μm , with the structured area in the centre. The line direction, the applied field and the measured magnetisation are in horizontal direction. The top row of MOKE images are taken while the applied field is ramped from +5 mT to -5 mT, at an applied field of -1.2 mT, -2.4 mT and -3.4 mT. The bottom row of MOKE images are taken while the applied field is ramped from -5 mT to +5 mT, at an applied field of +1.2 mT, +2.4 mT and +3.4 mT.*

the surrounding unstructured area. The position of this vertical band corresponds to the area where nanostructures were observed with AFM.

The sequence of images taken during the ramp of the applied field, shows when each point within the field of view switches and thus allows to determine the local value of the coercivity. To this end a Mathematica programme was created that calculates the local coercivity on a grid of 21×16 sub-images over the entire field of view, obtaining a spatial resolution of 21 μm in both horizontal and vertical direction.

In these calculations the average pixel value, which is proportional to the magnetisation, is calculated for each sub-image at each applied field, creating a hysteresis curve, which is normalized in two steps. First, the magnetisation averaged over all applied fields is subtracted as an offset value. Secondly, we assume that for applied

fields larger than $|\mu_0 H| > 4$ mT, the magnetisation is saturated. The average value of the magnetisation for applied fields larger than $|\mu_0 H| > 4$ mT is thus M_{sat}, which is used to normalise the hysteresis curves. From each hysteresis curve the coercivity H_C is extracted as the average of the absolute values of the applied field at the two zero crossings of the magnetisation at positive and negative applied field. If more than two zero crossings are found, an error is returned.

In Figure 5.7 the results of the calculations of the local coercivity are presented. In Figure 5.7A one MOKE image at $\mu_0 H =$ -2.4 mT is shown as a reference, revealing the vertical stripe where atom lithographic structures are present. In Figure 5.7B we present the coercivity map of the same position, again revealing a stripe where the coercivity is increased from the unstructured value of about $\mu_0 H_{C,\text{unstructured}} =$ 1.9$\pm$0.1 mT up to $\mu_0 H_{C,\text{structured}} =$ 2.4 mT. In Figure 5.7C we show the cross section of line heights of the atom lithographic structures at this position, directly linking the position of the structures with the coercivity increase.

As the atom lithographic structures were observed over an area of a few mm long, MOKE measurements were performed at neighboring positions on the sample over a length of more than 4 mm. In Figure 5.7D we show the combined coercivity map over the entire structured area, revealing that the band of coercivity increase stretches over a several mm. As a reference Figure 5.7E shows the cross section of line heights, already shown in Figure 5.3, along the length of the coercivity map. From all these results it is clear that the nanostructured area has an increased coercivity.

To investigate the anisotropy of the line structures, the coercivity as a function of the angle θ of the applied field to the nanoline direction, was investigated at the position where the highest line structures were measured. All measurements showed a very similar behaviour: the structured area always has a larger coercivity than the unstructured area. Coercivity maps such as shown in Figure 5.7B have been created of each measurement. In each coercivity map the structured area is visually identified as a stripe of increased coercivity. The mapped coercivity values over the centre 42 μm of this stripe are averaged and taken as the coercivity of the structured area. The coercivity of the unstructured area is defined as the average coercivity of all positions more than 126 μm away from the centre of this stripe. To create complete polar plots, separate values for the coercivity at positive and negative applied fields are calculated.

The angular plots for the unstructured and the structured area in Figure 5.8 show no clear anisotropy. In the unstructured area a small biaxial anisotropy is observed with easy axes along the $\theta = 60^\circ$/ $\theta = 240^\circ$ and $\theta = 150^\circ$/ $\theta = 330^\circ$ axes. This could be due to crystalline growth, as Fe$\langle 100 \rangle$ has a biaxial anisotropy. In Figure 5.8 the hysteresis curves for the unstructured and structured areas are shown for the applied field parallel and perpendicular to the line direction. The hysteresis curves are all very similar, indicating no anisotropy in the structured area, in contrast with the results of Smeets.

Both Figure 5.7 and Figure 5.8 show that the structuring of the Fe layer of 15 nm thick increases the local coercivity, but does not give rise to any anisotropies. For

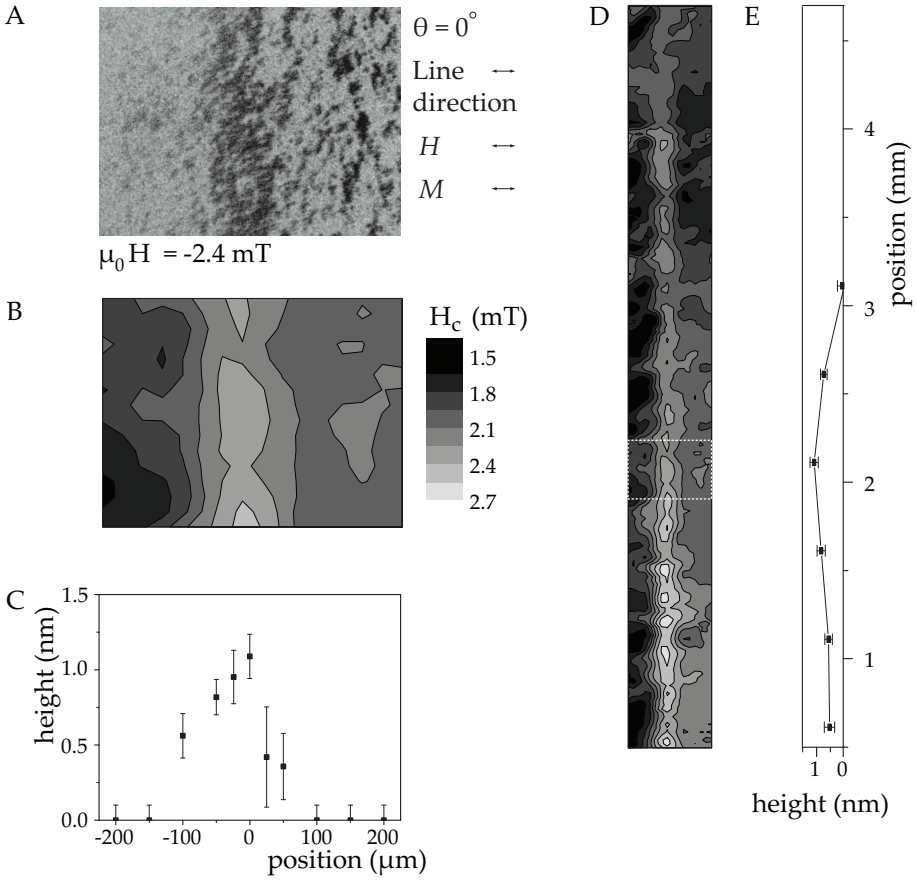

Figure 5.7: *Results of coercivity mapping of the MOKE microscopy measurement of Figure 5.6. A) single MOKE microscope view at $\mu_0 H$ = -2.4 mT. B) Corresponding coercivity map. C) horizontal cross section of line height measured with AFM over area shown in A. D) Stitched coercivity maps over the entire length of the atom lithographic structured area. E) vertical cross section of maximal line height measured with AFM over area shown in D.*

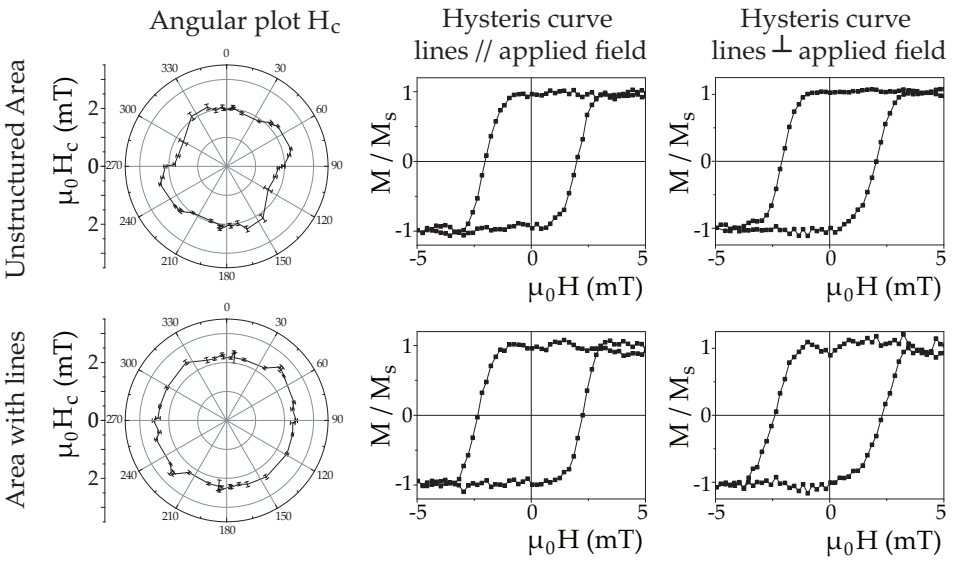

Figure 5.8: *Results of MOKE microscopy measurements of atom lithographic line structures at an angle θ to the applied field. Top: results for unstructured background; bottom: results for atom lithographic structures. Left: Polar plot of the coercivity, at 0° the applied field and measured magnetisation is along the lines direction*

the sample whose results are shown in this paragraph the values for the coercivity range over 1.6 mT $< \mu_0 H_{C,\text{unstructure}} <$ 2.4 mT while for the structured area 2.2 mT $< \mu_0 H_{C,\text{structure}} <$ 2.6 mT. The other 15 nm thick sample showed similar results: 1.2 mT $< \mu_0 H_{C,\text{unstructured}} <$ 1.4 mT and 1.7 mT $< \mu_0 H_{C,\text{structure}} <$ 1.9 mT. The increase in the coercivity due to structuring on a sample is thus comparable to the variation in the unstructured coercivity values between different samples. Only because MOKE microscopy allows for the direct comparison of magnetisation of structured and unstructured areas have we been able to find these subtle effects.

The results of Smeets from MOKE measurements on single positions with about 100 μm spatial resolution we presented in Figure 5.5 hinted on effects of nanolines. On structured areas a minor increase in coercivity was observed and hysteresis curves showed more kinks, as structured areas switched at higher fields than unstructured areas. This is indeed in line with the results of the MOKE microscopy. In Section 5.6 the increase in coercivity due to the structuring is discussed, after the properties of thicker structured samples are presented in the following paragraph.

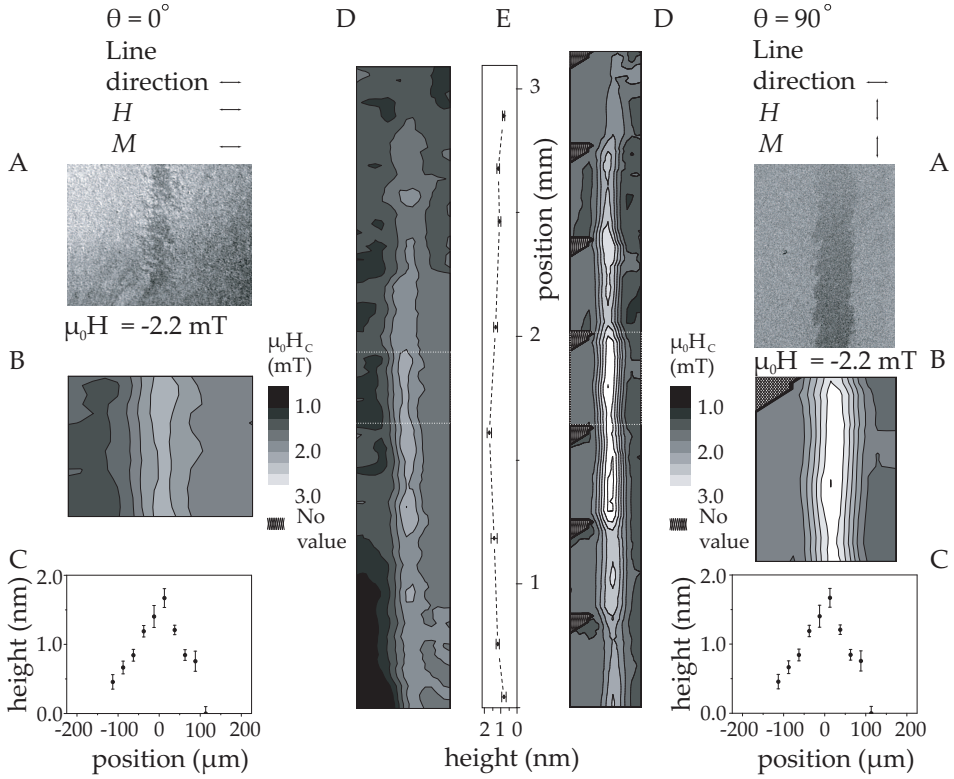

Figure 5.9: *Coercivity mapping of atom lithographic Fe sample of 30 nm thick for $\theta = 0°$ (left) and $\theta = 90°$ (right). A) Single MOKE microscope view at $\mu_0 H$ = -2.2 mT. B) Corresponding coercivity map. C) Horizontal cross section of line height measured with AFM over area shown in A. D) Stitched coercivity maps over the entire length of the structured area. E) vertical cross section of maximal line height measured with AFM over area shown in D.*

5.5 Effects in thicker structured Fe.

In the previous sub-section the magnetic properties of atom lithographic structured Fe with an average thickness of 15 nm were presented. The structuring was found to increase the coercivity of the Fe layer, but no anisotropy was found in the structured areas. In this section the properties of layers of 30 nm average thickness are presented, which are created by doubling the total deposition time to 4 hours. Thicker samples are not practically achievable with the current setup.

Coercivity maps have been created in the same way as described in the previous sub-section for a 30 nm sample for $\theta = 0°$ and $\theta = 90°$, these are shown in Figure 5.9. In Figure 5.9a for both field settings a single MOKE image is shown for $\mu_0 H$ = -2.4 mT. The corresponding coercivity map for that position is given (B), together with a cross section of the height of the nanolines in that image measured by AFM (C).

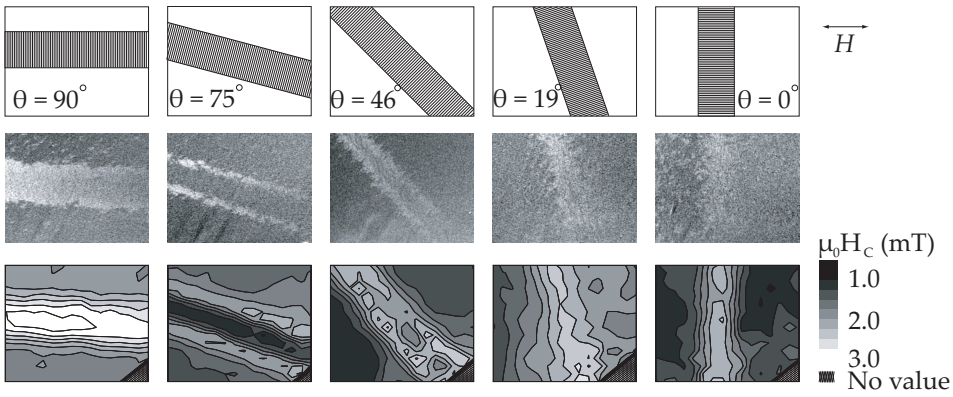

Figure 5.10: *Results of MOKE measurements on a 30nm high Fe layer with atom lithographic line structuring with the applied field at various angles θ to the line direction. Top row: schematic positions of the atom lithographic structuring. Middle row: representative MOKE view at an applied field of $\mu_0 H$ = -2 mT. Bottom row: coercivity maps.*

The coercivity mapping is also performed over various positions which form a stitched coercivity map (D) which can be compared to a cross section of the maximum line height measured by AFM (E).

For $\theta = 0°$, on the left of Figure 5.9, the MOKE image shows the patterned area as a grainy and not well defined vertical stripe. In the coercivity maps this stripe is also visible, the coercivity of the patterned area $H_{C,\text{structured}} < 2.2$ mT is increased compared to the unstructured area 0.8 mT $< H_{C,\text{unstructured}} <$ 1.7 mT. For $\theta = 90°$, shown on the right of Figure 5.9, the images show significantly more contrast. The patterned area is a clear stripe in the MOKE image and this stripe is clearly visible in the coercivity maps. The coercivity of the patterned area for $\theta = 90°$ is $H_{C,\text{structured}} \leq$ 3.0 mT, significantly larger than in the unstructured area, 1.2 mT $< H_{C,\text{unstructured}} <$ 1.7 mT.

In contrast to the results for the 15 nm structured sample, the results in Figure 5.9 indicate that there is anisotropy due to the line patterning. We have therefore performed MOKE microscopy measurements at various angles θ on the position where we observed the highest lines with AFM. In Figure 5.10 microscopy images and coercivity maps for five values of θ are presented, schematically giving the position and orientation of the atom lithographic structuring on the top row, showing on the middle row one representative MOKE image for an applied field of about $\mu_0 H$ = -2 mT and presenting the coercivity maps on the bottom row.

The most striking result is obtained for $\theta = 75°$, where we see in the MOKE image that the unstructured area and the centre of the structured area are switched, while the edge of the structured area is not yet switched. In the corresponding coercivity map, we find that the centre of the structured area has the lowest coercivity, while the edge of the structured area has a higher coercivity than both the unstructured area

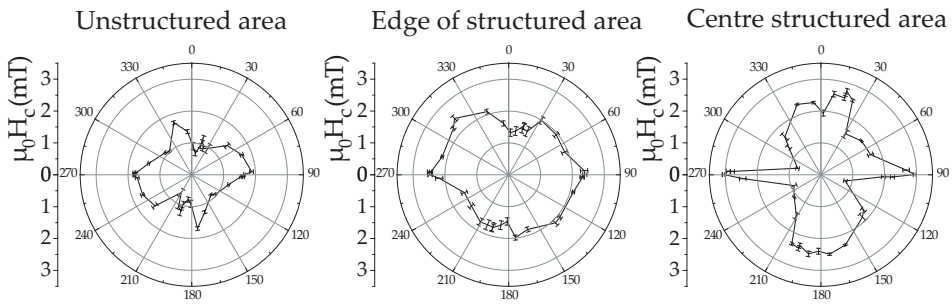

Figure 5.11: *Polar coercivity plot of a 30nm thick Fe layer atom lithographically structured with lines at an angle θ to the applied field, for the unstructured background (left), the edge of the structured area (middle) and the centre of the structured area (right).*

and the centre of the structured area. This odd behaviour is somewhat reproduced for $\theta = 46^\circ$, where the centre of the structured area has a coercivity higher than the unstructured area, but lower than the edge of the structured area.

To quantitatively show this behaviour we have measured the coercivity of the unstructured area, the edge of the structured area and the centre of the structured area for a large number of angles θ. In each coercivity map the structured area is visually identified as a stripe or a set of stripes. The centre of the structured area is defined as the centre 42 μm, the edges are 21 μm wide bands 52.5 μm away from the centre, the background coercivity is defined as the average coercivity of all positions more than 105 μm away from the centre of the structured area. Although this method is both cumbersome and introduces some uncertainty as it involves visual analysis, the results are clear. We show the resulting angular plots of the coercivity in Figure 5.11.

In Figure 5.11 we find limited angular effects for the unstructured area and the edge of the structured area, but a pronounced anisotropy is present for the centre of the structured area. The unstructured area shows a biaxial anisotropy in the background with easy axes along the $\theta = 75^\circ$ / $\theta = 225^\circ$ and $\theta = 165^\circ$ / $\theta = 355^\circ$ axes. This could be due to crystalline growth of Fe$\langle 100 \rangle$ which is biaxial anisotropic. The edge of the structured area shows no clear anisotropy.

The centre of the structured area, where the highest lines are present, shows one maximum in the coercivity for the field applied parallel to the line direction, $\theta = 0^\circ$ / $\theta = 180^\circ$ with values of $\mu_0 H_C = 2.2 \pm 0.2$ mT. The coercivity decreases for increasing angles θ, but a sharp increase in coercivity is observed for angles less than $20 \pm 5^\circ$ off the axis perpendicular to the line direction, $\theta = 90^\circ$/ $\theta = 270^\circ$, where the global maximum in coercivity is observed with values of $\mu_0 H_C = 3.0 \pm 0.1$ mT.

Comparing the plots of Figure 5.11 we find that the centre of the structured area has a lower coercivity than the edge of the structured area if θ deviates 15° to 45° from the $\theta = 0^\circ$/ $\theta = 180^\circ$ axis. This corresponds to the behaviour observed in Figure

5.10, where the centre of the structured area and the unstructured area switched before the edge of the structured area. We do note that these results are obtained on the area where the highest line structures were measured with AFM. On points of the stripe shown in Figure 5.9, where the line structures are lower, the behaviour was similar to the results of the 15 nm thick sample: no clear anisotropy was observed, only an increase in coercivity in the structured areas. This confirms that the observed anisotropy is linked to the height of the lines.

We have thus observed anisotropic behaviour in 30 nm thick Fe layers structured with atom lithography, which is dependent on the height of the line structures. For the highest line structures this anisotropy consists of an increased coercivity for $\theta = 0^\circ$. The coercivity decreases with increasing angle θ , until the coercivity increases sharply around $\theta = 90^\circ$. This behaviour has been observed in two samples, but it should be noted that a third sample has been left out of this analysis that did not show this behaviour. This sample showed visual signs of oxidation on the sample. The background coercivity was 50 mT $< H_{C,\text{unstructured}} <$ 60 mT, while for the other 30 nm samples 0.7 mT $< H_{C,\text{unstructured}} <$ 1.8 mT and for the 15 nm samples 1.6 mT $< H_{C,\text{unstructured}} <$ 2.4 mT.

5.6 Understanding a biaxial anisotropy in a uniaxial line structure.

In the previous sub-sections the magnetic properties of layers structured with atom lithography showed no anisotropy for 15 nm thick layers, while 30 nm thick layers showed a biaxial anisotropy, with a higher coercivity both at $\theta = 0^\circ$ and at $\theta = 90^\circ$. This is not expected considering the uniaxial geometry of the line structures. In the previous Chapter, ferromagnetic line structures were investigated that were created with shadow deposition in the same setup as the atom lithographic structures. For these line structures indeed a single magnetic easy axis was observed along the direction of the lines, at $\theta = 0^\circ$.

In this sub-section results are shown of micromagnetic modelling of line structures and an overview is presented of results reported in literature for various line structures. These results mostly confirm the presence of a magnetic easy axis along the direction of line structures. At the end of this sub-section alternative explanations are provided to explain for the observed lack of anisotropy in thin atom lithographic samples and the biaxial anisotropy in thick samples.

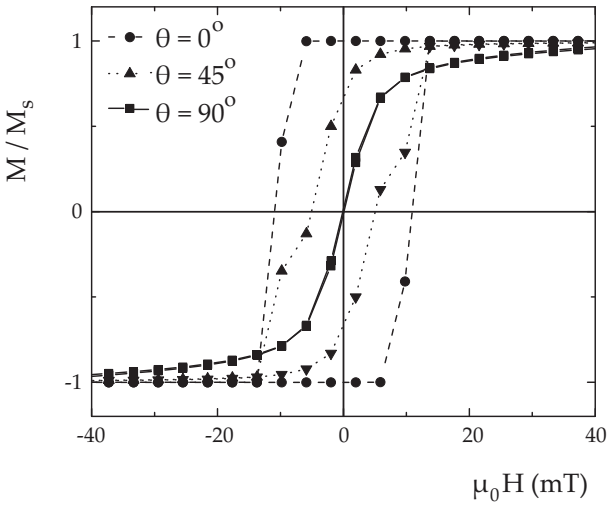

Figure 5.12: Hysteresis loops simulated with the LLG micromagnetic simulator [69] for atom lithographic structures with applied fields at $\theta = 0°$, $\theta = 45°$, or $\theta = 90°$.

5.6.1 Micromagnetic Modelling

The magnetic properties of the atom lithographic structures have been modelled using the LLG micromagnetic simulator [69], which is a three dimensional simulation programme for micromagnetic structures. However, as our samples stretch over length scales of mm, it is not possible to model an entire sample. To prevent unrealistic calculation times, periodic boundary conditions were applied to a 128×128×15 nm^3 structure, consisting of single calculation cells of 4×4×1 nm^3. The Fe structures are modelled as a 10 nm thick background layer with a 5 nm high corrugation in the form of a squared sine of period of 128 nm, which is for practical reason chosen to be slightly smaller than the real period of 186 nm. The properties for Fe as input are the saturation magnetisation $M_s = 1714$ kA/m and the exchange constant $A = 21.3$ pJ/m. To this model system magnetic fields were applied from +1 T to -1 T, in steps of 4 mT. To reduce calculation time, the reverse magnetisation curve is not calculated but taken to be point symmetric. The fields and resulting magnetisation were calculated either along the direction of the line at $\theta = 0°$, or at $\theta = 45°$, or at $\theta = 90°$. The results are shown in Figure 5.12.

The hysteresis curves in Figure 5.12 indicate an easy axis along the direction of the lines. This is in agreement with the results of line structures created with shadow deposition in Chapter 4, but it is not in agreement with the results found in the 15 nm thick atom lithographic samples. The 30 nm thick structured samples do show an increased coercivity at $\theta = 0°$, which decreases with increasing angle θ, but the experimental results show a very sharp increase in coercivity around $\theta = 90°$, where modelling results indicate a hard axis with zero coercivity at $\theta = 90°$.

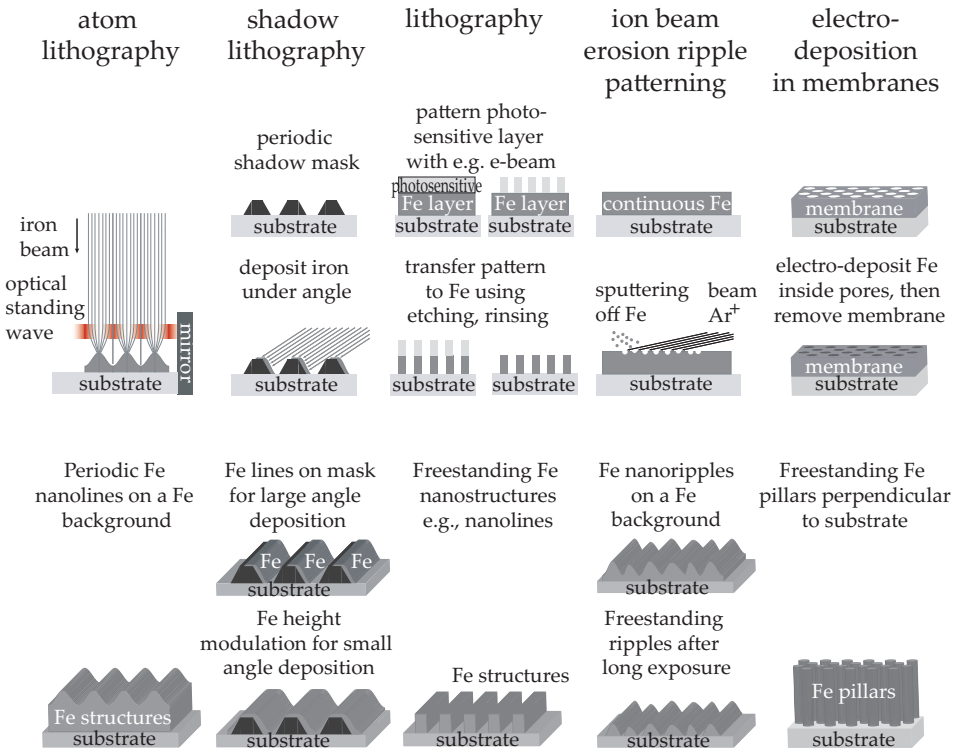

Figure 5.13: *Structuring techniques to create line structures (top) and resulting structures (bottom).*

5.6.2 Magnetic nanoline arrays in literature.

The magnetic properties of micro- and nanowires and as well as arrays of these structures have received much interest over recent years. Due to their reduced dimensionality, the magnetic properties of these structures differ from their bulk constituent materials, revealing new aspects of magnetism. In Figure 5.13 we show five different options to create nanoline or nanowire arrays: atom lithography, three other techniques to create in-plane nanoline arrays and one technique to create out-of plane nanowire arrays.

Atom lithography On the left of Figure 5.13 the concept of atom lithography is shown. With this technique structuring is created during deposition using intense standing wave laser fields just above the surface of the substrate. The resulting structures are nanolines on top of a background layer, for uncapped Fe 5 nm high structures are created on a layer of 15 nm average thickness. The structures are defined by the standing wave laser field and thus straight and perfectly periodic with a period of 186 nm. The nanolines are about 200 μm long and are formed over an area of a few mm.

Shadow lithography In the second column of Figure 5.13 the concept of shadow lithography is shown. To create nanolines with this technique a non-planar substrate is required that has facets, step-edges or other periodic corrugations that work as a shadow mask. If a material is evaporated onto the substrate at large angles, the structure of the shadow mask is recreated in the deposited material. Freestanding Fe lines have been created with various shadow masks such as: an array of atom lithographic Cr lines [67], faceted $\alpha - Al_2O_3$ [70], faceted NaCl$\langle 110 \rangle$ [71] or vicinal Si$\langle 111 \rangle$ surfaces [72]. These freestanding structures had widths in the range from 25 to 400 nm, heights in the order of 3 to 30 nm, periods in the range of 75 nm to 3.2 μm, and lengths from several μm up to 0.15 mm. These ranges include the dimensions of atom lithographic structures of this chapter. The structures are reported to be polycrystalline, grainy structures without crystalline anisotropy. The literature on these freestanding structures shows a clear shape anisotropy with an in-plane easy axis along the direction of the lines. This in-plane easy axis has also been observed in chapter 4, where we used a polymer grating as a shadow mask, to create continuous Fe_xNi_{1-x} layers where the height and composition is changed along the lines due to shadow effects.

Optical and e-beam lithography The basis of lithography is using light or electron-beams to pattern an image in a photosensitive layer and to transfer this pattern into a second layer. This image transfer can be performed in various ways, one of which is shown in the third column of Figure 5.13. A photosensitive layer is deposited on top of a second layer of magnetic material. An image is created in the photosensitive layer and subsequently transferred to the magnetic layer by etching away the unexposed parts. Finally the photosensitive layer is removed. Lithography on Fe nanolines, wires or stripes has been reported by various groups [73, 74, 75], creating arrays of freestanding structures with periods of 300 to 800 nm, widths of 150 to 500 nm, heights of 13 to 25 nm and lengths of 0.3 mm or larger. The deposited Fe layers were either polycrystalline or mono-crystalline Fe, so that magneto-crystalline anisotropies can be significant in the reported results. All three groups report that the shape anisotropy of the lines induces an in-plane easy axis along the direction of the lines, that is stronger than the magneto-crystalline anisotropy of the Fe.

Ripple patterning by ion beam erosion Ion beam sputtering can be used to induce nanoscale surface ripples. This is schematically shown in the fourth column of Figure 5.13. When an ion beam is positioned at an angle to the surface, anisotropic sputtering at perturbations of the surface combined with surface diffusion create ripple structures perpendicular to the projection of the ion beam direction on the surface [76]. These ripples are not perfectly straight, nor perfectly periodic, but they are in one distinct aspect very similar to our atom lithographic structures: they consist of line structures on a background of the same material. Ripple patterning of thin Fe layers has been performed by various groups [77, 78, 79], creating structures of up to 4 nm high, on layers of up to 20 nm, with periods of 35 to 100 nm. In all these structures a competition is found between the crystallographic anisotropy, which is biaxial in all references, and an induced uniaxial behaviour from the nanolines. Buettner et al. [79] report on ripple structures of 4 nm height on a 13 nm thick mono-crystalline Fe$\langle 001 \rangle$ background, which are comparable in size to our struc-

tures and find for these settings both crystalline anisotropy and a uniaxial anisotropy along the ripple direction.

Electrodeposited nanolines in membranes The most often studied system for the creation of nanowire arrays, is based on the electrodeposition of nanowires in membranes, schematically shown on the right of Figure 5.13. This technique allows for the fabrication of regular arrays of nanowires perpendicular to a substrate, either still in the membrane material or freestanding after removal of the membrane. Although the geometry of this system is very different compared to the atom lithographic nanolines, the large body of literature on this type of system make them interesting for comparison. For this type of structure, effects of magneto-static interactions between wires have been investigated, which was not taken into account for the systems previously mentioned in this section. The magneto-static interactions of magnetised wires can be easily understood in terms a dipolar coupling: if the aligned wires are all magnetised along the wire, dipolar coupling favors anti-parallel alignment of the wires to each other. This dipolar coupling competes with the shape anisotropy, which favors alignment parallel to the wires. This competition leads to a change in anisotropy, with an easy axis along the wires for short wires at long distances and a easy plane perpendicular to the wires for closely packed, long wires. This cross-over behaviour has been observed in arrays of nanowires of various materials such as Co [80], $Ni_{68}Fe_{32}$ [81], Ni, NiFe and CoNiFe [82]. However, it should be noted that if both effects are of similar size, the angular coercivity shows an M-shaped form, with minima for $\theta = 0^\circ$ and $\theta = 90^\circ$ [82]. This is exactly opposite to the behaviour observed in our atom lithographic structures.

Based on the literature presented in this sub-section, the observed anisotropies in the atom lithographic structures cannot be explained. In the literature a magnetic easy axis for $\theta = 0^\circ$ has been observed in various types of nanowire or nanoline arrays. Dipolar interactions can induce an easy plane perpendicular to the wire direction, but then there is no easy axis along the wire direction. A magneto-crystalline anisotropy can induce a biaxial anisotropy as was observed in the unstructured parts of the samples, but it is not likely the cause of the anisotropy of the lines. Anisotropy of the line structured area due to magneto-crystalline effects would most likely also be present in the unstructured Fe layer.

5.6.3 Domain wall types and switching behaviour.

In the literature discussed in the previous section, the magnetisation reversal of a nanoline, or a set of lines was mostly found to have a uniaxial anisotropy. This behaviour was already explained in Chapter 1 when line structures were viewed in the framework of a Stoner-Wohlfahrt system, where the magnetisation coherently rotates from one alignment to the other. Within this framework, the behaviour observed in our atom lithographic structures is not explained. We therefore investigate possible effects of domain walls and domain switching behaviour.

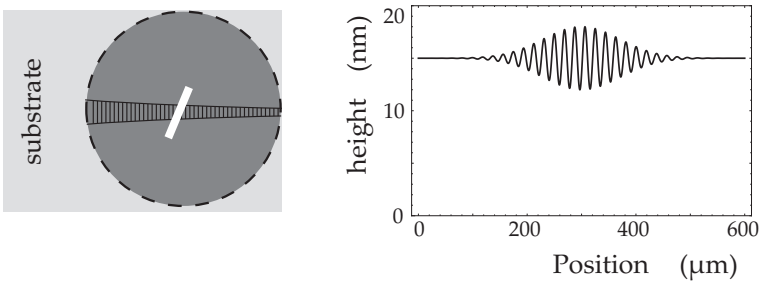

Figure 5.14: *Left: Schematic overview of a sample with atom lithographic structuring. Right: Schematic height cross-section over the white bar in the left image, showing the background height and the varying structure height.*

We once again summarize the observed behaviour of our atom lithographic nanostructures. These structures consist of a Fe background layer, with a modulation on top. A schematic is shown in Figure 5.14. The average height of background and line structure is constant over the sample, so where the lines are higher, the background is less high. We observed switching in thin (15nm) and thick (30 nm) samples. The structured area of the thin samples showed an isotropic increase of the coercivity compared to the background. In the 30 nm thick sample a more complex behaviour was observed. The lower line structures, which form the edge of the structured area showed an isotropic increase of the coercivity compares to the background similar to the behaviour of the 15 nm thin samples. The highest line structures, in the centre of the structured area, showed an increased coercivity for $\theta = 0^\circ$, higher than the coercivity of both the unstructured area and low line structures. The coercivity of the highest line structures decreases with increasing θ, indicating an easy axis along the direction of the lines. The coercivity decreases to values even lower than the coercivity of both the unstructured area and the low line structures. However, at angles near $\theta = 90^\circ$ the coercivity of the highest lines increases sharply and at $\theta = 90^\circ$ the highest coercivity is observed.

To understand the isotropic increase in coercivity of the 15 nm samples, we disregard the anisotropy of the line structures and consider these as isotropic roughness. Although this approach is crude, there are reasons why this might be valid. The limited contrast of the lines will give only a limited anisotropy, while the very grainy structure of the Ag capping observed in Figure 5.2 might further decrease anisotropic effects of the underlying Fe lines. Finally it was found in Chapter 4 that the deposited layers of Fe are most likely polycrystalline and separate crystalline grains might further limit anisotropic effects. If the line structuring is only considered as an isotropic roughness, literature provides various effects that could change the coercivity.

Surface roughness can enhance both domain nucleation and domain pinning. However, the resulting coercivity is usually found to increase with increasing roughness for e.g., Fe on Ag substrates [83], or $Ni_{80}Fe_{20}$ on Si$\langle 100 \rangle$ [84]. In contrast, Zhao et

Figure 5.15: *Schematic representation of Bloch domain wall (left) and Néel domain wall (right) in thin films.*

al. find that increased roughness can both increase coercivity in thin layers and decrease coercivity in thick layers. They explain this behaviour by the fact that domain walls in thin and thick layers differ and each has a different interaction with surface roughness [85]. For the 15 nm and the 30 nm samples, it is therefore not a priori clear if increased roughness will increase or decrease the coercivity.

The formation of domain walls in thin film structures is known to be dependent on the height of the structures [27]. Two types of domain walls are well known and easily described: Bloch walls and Néel walls, shown schematically in the top of Figure 5.15. The Bloch wall has no bulk magneto-static energy as $\nabla \cdot \overrightarrow{M} = 0$, except at the surface, while the Néel wall has a magneto-static energy contribution in the bulk but no stray fields at the surface. The competition of a volume and surface energy contribution, makes the Néel wall energetically favorable for very thin films, while the Bloch wall is more favorable for thicker films. It should be noted that especially at the transition regime, other domain walls can be stable such as the asymmetric Bloch wall (C-type), which consists of a Néel wall on the surface and a Bloch type interior [86].

In Fe the transition from Bloch to Néel wall has been observed around 30 to 60 nm film thickness [87]. Around 30 to 50 nm thickness of Fe films an increase in coercivity has been observed, which is also attributed to a change in domain wall type [88]. Although the transition of Bloch to Néel wall is not only dependent on the height, but also on e.g., the quality of the deposited film, it is clear that the 30 nm thick film are near the regime of the transition.

Although the type of domain wall in our samples has not been observed, the switching behaviour for $\theta = 75^{\circ}$ as shown in Figure 5.10 does indicate that two different types of switching are present. A low coercivity is observed for the highest lines and for the unstructured layer, while the coercivity remains high at intermediate line heights. Therefore it is likely that two different types of switching are present, leading to the observed behaviour. As the unstructured area and the edge of the line structures of the thin and thick sample behave similarly for all angles, it is likely that the switching in these areas is of Néel type, which is energetically favorable for thinner layers. The switching at the highest line structures might then be via a Bloch like domain wall, which is favorable for thicker layers. Here we recall that according to Zhao et al. [85], the coercivity of Bloch switching decreases with increased roughness, while the coercivity increases with roughness for Néel switching. This supports the view that for the 30 nm layers, whose height is near the transition of Néel to Bloch switching, the more corrugated areas show Bloch switching and the

least corrugated areas Néel switching. In the 15 nm layers and the 30 layers at positions with low corrugations, the isotropic increase of the coercivity with increasing line height can thus be explained by an increase in coercivity in a Néel like switching due to an increased roughness.

To support these claims, additional micromagnetic simulations were performed. To test the effect of sample thickness on the domain wall formation, thin Fe samples have been modelled using the LLG micromagnetic simulator [69]. In the top inset of Figure 5.16 the schematic is shown of a thin layer that is divided in two equal parts one with magnetisation in +y direction, the other with magnetisation in -y direction. Three flat layers were modelled with this starting magnetisation. The model structures had dimensions of 512 nm in x-direction, 128 nm in y-direction, but periodically propagated in y direction and heights of respectively 26 nm, 36 nm and 108 nm. The model structure is divided into $4\times4\times1$ nm^3 cells. To find the typical shape of the domain wall, the magnetisation was relaxed to find the minimal energy configuration under no applied field. The results are presented in the top of Figure 5.16. Three sets of images are shown, representing the magnetisation in x, y and z. In the M_y images, the clear black and white contrast indicate the two domains along +y and -y directions for all heights. The grey areas for M_x and M_z at the outer edges indicate zero magnetisation. The M_x and M_z images do show contrast at the domain wall. However, it is clear that the domains are not pure Néel walls, which would rotate only via the M_x direction, nor pure Bloch walls, which would rotate only via the M_z direction. We do find that the M_z components are more pronounced for thicker walls, while M_x components are present for all heights. This confirms the notion from literature that thicker layers induce more Bloch-like walls.

A period line structure is a second model structure, modelled as a 24 nm background layer of Fe with a 12 nm corrugation in the form of a squared sine of period of 128 nm, so that the average height is 30 nm as in our samples. The structure is 512 nm long, thus containing four periods. It has periodic boundary conditions in y-direction, but not in x-direction. The magnetisation is set along -y for the left and along +y for the right of the structure as indicated in the inset in the lower half of Figure 5.16. The magnetisation was relaxed to find the minimal energy configuration under no applied field, as indicated in the $\mu_0 H = 0$ mT image. After the minimal energy configuration of the domain wall is found, an external field is applied along the +y direction. In Figure 5.16 the magnetisations at increasing applied fields show that the domain wall is pinned at the valley of the line structures for fields from $\mu_0 H = 2$ mT to $\mu_0 H = 54$ mT, only releasing at $\mu_0 H = 56$ mT.

The pinning of the domain wall in Figure 5.16 indicates that interactions of the domain wall with the line structure can increase the coercivity. However, the modelling in the lower half of Figure 5.16 is for the field and magnetisation in the $\theta = 0^\circ$ configuration. The anisotropic behaviour of the highest line structures in the thicker samples is hereby not yet explained. The high coercivity for applied fields along the line direction, which decreases as the angle of the field with respect to the line structure increases, indicates an easy axis, in accordance with literature expectations and with the modelling shown in section 5.6.1. The very sharp increase of the

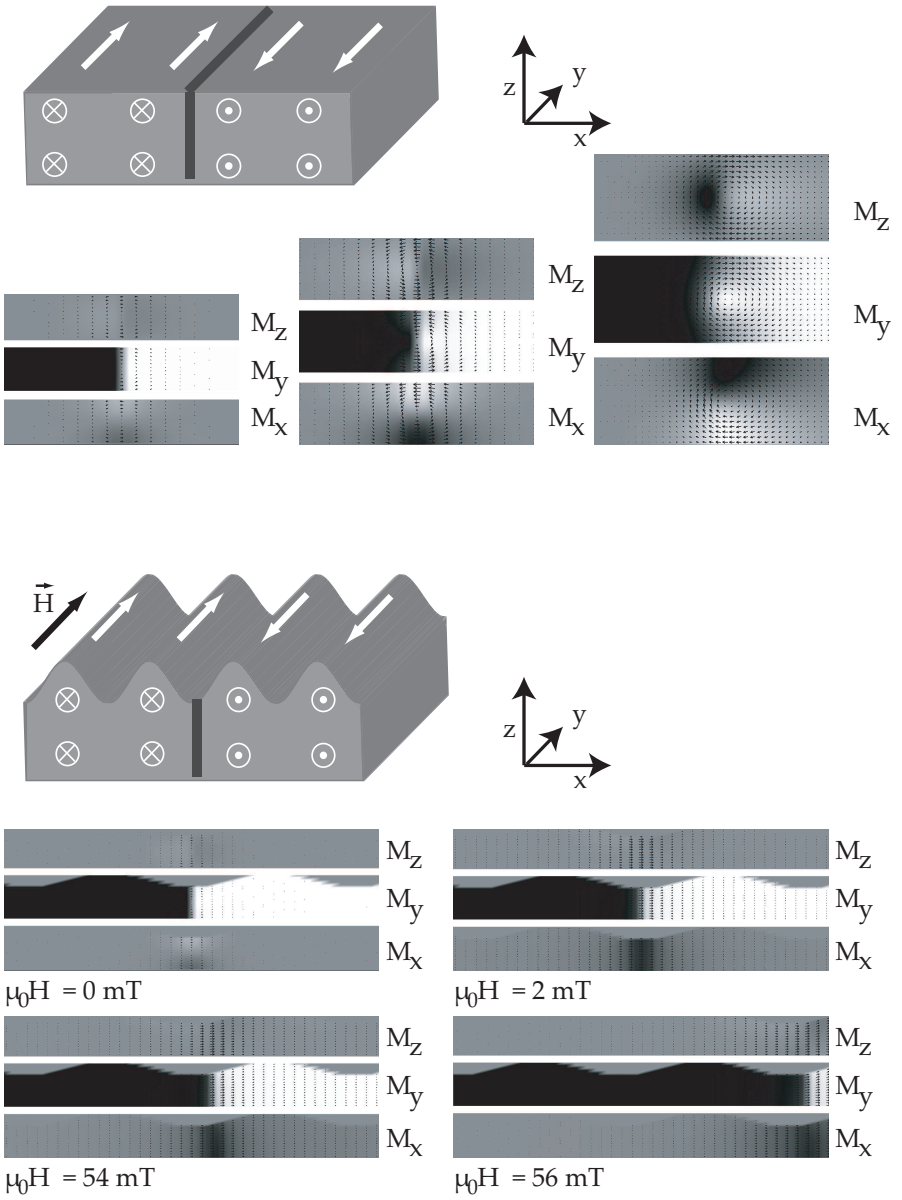

Figure 5.16: *Modelling domain walls in Fe structures using the LLG micromagnetic simulator. Top: magnetisation of thin Fe layers of thickness 26 nm (left), 36 nm (middle) and 108 nm (top) with an introduced domain wall at no applied field. Bottom: propagation of domain walls in a periodically modulated structures of Fe of 36 nm total height under applied field ranging from* $\mu_0 H = 0$ *mT to* $\mu_0 H = 56$ *mT.*

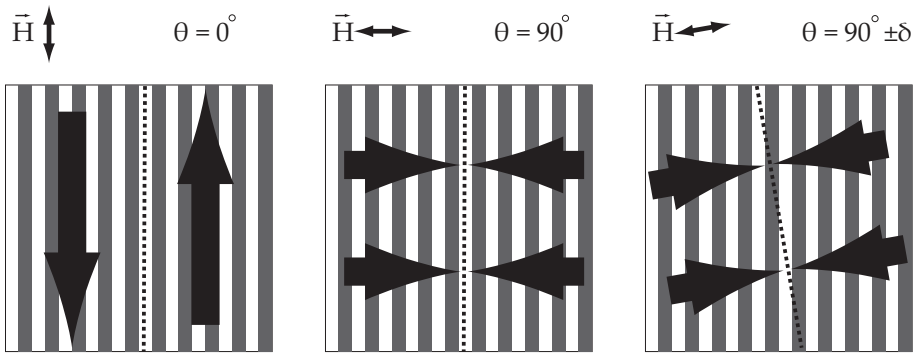

Figure 5.17: *Schematic top-view of magnetised line structures, with a domain wall aligned along the line direction (left and centre), for domains magnetised parallel (left) or perpendicular (right) to the line direction, or for a domain wall at a slight angle to the line direction with a magnetisation perpendicular to the line direction.*

coercivity for applied field perpendicular to the lines structures is not explained by this easy axis. Currently we have no complete understanding of this behaviour, as the expected hard axis perpendicular to the line direction should give no remanent magnetisation for zero applied field. Since we observe there is a remanent magnetisation perpendicular to the lines, a potential explanation for the increased coercivity can be found in pinning of domain walls on the line structures, similar to the pinning observed in Figure 5.16.

Domain walls in Fe have typical widths in the order of the height of the sample [28], which is also observed in the simulations in Figure 5.16. The domain walls in 30 nm thick samples are thus smaller than the period of the line structure of 186 nm. The domain wall is therefore located locally at either a valley or a top of the line structures. As we have concluded earlier that the energy of a domain wall is height dependent, the height dependent energy is minimized for the configuration of the domain wall along the direction of the lines as shown in Figure 5.17. As a domain wall is aligned parallel to the line direction, it is oriented at an angle θ to the applied field, just like the lines. It is known that alignment of domain walls at an angle $\theta = 0^\circ$ as shown on the left of Figure 5.17 is energetically favorable [89], but so-called head-to-head domain walls as shown in the centre of Figure 5.17 have also been observed [90].

A simple schematic shown in the right of Figure 5.17, indicates that even a small angular deviation of the direction of the domain wall, will directly reduce the pinning of the domain wall on the line structures. If fields applied at a small angle from the $\theta = 90^\circ$, can change the alignment of the domain wall and reduce the pinning of the domain wall, this could explain the very sharp angular decrease of the coercivity around $\theta = 90^\circ$ observed in the experiments. Unfortunately the results of simulations in 5.6.1 already indicated that, using the LLG micromagnetic simulator, no stable magnetisations for $\theta = 90^\circ$ at zero applied field can be created. It is therefore

not possible to model the configurations in the centre and right of Figure 5.17. Additional pinning mechanisms, such as pinning on crystal defects or contaminations are probably present in our samples and can allow for stable magnetisations along $\theta = 90^\circ$, however this has not been modelled.

In conclusion we state that the observed magnetic behaviour in our atom lithographically structured samples indicates an isotropic increase of the coercivity with increasing line structure height for the 15 nm samples and for the shallow line structures on the 30 nm thick samples. Assuming that the lines form an effective roughness that is isotropic, the increase in coercivity is in line with behaviour observed in other studies of Néel type switching. The highest line structures in 30 nm samples do show anisotropy. They showed an increased coercivity for $\theta = 0^\circ$, which decreases with increasing θ, indicating an easy axis along the direction of the lines, in accordance with micromagnetic simulations and literature. However, at angles near $\theta = 90^\circ$ the coercivity of the highest lines increases sharply and at $\theta = 90^\circ$ the highest coercivity is observed. This behaviour is not well understood, but a possible mechanism is introduced, based on pinning of domain walls along the lines for the $\theta = 90^\circ$ configuration. Further micromagnetic analysis of domain walls combined with direct observation of the domain walls on atom lithographic samples is required to understand the observed effects.

5.7 Magnetic properties of co-deposited Fe_xNi_{1-x}

In this section we present the first study of Fe_xNi_{1-x} co-deposited atom lithographic structures. As atom lithography uses near-resonant light fields to structure depositions of atomic beams, co-depositing two atomic species allows for the structuring of one of these two materials, while the other is deposited uniformly. This creates a periodic modulation of the composition with a period of $\lambda/2$. The basic concept is shown in Figure 5.18 for Fe_xNi_{1-x}. Earlier experiments have been performed with structured Cr in a background of MgF_2 [91] and Cr in a background of Co [92]. The latter system was shown to have a magnetic easy axis along the structures of the lines.

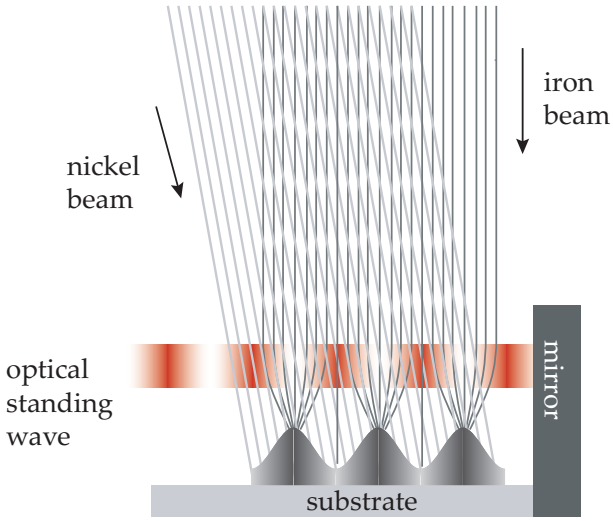

Figure 5.18: *Schematic view of co-deposition of FeNi in which Fe is structured with atom lithography as the optical standing wave is resonant with Fe and not with Ni.*

A layer of 30 nm average thickness was deposited with an average composition of $Fe_{60}Ni_{40}$ on a substrate of SiOx by thermal evaporation of separate beams of Fe and Ni during 2.5 hrs. The Fe atom beam impinges on the sample perpendicularly, while the Ni atom beam is at 45 degrees with respect to the sample. The Fe is structured by a standing wave laser field with a 90 μm waist and 15 mW power. To avoid corrosion, the sample is capped with an 8 nm thick Ag layer.

With AFM it was confirmed that the $Fe_{60}Ni_{40}$ film contained an area with line structures, which is a type of structure that has not yet been reported in literature. This is shown in Figure 5.19. In the top left an AFM surface scan is shown where we observe lines. In the corresponding averaged height cross section in the top right we find that the line height is about 2 nm and the period is about 186 nm corresponding to the period of the standing wave. In Section 5.2 it was shown that the line height

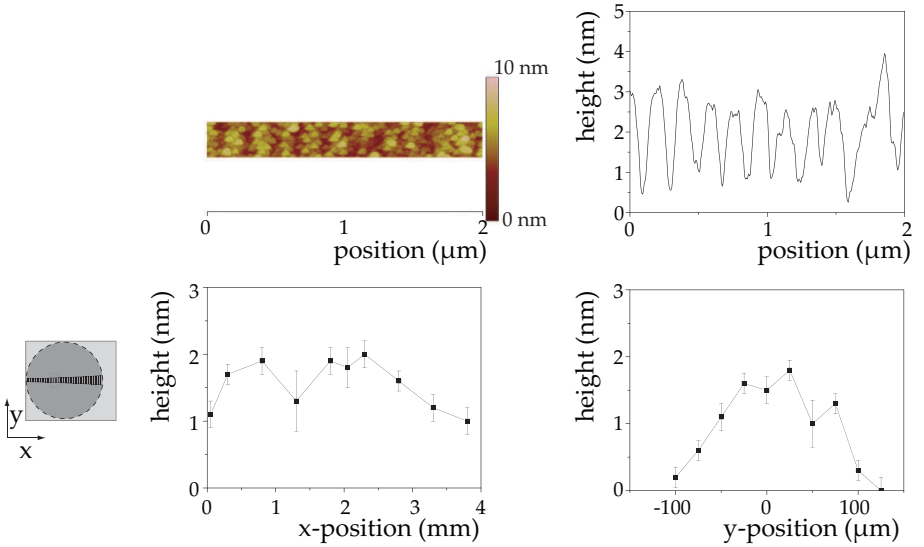

Figure 5.19: *AFM scan of atom lithographic structuring of FeNi. Top left: AFM scan of 2×0.5 μm area. Top right: average height cross section over the AFM scan area. Bottom left: schematic of sample. Bottom middle: measured maximum line height for each x-position. Bottom right: measured line height as function of y-position for $x = 2$ mm.*

is most likely obscured by the Ag capping, so that the lines are potentially higher. At the bottom of Figure 5.19 the line height is shown measured along the x-direction perpendicular to the lines and along the y-direction parallel to the lines. The structuring extends over an area of 200 μm $\times$ 4 mm, similar to the areas reported in Chapter 3 and Section 5.2 for atom lithographic structuring of Fe layers.

MOKE microscopy was used to observe the magnetic switch behaviour on this $Fe_{60}Ni_{40}$ sample in areas where lines were observed with AFM. A field of view of 448×341 μm allows simultaneous imaging of both structured and unstructured parts of the sample. An external in-plane magnetic field was applied that ramped from +7 mT to -7 mT and back in 0.05 mT steps. At each step an image representing the magnetisation in the direction of the applied field was taken with the MOKE microscope. These measurements were performed with the applied field along the lines, $\theta = 0°$, and for the $\theta = 90°$ configuration. In Figure 5.20 we show on the left schematic representations of the line area in the field of view for $\theta = 90°$ (top) and for the $\theta = 0°$ (bottom). For each configuration four typical MOKE microscopy images during the applied field ramp from +7 mT to -7 mT are shown. We find that for both $\theta = 0°$, and for $\theta = 90°$ the magnetisation in the area with lines switches its magnetisation at a different applied field compared to the unstructured area.

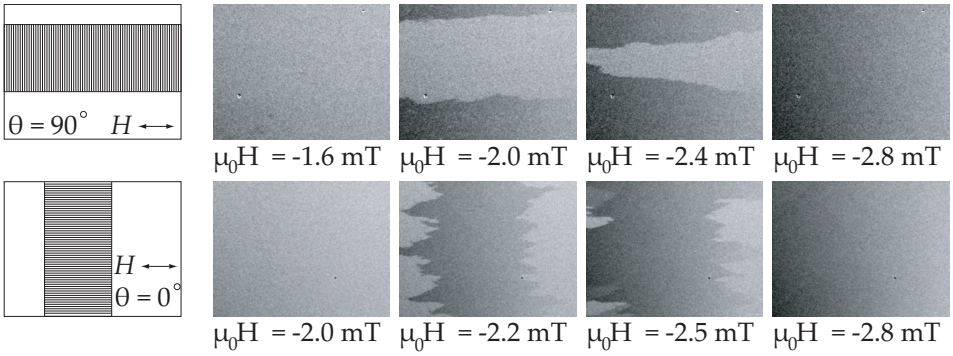

Figure 5.20: *MOKE microscopy results for the switching of atom lithographically structured $Fe_{60}Ni_{40}$ for $\theta = 90°$ (top) and $\theta = 0°$ (bottom) configurations. On the left a schematic overview of the structured area in each images is given, followed by four representative images for the applied field ramping from +7 mT to -7 mT.*

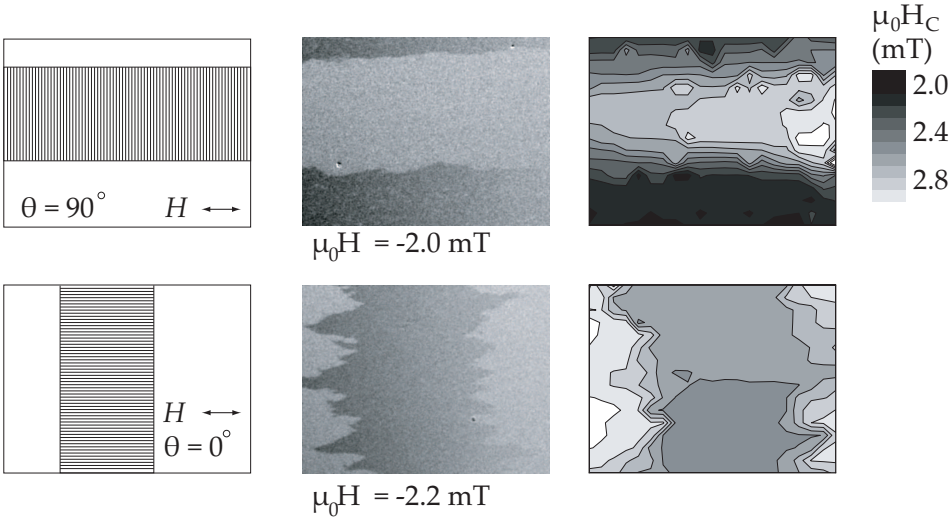

Figure 5.21: *Coercivity mapping of atom lithographic structured $Fe_{60}Ni_{40}$ measured with MOKE microscopy in a $\theta = 90°$ (top), and for the $\theta = 0°$ (bottom) configuration. On the left a schematic of the position of nanostructuring in the field of view, in the middle a typical MOKE microscopy view during a ramp of the applied field, on the right the resulting coercivity maps.*

Coercivity maps were calculated from the MOKE microscopy images for both $\theta = 90°$ and $\theta = 0°$ as described in Section 5.4. They are presented in Figure 5.21. The structured area is clearly recognisable in the $\theta = 90°$ coercivity map, whereas the structured area is less clearly visible for $\theta = 0°$.

Table 5.1: *Values for $\mu_0 H_C$ for the structured area and the background in atom lithographically structured $Fe_{60}Ni_{40}$.*

configuration	structured area	unstructured area
$\theta = 0^o$	2.6±0.1 mT	2.9±0.1 mT
$\theta = 90^o$	2.9±0.1 mT	2.2±0.1 mT

The coercivities of the structured and unstructured areas are shown for $\theta = 90^\circ$ and $\theta = 0^\circ$ in Table 5.1. The largest difference in coercivity is in the unstructured area, which makes further analysis troublesome. The high coercivity of the unstructured area for $\theta = 0^\circ$ indicates an anisotropy with an easy axis along $\theta = 0^\circ$ in the unstructured area. This could be due to magneto-crystalline growth of the unstructured area. Comparing the coercivities of the structured area, the coercivity is higher for $\theta = 90^\circ$ than for the $\theta = 0^\circ$ configuration, which indicates an anisotropy contribution with easy axis perpendicular to the line direction. A complete angular scan of the coercivities of the structured and unstructured areas provided more insight into the anisotropy of Fe layers in Section 5.4 and 5.5, but this data is not available for these co-deposited structures.

A second observation that points to an influence of the structuring on the magnetic properties of the layer is in the observed switching behaviour of the domain walls in Figure 5.20. For $\theta = 90^\circ$ the domain wall is smooth and aligned perpendicular to the direction of the lines and moving in the direction of the lines as the applied field is ramped. For $\theta = 0^\circ$ the domain wall is jagged and although it is still on average aligned perpendicular to the lines, the domain wall changes position in seemingly unpredictable steps. In the $\theta = 0^\circ$ MOKE images of $\mu_0 H =$ -2.2 mT and $\mu_0 H =$ -2.5 mT this is visible, e.g., in the top right corner of these images the magnetisation switches and the domain wall moves, while in the area next to it the domain wall has not moved at all.

The formation of jagged or zig-zag structures is known for 180° domain walls, which are walls in between antiparallel magnitised areas. The most favorable alignment of such a domain wall is parallel to the field, but if this is not possible the domain wall can locally reorient, to minimize its energy [89]. As the structured area forms a barrier to the domain walls, this barrier is at 90° with respect to the applied field in the $\theta = 0^\circ$ configuration, which can explain the formation of zig-zag structures is this case. This behaviour was not observed in the structured Fe layers, which indicates that the combination of geometric line structures and the periodic modulation of Fe_xNi_{1-x} content has a different interaction with the domain walls that the only geometrically modulated Fe layers.

5.8 Conclusions

In this chapter three experiments were presented. Firstly, we have shown that using MOKE microscopy it is possible to find a clear magnetic signature of atom lithographic structuring of Fe in 15 nm thick layers of Fe, in contrast with earlier reports of Myszkiewicz et al. [19] and Smeets [25]. Structuring of Fe increases the coercivity of the structured area isotropically for 15 nm thick layers. This indicates that these structures do not give a significant magnetic anisotropy, but that the structuring can be seen as isotropic roughness, increasing the coercivity of these thin layers. Assuming that the lines form an effective roughness that is isotropic, the increase in coercivity is in line with behaviour observed in other studies of thin films with Néel type switching.

In a second experiment we have studied 30 nm thick samples. In these samples shallow line structures give an isotropic increase in coercivity similar to what is observed in 15 nm thick samples, however the highest line structures on these samples show a distinct anisotropic behaviour. The coercivity is high for $\theta = 0^\circ$ and decreases for an increasing angle θ, indicating an easy axis along the direction of the lines. This easy axis is in accordance with micromagnetic modelling and literature. However around $\theta = 90^\circ$, there is a sharp increase of the coercivity, so that the highest coercivity for the highest lines is observed for the $\theta = 90^\circ$ configuration. This is not in agreement with micromagnetic modelling, nor is it reported in literature. This behaviour is not well understood, but a possible mechanism is introduced, based on pinning of domain walls along the lines for the $\theta = 90^\circ$ configuration. Further micromagnetic analysis of domain walls combined with direct observation of the domain walls on atom lithographic samples is required to truly understand the observed effects.

Finally we have presented the first results of atom lithographic co-deposition experiments of $Fe_{60}Ni_{40}$, showing that this technique allows for nanostructuring over areas of 200 μm $\times$4 mm size. We have shown with MOKE microscopy that the nanostructuring influences the switching behaviour for the $\theta = 0^\circ$ and $\theta = 90^\circ$ configurations differently. Both the shape of domain walls changes as well as the observed coercivity. However, significant effects were also found in the background, limiting the analysis.

Chapter 6

All-optical focusing of neutral atom beams.

In atom lithography, atom beams are usually focused by standing wave light fields to arrays of points or lines with sizes on the order of 10 nm spaced by half an optical wavelength. Magneto-optical compression can be used to compress thermal atom beams to the order of 10 μm. We evaluate the possibilities of focusing such a magneto-optically compressed thermal atomic beam directly to a *single* point of 100 nm diameter, using all-optical masks. Such a focused beam could be used as a 'nanopencil' for depositing nanostructures. To this end we developed a modular Monte Carlo atom tracking program in which the effects of initial beam divergence, magnetic substructure, laser cooling, and spontaneous as well as stimulated diffusion are included and apply it to a number of promising light field configurations. We find that optical focusing or funneling a thermal beam to 100 nm is not possible within realistic experimental limits when all effects are considered. The main cause is the combination of the destructive heating effect of stimulated diffusion and the limited available interaction time for cooling. Thus, an all-optical atomic nanopencil will require a slow and monochromatic atom beam. This seriously complicates the practical application of such a device as a writer.

6.1 Introduction

Over the last decades many techniques have been developed that can be used to create ever smaller mechanical, optical and electronic devices. These include optical lithography, charged particle lithography, assembly of atoms using scanning probes and various self-assembling techniques [93]. One promising option, based on the dipolar interaction between near resonant light fields and neutral atoms, is direct-write atom lithography [36, 68]. As this is a single step deposition method using beams of neutral atoms, it allows for the deposition of pure materials, unlike electron-beam or focused ion beam (FIB) induced deposition where deposited materials usually contain from about 10 up to 80% of contaminations [94]. direct-write atom lithography can be applied to any substrate, although the interaction between the deposited atomic species and the substrate can be of influence for the produced structures [95]. Furthermore, as the technique uses no mechanical masks, it is not subject to degradation or clogging of masks. Atom lithography is thus very suitable to create nanostructures.

In atom lithography, standing wave intensity patterns of a near-resonant light field are used. This allows for the production of highly periodic structures, with wavelength or sub-wavelength periodicity, in one, two or even three dimensions. Structure sizes down to 20 nm [96] have been achieved with 589 nm light, clearly below the diffraction limit that limits classical optical lithography. However, it should be noted that atom lithography can only use wavelengths that are nearly resonant with strong transitions in atoms. Thus, the basic method is restricted to producing simple, periodic structures with a limited choice of periods.

To overcome these restrictions different options have been proposed. Two main approaches are the use of non-periodic, holographically created light fields [13], and tailoring the light field geometry to achieve tight focusing of a beam of atoms to a single spot. This spot can then be used for serial writing of arbitrary nanostructures analogous to electron beam or ion beam writing. Here, we further investigate the possibility to tightly focus an atom beam to a single spot.

Bjorkholm et al. observed in 1978 the first focusing of atom beams in a traveling Gaussian laser beam [97], after which various different focusing schemes have been proposed theoretically. These include using blue detuned hollow TEM01* [98, 99] or Bessel J1 [100] laser beams and blue-detuned near-field lenses [101]. These theoretical models predict focused beam spots down to the nanometer or even sub-nanometer range [98, 102]. The only actual implementation of a focused 'atom beam pencil' uses focusing by static magnetic quadrupole fields instead of light fields, combined with physical aperturing. It has been used to write structures of 280 nm diameter [14]. There are thus more than two orders of magnitude between the theoretically proposed and experimentally achieved single spot focus size.

Chromatic and spherical aberration limit the achievable focus size in the all-optical schemes. Chromatic aberration arises when atoms with different axial velocities are

focused, because the focal length of an atom-optical lens is velocity-dependent. It can be overcome by compressing the axial velocity distribution of the atom beam, e.g. using a Zeeman slower or by using a supersonic expansion source. Spherical aberration is caused by the fact that the shape of real optical focusing potentials are not the ideal parabola of a particle lens. Using a small aperture size (the spatial range over which atoms enter the focusing potential), spherical aberration can be reduced, as the optical lens will be more quadratic over a small range. The use of small, monochromatic incoming beams can thus overcome chromatic and spherical aberrations, but this severely limits the achievable flux.

The availability of non-conservative cooling forces in atom optics allows the use of optical funnels instead of optical lenses. In these funnels the transverse movement of the atoms is damped during the focusing process, providing three main advantages. First, it allows for a much larger capture range. Second, it will give a collimated as well as focused beam, which is easier to use than a tightly focused atom beam with a small depth of focus. Finally, it allows for the use of thermal beams, which have a large axial velocity spread, as a funnel is less sensitive to chromatic aberration. Optical funnels are therefore more suited for focusing atomic beams than optical lenses.

In this article we investigate the possibilities to focus or funnel thermal atomic beams to a sub-100 nm radius, using only optical forces. We start out with beams that are pre-compressed and collimated using magneto-optical compression to a 10 μm radius. This is known to be experimentally achievable [103]. This way we hope to obtain a high localized flux and thus fast deposition rates. Although previous theoretical work predicted atom lithographic focussing to even (sub)-nanometer ranges [98, 102], this article will focus on experimentally achievable limits on both the incoming atom beam as well as on the light fields and include all heating effects to remain within experimentally achievable limits.

To this end we have developed a modular simulation program, based on Monte Carlo atom tracking. The program allows for the inclusion of focusing, heating and cooling effects, initial beam divergence, axial velocity spread, and a distribution over magnetic sub-states. This allows us to evaluate different options for focusing and funneling, and to obtain a clear insight into the relative importance of the various physical effects in atom lithography.

In all calculations in this work we use chromium as a model system. Chromium is the best studied system for atom lithography [15], with a well-accessible optical transition suitable for focusing as well as cooling. It forms stable nanostructures and is relevant as interconnect material. The relevant parameters of chromium that are used are given in Table 6.1.

Table 6.1: *Properties of chromium.*

transition	$a^7S_3 \rightarrow z^7P_4$,
wavelength (λ)	425.55 nm
line width (Γ)	5.0 (2π) MHz
saturation intensity (I_s)	85.09 W/m^2
Doppler temperature (T_D)	120 μK
Doppler velocity (v_D)	13 cm/s
single photon recoil velocity (v_R)	1.8 cm/s
atomic mass (m)	52 amu

6.2 Theory

Before discussing specific light fields suitable to focus or funnel atoms to a single focal point, we will describe the general framework used for calculating the atomic motion in a light field. In this section will describe the potential field of an atom in a near resonant light field in the so-called dressed state model, which is based on a quantum mechanical description of the combined states of the atom and the light field [41]. Within this model we will describe the effects of spontaneous emission, which lead to the so-called logarithmic potentials. This framework will be used in the next section to estimate the suitability of two light fields to focus or funnel an atomic beam to a sub-100 nm diameter.

The dressed state model describes a two-level atom in a near resonant light field. A light field that is tuned near resonance with an atomic transition has a dipole interaction with an atom, leading to a potential field for the atom. The Hamiltonian of the system is given by $H = H_a + H_l + H_{int}$. Here H_a is the Hamiltonian of the free atom, H_l describes the light field and H_{int} describes the dipole interaction between the atom and the light field. The eigenstates of the free atom are denoted by $|g\rangle$ and $|e\rangle$, the eigenstates of the (single mode) light field are given by the photon number states $|n\rangle$. The eigenstates of the full Hamiltonian, which can be expressed as superpositions of the $|g\rangle|n\rangle$ and $|e\rangle|n\rangle$ product states, are called the dressed states.

If we assume a light field with a spatially varying intensity $I(\vec{r})$, which is detuned by Δ from a resonant transition with a natural line width Γ and a saturation intensity I_s, the effective coupling of the atom to the light field is described by the Rabi frequency $\Omega(\vec{r})$, given by:

$$\Omega(\vec{r}) \quad = \quad \Gamma\sqrt{\frac{I(\vec{r})}{2I_s}}. \tag{6.1}$$

In this light field the dressed states can be described as superposition states of the ground state $|g\rangle$ and the excited state $|e\rangle$ according to [41]:

$$\begin{aligned} |1,n\rangle &= \sin\theta|g\rangle|n+1\rangle + \cos\theta|e\rangle|n\rangle, \\ |2,n\rangle &= \cos\theta|g\rangle|n+1\rangle - \sin\theta|e\rangle|n\rangle, \end{aligned} \tag{6.2}$$

where the angle θ is defined by

$$\cos 2\theta \equiv -\frac{\Delta}{\sqrt{\Omega^2+\Delta^2}}. \tag{6.3}$$

For a light field with detuning $\Delta \geq 0$, i.e., a blue-detuned light field, the $|1\rangle$ state projects more on the atomic ground state, while the $|2\rangle$ state projects more on the atomic excited state. In the limit of low light intensity and/or large detuning, the correspondence is complete. In case of a red-detuned light field with $\Delta \leq 0$ the $|2\rangle$ state projects more on the ground state and the $|1\rangle$ state more on the excited state.

Assuming a fixed photon index n in Eq. 6.4, after subtraction of a common energy contribution of the photons, the energies of the dressed states are given by:

$$E_{1,2} = -\frac{\hbar\Delta}{2} \pm \frac{\hbar}{2}\sqrt{\Delta^2+\Omega^2}. \tag{6.4}$$

For blue detuning, ground state atoms entering the light field will initially be in the $|1\rangle$ dressed state. This state has the lowest energy for the minimum intensity of the light. For red detuning, ground state atoms start in the $|2\rangle$ state, which has the lowest energy for the intensity maximum. A red detuned light field can therefore focus atoms towards a local intensity maximum, whereas a blue detuned light field focuses towards a local intensity minimum.

The potential landscapes of dressed states are similar to classical dipole potentials, but the effects of spontaneous emission in the dressed state model are different from any classical model. As the dressed states are superposition states of the ground and excited states, atoms can undergo spontaneous emission from both $|1,n\rangle$ or $|2,n\rangle$ state to either the $|1,n-1\rangle$ or the $|2,n-1\rangle$state. Both dressed states can undergo spontaneous emission and the dressed state of an atom can change upon spontaneous emission, thus leaving the atom in a different potential landscape. Changing the dressed state reverses the sign of the position dependent part of the potential (Eq. 6.4) and thus the sign of the force due to this potential reverses. The randomness in the atom's motion introduced by these force reversals is known as 'stimulated diffusion', to separate the effect from the direct heating by the random photon recoils associated with the spontaneous emissions ('spontaneous diffusion').

To create a truly confining potential, the effects of diffusion need to be decreased. This can be done by minimizing the spontaneous emission decay rates. Spontaneous emission is governed in the dressed state model by four rates, describing all possible transitions [41]:

$$\Gamma_{12} = \frac{\Gamma}{4}\left(1+\frac{\Delta}{\sqrt{\Omega^2+\Delta^2}}\right)^2, \tag{6.5}$$

$$\Gamma_{21} = \frac{\Gamma}{4}\left(1-\frac{\Delta}{\sqrt{\Omega^2+\Delta^2}}\right)^2, \tag{6.6}$$

$$\Gamma_{11} = \frac{\Gamma}{4}\left(1-\frac{\Delta^2}{\Omega^2+\Delta^2}\right), \tag{6.7}$$

$$\Gamma_{22} = \Gamma_{11}, \tag{6.8}$$

where Γ_{ji} is the transition rate from level i to level j. If we assume a blue detuned system, we try to focus the ground state–like $|1\rangle$ dressed state. Spontaneous diffusion is governed by the Γ_{11} decay rate, stimulated diffusion by Γ_{21}. Both rates can be minimized either by making Δ large, or Ω small, i.e. by increasing the detuning or decreasing the light intensity. Applying the same reasoning, it can be shown that this conclusion also holds for a red detuned system.

However, in any real experiment a finite detuning and Rabi frequency will be needed and the effects of spontaneous emission cannot be neglected. Dalibard and Cohen-Tannoudji [41] derived an expression for the time-averaged potential acting on a (stationary) atom in the presence of dressed-state-changing spontaneous emissions. The result is the so-called logarithmic potential:

$$U_{log}(\vec{r}) = \frac{\hbar\Delta}{2}\log\left(1+\frac{\Omega^2}{2\Delta^2}\right). \tag{6.9}$$

This potential is often used in atom-optical calculations. For $|\Omega/\Delta| \ll 1$, it equals the potential of the ground state–like dressed state, while for larger values of $|\Omega/\Delta|$ it saturates. Petra et al. [104] showed that for non-stationary atoms, such as atoms moving in a periodic potential, the logaritmic potential is no longer fully valid and the velocity effects change the funneling significantly. In the regime of larger values of $|\Omega/\Delta|$ stimulated diffusion becomes important as well. When using the averaged force for actual calculations, care has to be taken to include the increased diffusion. In this work, for numerical simulations we will follow a different approach based on the dressed state potentials combined with a Monte-Carlo treatment of all spontaneous emission effects (see Section 6.4). We will use the logarithmic potential to obtain simple estimates of atom focusing.

With this understanding of atom-optical potentials, we have chosen two light fields that can be used as atom lenses or funnels. These will be discussed in the next section.

6.3 Focusing Potentials

To provide a focusing or funneling potential we showed that either a blue detuned field focusing towards an intensity minimum or a red detuned field focusing towards an intensity maximum is needed. We consider two possibilities for such configurations: a blue detuned laser beam with a Laguerre-Gaussian TEM01* mode (hollow beam), and a red detuned optical field inside an axially symmetric conical mirror with a vertex angle of 90° (axicon light field). The corresponding potentials have the advantage that they have only one minimum or maximum, while the potential extends over a area of more than 10 μm diameter, thus providing a capture area suitable for the incoming atom beam while focusing it to a single spot. In Figure 6.1**a** and **b** we show schematically how an atomic beam is compressed by a hollow beam or an axicon light field.

The first field we investigate is the laser beam with the hollow TEM01* mode. The intensity of the light in this configuration is described by [105]:

$$\begin{aligned} I_{hb}(r,z) &= \frac{4P_0 r^2}{\pi w(z)^4} \cdot e^{-\frac{2r^2}{w(z)^2}}, \\ w(z) &= w_0\sqrt{1+\left(\frac{z}{z_R}\right)^2} \end{aligned} \tag{6.10}$$

with P_0 the laser radiation power, w_0 the waist radius of the laser beam, $z_R = \frac{\pi}{\lambda} w_0^2$ the Rayleigh length and λ the wavelength of light. The intensity profile of the hollow beam at a fixed z-position shows a local minimum at $r = 0$ and two maxima at $r = \pm w_0\sqrt{\frac{1}{2}(1+(z/z_R)^2)}$ with an intensity $I_{max} = 2P_0 \mathrm{e}^{-1}/(\pi w_0^2(1+(z/z_R)^2))$.

To investigate the funneling ability of such a hollow beam we look at the atom-light potential using the logarithmic potential $U_{log}(\vec{r})$. Assuming a focused TEM01* beam with detuning $\Delta = 100$ (2π) MHz, power $P_0 = 250$ mW and a waist of $w_0 = 25$ μm we can achieve an intensity and potential landscape in the focus as shown in Figure 6.1**c** and **e**. The potential of the hollow beam light field is in first order quadratic around the center, thus providing good options for focusing, as a quadratic potential is an ideal particle lens.

Assuming a transversely Doppler cooled incoming atom beam, which we compress isothermally by increasing the strength of the quadratic potential, the atoms are restricted to an area where the potential energy is comparable to the transverse energy of Doppler cooled atoms. Increasing the strength of the potential occurs automatically as the atomic beam travels along the axis of the hollow beam and approaches the waist. In the potential landscape we have indicated the transverse kinetic energy level of the Doppler cooled atoms ($E_{kin} = \hbar\Gamma/2$). As is shown in the figure, the radius of the area where the potential energy is less than the kinetic energy of Doppler cooled atoms is approximately 100 nm. It should be noted that isothermal compression

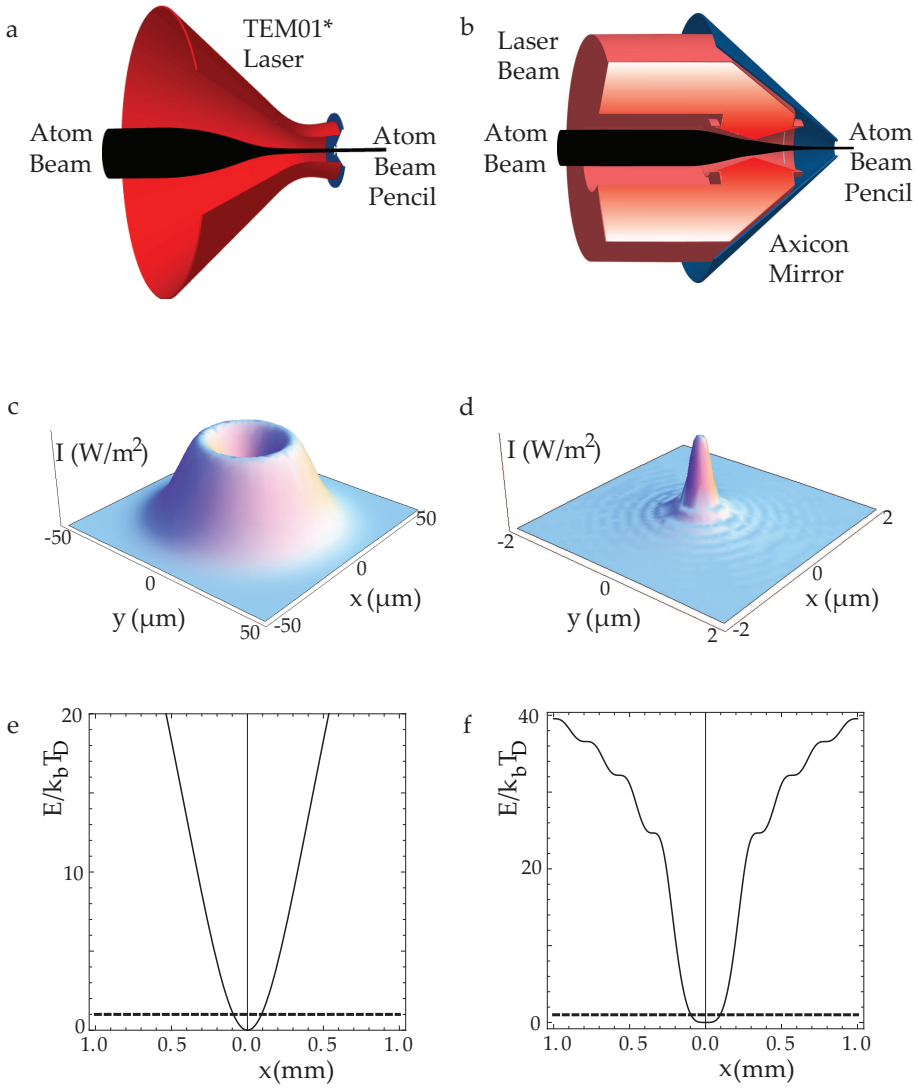

Figure 6.1: *Two schematic possibilities for all optical beam funneling using a TEM01* blue detuned field (**a**) or red detuned beam reflection on an axicon mirror (**b**), with their corresponding intensity distribution (**c**,**d**) and a cross section of the energy landscape assuming a logarithmic potential (**e**,**f**) for typical values of power, waist and detuning. In **e** and **f** the dashed line represents the transverse kinetic energy of a Doppler cooled atom beam.*

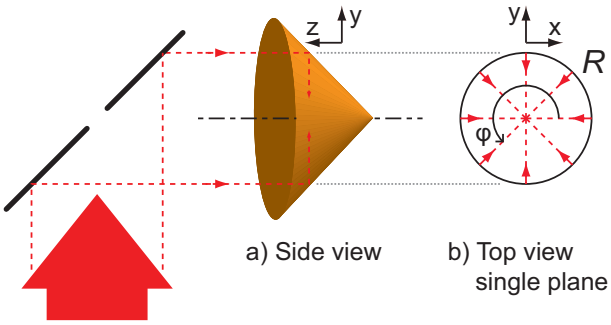

Figure 6.2: *A schematic representation of an axicon mirror.* ***a****) Incident light rays parallel to the center line of the axicon travel in planes perpendicular to the center line after reflection.* ***b****) In one single plane, with radius R, all rays cross the heart line. The direction of the reflected light ray is defined by ϕ, the angle of the light ray with the x-axis in the plane.*

requires continuous cooling to maintain the transverse temperature at the Doppler limit.

If isothermal compression is not possible and we consider the potential landscape to be conservative, Liouville's theorem states that phase space density is conserved. Therefore a 50 fold adiabatic compression in both lateral directions from 5 μm to 100 nm will lead to a increase of the lateral momenta by a factor of 50, i.e., an increase in the transverse energies by a factor of 2500. As a result, the required increase in strength of the quadratic potential to achieve this compression is much larger than in the case of isothermal compression. For a fixed maximum potential strength, the compression factor for adiabatic compression is equal to the square root of the isothermal compression factor. For the potential of Figure 6.1**e**, this leads to a final beam radius of 0.7 μm.

The second light field we proposed for focusing is a red detuned axicon light field. This field is created by letting a parallel light beam reflect on an axially symmetric conical mirror with a vertex angle of 90° as shown in Figure 6.1**b** and Figure 6.2. In this configuration all light rays pass through the central axis, leading to an optical line focus on axis. The exact intensity distribution around the central axis is determined by the polarization of the incoming beam, which can lead to constructive or destructive interference on axis. In [100], a radially polarized incoming light field with blue detuning is proposed, which leads to zero intensity on axis and a dipole potential that is in first order quadratic around the axis, thus forming a good lens. However, it has a ring-shaped potential maximum at less than half a wavelength distance from the axis. As a consequence, the capture range of atoms into the potential is limited to less than a wavelength.

We propose to use a circularly polarized red-detuned incoming light beam with a Gaussian beam profile. To calculate the intensity distribution in this geometry, we start out with a right hand circularly polarized beam traveling in the $-z$ direction:

$$\vec{E}_{incoming} = E_0 \cdot \mathrm{e}^{-r^2/w_0^2} \cdot (\hat{x} + i\hat{y}) \cdot \mathrm{e}^{ikz} \cdot \mathrm{e}^{-i\omega_L t}, \tag{6.11}$$

with $k = \frac{2\pi}{\lambda}$ the wave number of the incident wave, w_0 the waist of the incoming Gaussian beam, $r = \sqrt{x^2 + y^2}$ the distance from the axis and E_0 the on-axis amplitude of the wave. Here, the z–dependence of the electric field is neglected, which is valid in good approximation for the large beam waists being considered here.

The beam is reflected by the axicon mirror, whose tip is in the origin of our Cartesian system and whose cone is in the $+z$ direction. The light field inside the axicon can now be calculated: the full derivation is given in Appendix A of this chapter. The result for the total intensity is:

$$\begin{aligned} I_{ax}(r,z) &= \frac{2P_0 k}{w_0^2} \cdot z\mathrm{e}^{-2(\frac{z}{w_0})^2} \times \\ &\times \left\{ J_1^2(kr) + \left(J_0(kr) - \frac{J_1(kr)}{kr} \right)^2 + \frac{J_1^2(kr)}{(kr)^2} \right\}. \end{aligned} \tag{6.12}$$

In this field distribution it is comparatively easy to create high intensities and high radial intensity gradients, as all power passes through the optical axis. However, this configuration does not lead to a quadratic potential near the axis, but to a fourth order dependence of the potential on the radius. This potential should therefore not be useful as a good lens.

To create an optical funnel, sufficient interaction time is needed, leading to an optical field distributed over a large axial length. Axial lengths of the potential field of centimeters are required. As the width of the incoming laser beam is projected onto the z-axis, we will also require the waist of the incoming laser beam to be of the order of centimeters. As the axicon potential traps atom in a intensity maximum, it is now essential that we include saturation effects. Therefore we use the logarithmic potential. In Figure 6.1**d** we show the intensity distribution in the plane $z = \frac{1}{2}\sqrt{2}w_0$, for a detuning $\Delta = 100$ (2π) MHz, power $P_0 = 50$ mW and a waist of $w_0 = 50$ mm. In Figure 6.1**f**, the corresponding potential energy landscape is shown. As a comparison the transverse energy of a Doppler-cooled beam is given by the dotted line, indicating that a laser cooled atom beam can possibly be funneled to a beam with a radius of 100 nm.

From the basic arguments presented in this paragraph, we might conclude that both proposed light fields can be used to focus a beam of neutral atoms to sub-100 nm dimensions. However, the strongly inhomogeneous light field configurations considered here are complicated from an atom optics viewpoint. For simulations, heating by photon recoils can be included in a Fokker-Planck type calculation of atomic ensembles with an averaged force and a diffusion coefficient. However, the character

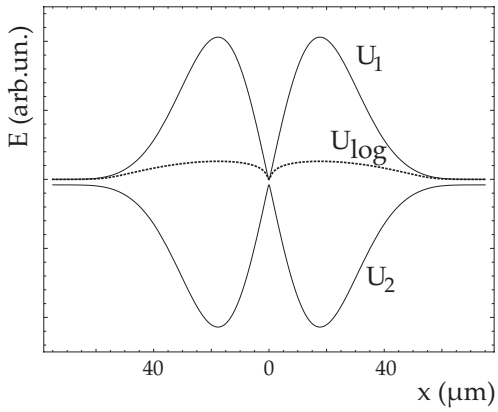

Figure 6.3: *Potential energy levels of an atom in a TEM01* hollow beam assuming a dressed state model (U_1 and U_2) or a logarithmic potential (U_{log}) at high intensities s_{max}=10^6, like in Figure 1.*

of the stimulated diffusion (large changes in acceleration, spaced widely in time) does not lend itself to this approach.

As an example, consider the dressed-state potentials of an atom in the field of a TEM01* hollow beam. Figure 6.3 shows the two dressed state potentials U_1 and U_2 at high maximum intensity (effective saturation parameter $s = I_{max}/I_{sat} = 10^6$), as well as the potential U_{log} which is the time-averaged potential for an atom held at fixed position. During the actual interaction with the light field the atom follows U_1 or U_2 until a spontaneous emission takes it from one curve to the other. The motion of the atom obviously deviates drastically from the motion of an atom experiencing the averaged force. Specifically, a dressed state change turns a confining potential into a potential expelling the atom from the intended capture region. Therefore, a single dressed state change can even be a fatal event, after which the atom never makes it back to the capture region.

The main differences between the two proposed light fields when used as a lens is that the hollow beam light field in first order leads to a quadratic potential, representing a good lens, whereas the axicon light field in first order leads to a quartic potential, corresponding to a lens with severe aberrations. However, as these systems will also be used as funnels, we cannot say beforehand what the better solution will be. In the next section we will discuss the model we use to investigate the possibilities of both light field configurations.

6.4 Monte Carlo Model

The nature of the stimulated diffusion, discussed in the previous section, can be taken into account simply and effectively in a Monte-Carlo atom trajectory calculation. This approach offers a clear insight in the effects of spontaneous emissions and dressed state changes. Furthermore, it enables the straightforward inclusion of extra effects. Therefore we have used this to construct a flexible, modular simulation program for atom focusing and funneling. The atoms are considered as classical point particles moving in the dressed-state potentials. Initially (before they interact with the light field) the atoms are all in the dressed state adiabatically connecting to the atomic ground state. The three-dimensional dipole force vector is then calculated as the gradient of the potential of the dressed state. The trajectories are calculated by numerically integrating the Newtonian equation of motion in three dimensions. Thus, changes in axial, radial as well as azimuthal velocity components are taken into account. During the integration, the spontaneous emission rates of the dressed states according to Eq.6.5 are monitored. Random spontaneous emission events are generated according to this rate. After each spontaneous emission, a random photon recoil momentum is added to the atom's momentum and the possibility that the atom switches to the other dressed state is taken into account.

In this way dipole forces, recoil heating, stimulated diffusion, and the three-dimensional nature of the problem are accurately taken into account. However, standard low-intensity Doppler cooling and high-intensity velocity-dependent effects based on the phase of the atomic wave function (e.g., polarization gradient cooling with $\sigma^+ - \sigma^-$polarized counter running laser beams) are not included in the model.

The program is constructed in a modular way. Axicon light fields and the field of a running wave Laguerre-Gaussian TEM01* hollow light beam (the two situations investigated in this work) can be inserted, as well as regular standing waves.

For situations where one- or two-dimensional transverse laser cooling is to be added to a light field, the velocity-dependent force is added separately as an averaged force. The increased spontaneous emission then contributes to the diffusion via extra random recoils. As an example, standard Doppler cooling in a weak transverse red-detuned light field can be used to induce cooling in the dark area in the center of a blue-detuned hollow beam. In this case, the averaged force is given by:

$$F_{D,i} = F_{i+} + F_{i-} \tag{6.13}$$

where

$$F_{i\pm} = \pm \frac{\hbar k s_0 \Gamma/2}{1 + s_0 + \left(\frac{2(\delta \mp k v_i)}{\Gamma}\right)^2} \tag{6.14}$$

with $i = x$ or y, v_i the transverse velocity of the atom in the x- or y-direction, and $s_0 \equiv I_0 / I_s$ the saturation parameter of each of the counter propagating beams of the cooling standing wave. The parameter δ is the effective detuning of the Doppler cooling light, which can take into account the light shift induced by the strong focusing light field. Throughout this article we will use for Doppler cooling a detuning $\delta = -\Gamma/2$ and a saturation parameter $s_0 = 1$.

To include the effects of atomic magnetic sub-states, the atoms are uniformly distributed over all magnetic sub states and the appropriate Clebsch-Gordan coefficients are assigned to each atom. In the calculation of the forces from the gradient of the dressed energy potentials these Clebsch-Gordan coefficients are used. The possibility that the magnetic sub-state of an atom changes during spontaneous emissions is neglected.

The program also includes the possibility of switching cooling and focusing fields on and off during the compression process according to a fixed switching schedule. We have investigated such schemes as a possibility to combine focusing and cooling fields without the complicating effects of a direct interplay between the light fields.

6.5 Validation

To confirm the validity of our modular Monte Carlo simulation program, we first show results that reproduce the focusing seen in actual experiments by McClelland [15] using standing waves to focus particles. In Figure 6.4 we show the results of focusing of a chromium beam by a standing wave created by retro-reflecting a Gaussian laser beam with a waist of 0.39 mm, power $P_0 = 20$ mW and detuning $\Delta = 200$ (2π) MHz, similar to the settings in [15].

To show the effects of our modular system, we show the simulation without spontaneous emission, magnetic sub-levels, transverse or longitudinal velocity distribution in Figure 6.4**a**. The longitudinal velocity is 926 m/s, which is the most probable longitudinal velocity for a beam from an effusive source at a temperature of 1800 K. The effect of a transverse velocity is shown in Figure 6.4**b**. There the incoming beam is collimated to 0.2 mrad (FWHM), representing a realistic beam transversely cooled using polarization gradient cooling [15]. The effect of longitudinal velocity spread is shown in Figure 6.4**c**, where a perfectly collimated thermal beam is modelled, having a rms velocity spread of 366 m/s. The effect of including magnetic sub-levels is shown in Figure 6.4**d**. The effect of spontaneous emissions is included in Figure 6.4**e** and finally a complete modelling including all effects is given in Figure 6.4**f**. These images give a clear insight into the nature of the various effects that limit focusing. The longitudinal velocity spread is clearly the most limiting factor, followed by the magnetic sub-states and the transverse velocity distribution. Spontaneous emissions are not of much influence, as the interaction time of the atoms with the light field in this configuration is in the order of the lifetime of the dressed states. In Figures 6.4**a**,

b, **d** and **e** haloes due to spherical aberrations can be seen. In Figure 6.4**c** and **f** the chromatic aberration introduced by the thermal longitudinal velocity distribution broadens the separate contributions so that the haloes are no longer visible.

The results shown in Figure 6.4 **f** give a FWHM of the structures of 55$\pm$1 nm, below the experimentally observed line widths of 65$\pm$6 nm reported in [15]. This is reasonable as we do not take into account any surface diffusion effects, which lead to a broadening of lines as was shown in Chapter 3 and in [44, 43]. Considering the good results of our model for an experimentally known system, we can now consider the results of the model for the proposed hollow beam and axicon light field.

6.6 Hollow beam

Focused TEM01* hollow beam light fields can be represented by three parameters: the waist w_0, the detuning Δ and the power P_0. To focus an atom beam in such a co-propagating hollow laser beam, the atom beam needs to enter the light field at some point. This is most easily achieved, by letting the light field reflect off a mirror with a hole in it so that the atom beam can enter the light field parallel to the propagation direction of the light field via the hole. Such a setup does create an additional parameter: the distance z_{int} between the point where the atom beam enters the light field and the focus of the light field.

All parameters are limited by fundamental as well as practical limits. The power P_0 is limited by experimentally available power. A TEM01* laser mode at 425 nm will most usually be created by frequency doubling a TEM00 mode from a Ti:S laser. From this doubled TEM00 mode, a TEM01* mode can be created using e.g. a holographic phase plate. Such a system will certainly not generate more than 2 W in power, which we take as an upper limit in our modelling. For low power, heating effects due to spontaneous emission will be less, but the lower intensity gradients lead to smaller focusing forces. We use 50 mW as the lower limit on power. The minimum waist size of a focused hollow beam is limited theoretically by the diffraction limit. However, a short waist size leads to a short Rayleigh length and thus a short effective interaction time. A large waist leads to long interaction times, but large waist systems lack strong intensity gradients needed for confining an atom beam. We will show that an optimal focusing can be found for the waist ranging from 5 to 75 μm, corresponding to Rayleigh lengths of 0.2 mm and 42 mm. The distance z_{int} that the atom beam is in the light field should be a few Rayleigh lengths to have a sufficient capture range. We use limits of 10 and 60 mm. The detuning Δ is experimentally easily tunable over a large range. However, for small detunings heating effects due to stimulated diffusion limit effective focusing. Very large detunings give small potential energy levels and therefore limit the focusing power of the optical system. The range of detunings in our modelling is restricted from 50 (2π) MHz to 1 (2π) GHz.

A thermal, fast atom beam, that we propose to use in our focusing setup, will give rise to a a large Doppler shift in a a co-propagating hollow laser beam. For the

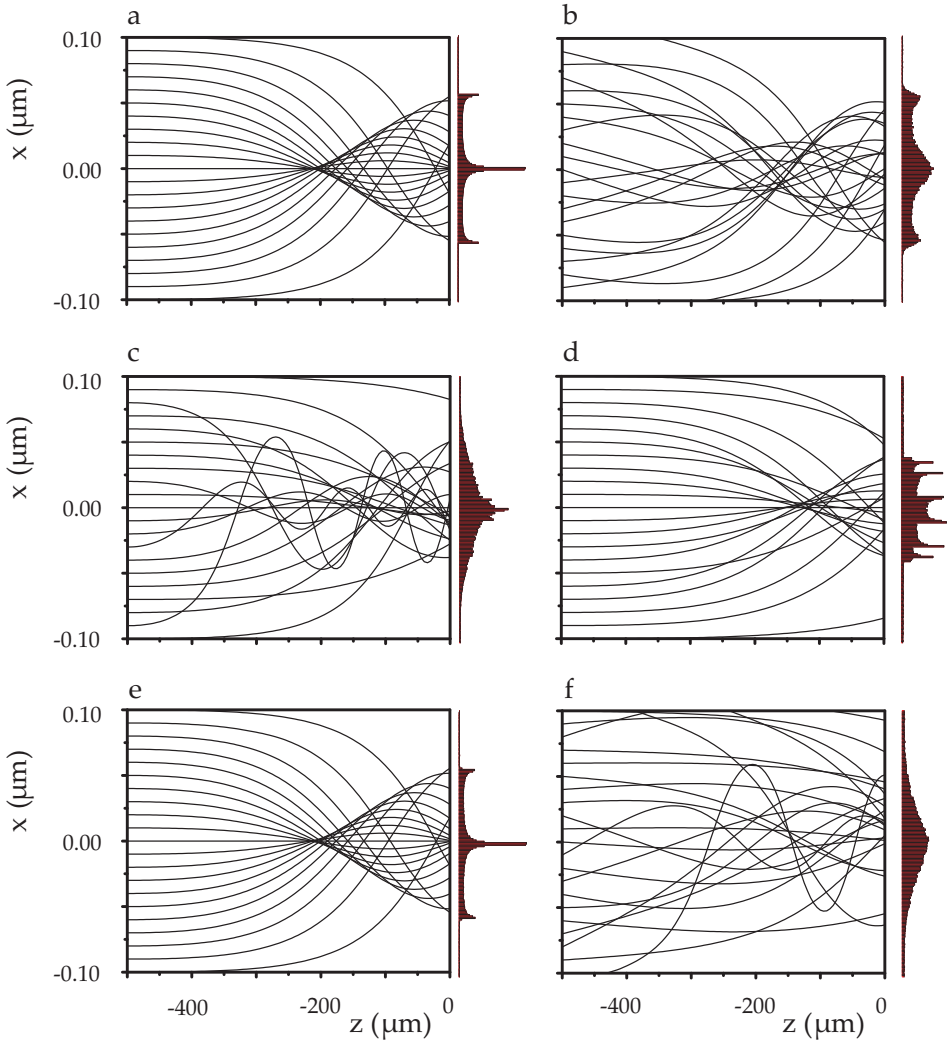

Figure 6.4: *Typical particle trajectories of atoms focused in a standing wave dipole potential created from a retro-reflected laser with $\lambda = 425$ nm , $w_0 = 0.39$ mm, power $P_0 = 20$ mW and detuning $\delta = 200\ (2\pi)$ MHz. In* **a** *we assume a perfectly collimated incoming beam with no longitudinal velocity spread, only dipole interactions without any magnetic substructure, (***b***) is as (***a***) but assuming a 0.2 mrad collimated beam,(***c***) is as (***a***) but assuming a longitudinal thermal beam, (***d***) is as (***a***) but including magnetic substructure, (***e***) is as (***a***) but adding spontaneous emission effects, (***f***) includes all effects from (***b***) to (***e***). On the righthand side of each image the particle distribution at $z = 0\ \mu$m is plotted.*

longitudinal velocity of 900 m/s the associated Doppler shift is $\omega_d = -kv = 2.1$ (2π) GHz. This Doppler shift can be compensated by adjusting the laser frequency. The longitudinal velocity distribution adds a complication as the rms velocity spread of 360 m/s gives a Doppler shift spread of 0.8 (2π) GHz. Each velocity component will therefore interact with a different effective detuning and a different effective focusing potential. We will therefore first model our system as a monochromatic beam with longitudinal velocity of 900 m/s and discuss the effects of having multiple velocity components in a real thermal beam at the end of this paragraph.

The longitudinally monochromatic atom beam we now use in our system will not suffer from chromatic aberrations upon focusing, we can therefore use our hollow beam as a lens to obtain basic insight into the focusing process. We can investigate effects of beam collimation, spherical aberrations and magnetic sub-states in the lensing regime. To this end we have investigated the focusing of a monochromatic atom beam of 10 μm diameter with a longitudinal speed of 900 m/s and a transverse velocity spread with a FWHM of 0.3 m/s, whose atoms are uniformly distributed over all magnetic sub-states. We have found an optimum within the limits described at the start of this section for the settings w_0 =10 μm, $P_0 = 1$ W and $\Delta = 250$ (2π) MHz and $z_i = 10$ mm. The results are shown in Figure 6.5 $\mathbf{f}$. This beam is focused most tightly in the plane $z = 0$ mm, where it factually is more in a channeling regime than a simple focusing regime. To obtain the focused atom beam size, we fitted the atom density distribution with a Gaussian profile and used the FWHM as the beam-size. For this beam the size is 1.1 μm. From these results it is clear that in a realistic lensing scheme even without chromatic aberration, a 10 μm atom beam cannot even be focused to sizes less than 1 μm.

To obtain information on the various effects that cause the large focus size, we have performed the same modelling with identical laser field settings but changing the magnetic state effects, transverse velocity distribution and beam size. In Figure 6.5$\mathbf{a}$ we show the results for an atom beam of only 1 μm diameter, without transverse velocity, without magnetic state effects. This beam is focused most tightly in the plane z = -3.0 mm to a size of $FWHM = 3.2$ nm . In Figure 6.5$\mathbf{b}$ the incoming atom beam is increased to a 10 μm diameter, resulting in an smallest focus at z = -3.0 mm with a size of $FWHM = 0.56$ μm. The effect of spherical aberrations is thus a major influence on the final size. Figures 6.5$\mathbf{c}$ and $\mathbf{d}$ are identical to Figures 6.5$\mathbf{a}$ and $\mathbf{b}$ but a transverse velocity spread with a FWHM of 0.3 m/s is added to the incoming atoms beams, corresponding to a Doppler cooled beam. These beams are now focused most tightly in the plane z = 0 mm, where the beam is more in a channeling regime. The sizes are $FWHM = 0.16$ μm and 0.78 μm respectively. By approximating the focusing potential in the plane $z = 0$ by a quadratic potential, we find that there the focal distance of our optical lens is 0.3 mm. As our atom beam has a divergence of 0.3 mrad, we should expect a minimum focus size of 90 nm, on the order of the size we found for an incoming beam of 1 μm diameter. The diverging beams will also suffer more from spherical aberrations, as the beam size is increased before real focusing starts. It should be noted that the focus size of both 1 μm and 10 μm atom beam increases by nearly the same absolute amount, but that for the small incoming beam the relative effect is about 40x larger. In Figure 6.5$\mathbf{c}$ and $\mathbf{d}$ magnetic sub-states

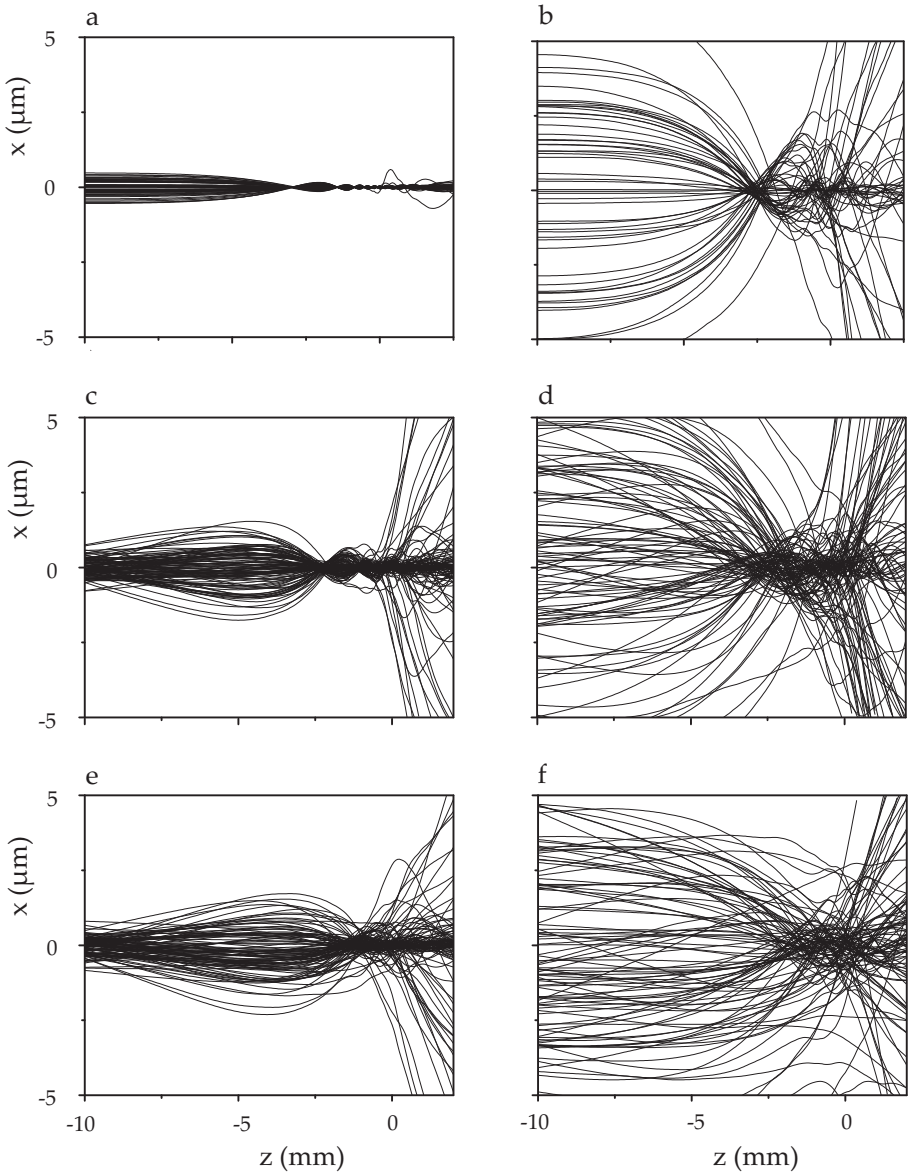

Figure 6.5: *Overview of using a hollow beam potential as a lens. The lefthand images have an incoming beam of 1 μm diameter, the righthand images have a 10 μm diameter incoming beam. In* **a** *and* **b** *the atom beam has no transverse velocity and no magnetic states, in* **c** *and* **d** *the atom beam has a transverse velocity distribution, in* **e** *and* **f** *the atom beam has both transverse velocity distribution and magnetic state effects.*

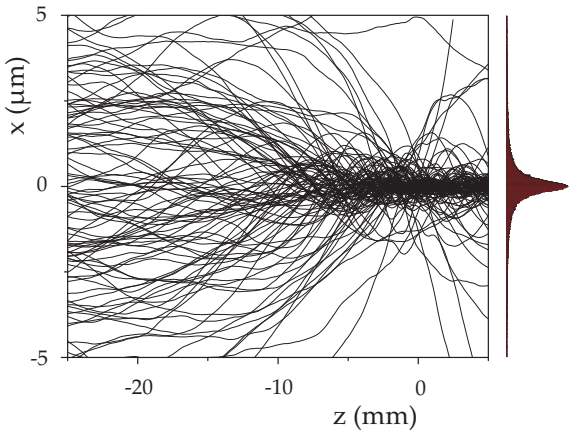

Figure 6.6: *Optimal focusing of a 900 m/s atom beam in a hollow beam funnel. On the left the particle trajectories are shown, on the right the particle distribution in the focus. The light field has a waist of 20 μm, a power of 1 W, a detuning of 150 (2π) MHz and an interaction length of 25 mm.*

are not yet taken into account and all Clebsch Gordan coefficients are assumed to be 1. In Figure 6.5**e** and **f** the atoms are uniformly distributed over all magnetic substates and the focusing potentials have the associated Clebsch Gordan coefficients. These beams too are focused most tightly in the plane z = 0, where they have sizes of 0.27 μm and 1.1 μm. We conclude that the hollow beam potential is not suitable as a lens for 10 μm atom beams mainly because of spherical aberrations, while magnetic state effects further decrease the effectiveness of the lens significantly. The collimation of the incoming beam is only a major effect for incoming beams much smaller than the proposed 10 μm.

As it is not possible to focus a 10 μm beam adiabatically to a size of less than 100 nm, even without taking chromatic aberrations into account, we consider the addition of a damping force in the form of laser cooling. We have added transverse Doppler cooling to our model, based on two pairs of counter-propagating beams with a detuning of $\Gamma/2$, each beam having a saturation parameter $s_0 = 1$. The best result we have obtained in this cooling regime after scanning the parameter range described in the beginning of this section is an atom beam focused to a FWHM of 0.55μm in which only 8.5% of all particles are focused to a radius of 100 nm. The particle trajectories and the focused particle density distribution is shown in Figure 6.6. The settings for the light field are $w_0 = 20$ μm, $P_0 = 1$ W, $\Delta = 150$ (2π) MHz and $z_i = 25$ mm. It is clear that cooling in the funnel improved the focus size compared to the lensing regime, but it is still far off the desired 100 nm radius.

However, the dipole potential well created in the focusing scheme of figure 6.6 is very steep; the well has a Doppler energy level $\hbar\Gamma/2$ at a 36 nm radius, so the Doppler cooled beam is apparently not isothermally compressed. In the focus the average transverse kinetic energy of all particles within a 1 μm radius in the focus has actually

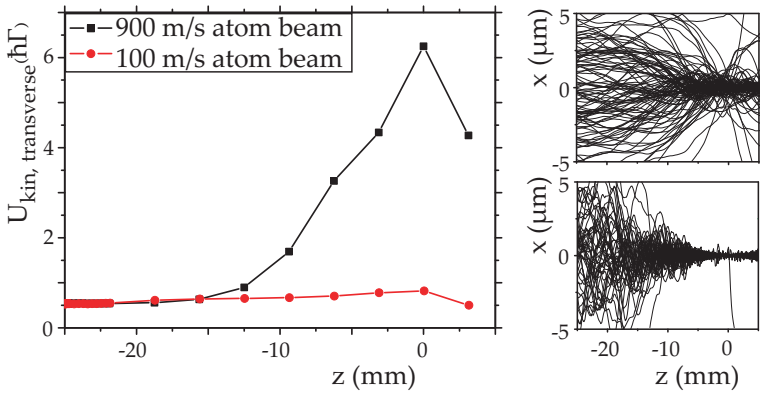

Figure 6.7: *Left: Average transverse kinetic energy of atoms in beams of 900 m/s (black boxes) or 100 m/s (red dots) focused by a hollow beam light field with a waist of 20 μm, a power of 1 W, a detuning of 150 (2π) MHz and an interaction length of 25 mm. Right: particle trajectories for 900 m/s beam(top) and 100 m/s beam (bottom)*

increased to 6.3 $\hbar\Gamma$. To obtain a better insight in the heating and cooling effects, we plot the average transverse kinetic energy of all particles within a 1 μm radius as a function of z position. We show this in Figure 6.7 for an atom beam which has a longitudinal velocity of 900 m/s and for an atom beam with longitudinal velocity of only 100 m/s. Both beams start with a transverse velocity distribution of $FWHM =$ 0.3 m/s. The transverse kinetic energy of the fast atom beam rises steeply as the atoms move towards the focus of the light field, indicating that the cooling scheme cannot cool fast enough for isothermal compression to take place.

The slow 100 m/s atom beam can be funneled nearly isothermally as can be seen in Figure 6.7. In this figure the atom trajectories are also shown. This reveals an improved compression for the slow beam, which is compressed to a size of $FWHM =$ 108 nm. However, using a slow beam seriously complicates the setup and will limit practical application and is therefore outside the scope of this article.

There are several mechanisms that contribute to the heating we see in Figure 6.7. First there is the focusing itself, which according to Liouville's theorem will increase the momentum distribution by a factor 50 if the spatial distribution is decreased by that factor in a conservative potential. Another important heating mechanism is stimulated diffusion due to dressed state changes. In the optical funnel, the decay rate Γ_{21} of the dressed ground state to the dressed upper state is not negligible. If atoms would be focused to the position where the dipole shift is $\Gamma/2$, the decay rate is still $\Gamma_{21} = 2.8\ (2\pi)$ kHz. At a longitudinal velocity of 900 m/s and a interaction length of 25 mm atoms reside in the interaction region for 28 μs. This means that about half of the atoms will undergo a state change to the upper dressed state, even when they reside at the edge of the area to which we hope to focus them. These dressed state changes will lead to stimulated diffusion. The effect of a dressed state change can be drastic as is shown in Figure 6.8. Here two trajectories are shown, of atoms star-

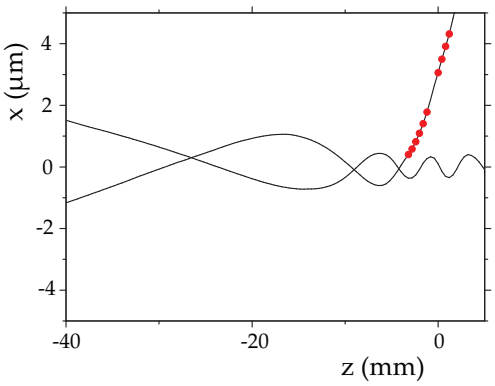

Figure 6.8: *Effects of atom dressed state change on trajectory in a hollow beam potential. The dotted parts of the line indicate the areas where the atom is in the higher state.*

ting in the confined ground state. One of the two atom has a dressed state change and is then completely expelled from the focusing region. This makes it clear that the simple assumptions made in the theory sections on the focusing power of the potential are heavily altered because of the heating due to stimulated diffusion in these steep potentials.

The significant difference in heating because of dressed state changes by slow or fast beams can be understood by considering two elements, firstly that fast atoms will move to areas of higher light intensity and secondly the fact that heating in steep potentials has a positive feedback mechanism inducing more heating. The optical potentials of focused hollow beams have equipotential lines that are not parallel to the incoming atom beam, the longitudinal speed and longitudinal kinetic energy therefore determine to which extent an atom can move to areas of high potential and thus high light intensity. In Figure 6.7 it is visible that up to the point $z =$ -15 mm, the transverse kinetic energy in both fast and slow beams is nearly identical. However, the particle trajectories show that the slow atoms are already being focused to the centre region whereas fast atoms are on average more away from the central axis in areas of higher intensity and higher potential. In these areas the chance of dressed state changes are higher as can be seen in Equation 6.5. As dressed state changes leads to stimulated diffusion and thus heating, atoms can move even further into areas of higher intensity. This again increases the chance of dressed state changes thus this feedback mechanism stimulates the heating tremendously. In the near isothermal compression of the slow beam in Figure 6.7, cooling is not just balancing the heating effects, but also preventing heating effects to increase as atoms are compressed to areas of low light intensity.

It is clear that the cooling within a hollow beam setup with fast atoms is not sufficient to cool fast atoms to a Doppler temperature and isothermally compress the atom beam. In reality the cooling will even be less effective, as the dipole shift of the atoms due to the hollow beam, will decrease the effect of the cooling beams. To

have an indication of this effect, we can apply cooling in our model only to particles that are in a region where the dipole shift is less than $\Gamma/2$. We now obtain a beam that has a FWHM of 1.3 μm, as heating effects are now less damped by cooling. This means that optimising the focusing regime as discussed in the beginning of this section gives comparable results as a realistic funneling regime. For slow beams of 100 m/s the localized cooling is less detrimental, a 100 m/s beam can still be focused to a 0.17 μm beam. This shows clearly that the realistic cooling schemes give little effect for fast beams.

So far we have not modelled real thermal beams in our calculations, but monochromatic beams with a velocity comparable to the most likely velocity of a thermal beam. Even these idealized fast beams do not give good results. We will not investigate the effects or the inclusion of longitudinal velocity distribution as these will lead to additional problems with chromatic aberration and issues with the Doppler shift. Schemes based on blue detuned hollow systems not based on co-propagating laser beams but consistent of crossing beams have been proposed [106], to circumvent the problem of Doppler shifts, but these are beyond the scope of this article.

We have shown that slow beams can be focused. Slow atom beams have fewer issues with longitudinal velocity spread as they are usually produced by decelerating fast beams, which results in rather monochromatic slow beams. The schemes that produce a slow atom beam are outside the scope of this article.

6.7 Axicon

In the previous section we have discussed the focusing potential of a hollow beam light field, of which we have shown that it is not particularly suited to funnel thermal atom beams. Only for slow beams could Doppler cooling provide sufficient cooling of the transverse temperature to allow for optimal funneling towards the potential minima. We will therefore investigate a second light field configuration: the axicon, as discussed in section 6.3. This configuration allows for much longer interaction regions, as can be clearly seen in Figure 6.9, where we show the region where local potential energy is $\hbar\Gamma/2$ over the ground state energy at the heart line. The hollow beam potential has a narrower focus than the axicon, but the hollow beam diverges greatly, whereas the axicon focus hardly diverges over the entire interaction region.

The main problem of the axicon configuration is that we are focusing towards an area of maximum intensity, so that heating effects will be a bigger issue, as increased intensity leads to increased spontaneous emission and dressed state changes. A second problem is that, in the high intensity focusing region, cooling will be difficult. For the hollow beam scheme Doppler cooling in the dark focusing region is a reasonable option, as the region where the level shift is less than $\hbar\Gamma/2$ is large as can be seen in Figure 6.9. For the axicon configuration cooling will be difficult as the central region has shifted dressed energy levels and cooling schemes will require

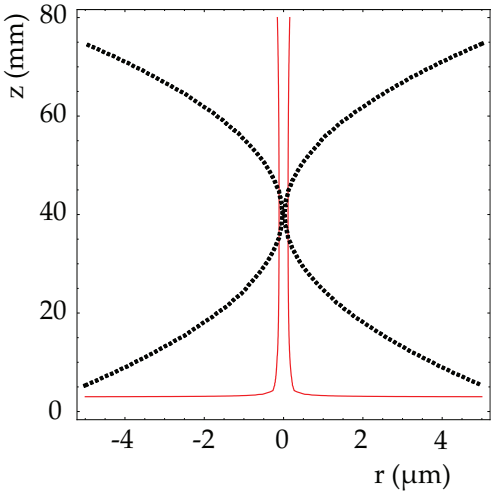

Figure 6.9: *Equipotential lines for the energy level of the ground state particle that is $\hbar\Gamma/2$ over the (z-dependent) ground state energy at the heart line for a hollow beam (black dashed) focused at $z = 0.04$ m of $w_0 = 20$ μm, $P = 1$ W, $\Delta = 150\ (2\pi)$ MHz and an axicon field (red solid line) configuration of $w_0 = 80$ mm, a $P = 1$ W, a $\Delta = 4\ (2\pi)$ GHz.*

an extension of our model to a complicated multi-colour dressed atom picture, which we have not attempted to create.

To obtain insight into the focusing potential of the axicon configuration, we first modelled the system with global Doppler cooling, not taking into account any effects of the level shifts. Optimising the setting of the detuning, incoming beam waist and power leads to the result shown in Figure 6.10, giving nice focusing results. The incoming laser beam has a waist $w_0 = 80$ mm, allowing for 80 mm of interaction length. The laser field has further settings $P = 1$ W, $\Delta = 4\ (2\pi)$ GHz . The atom beam is a 10 μm thermal atom beam with a transverse Doppler energy, which is focused to a $FWHM = 0.13$ μm, thereby focusing 40.6% of all particles within a 100 nm radius.

Comparing the optimal settings for the laser beam in the hollow beam and the axicon configuration shows clear differences, which we investigate by comparing the Rabi frequency Ω with the detuning Δ. For the hollow beam this ratio is $|\Omega/\Delta| \simeq 10^5$ at the points of maximum intensity, and $|\Omega/\Delta| \simeq 1/4$ for the position where the energy levels are shifted by $\hbar\Gamma/2$. For the axicon $|\Omega/\Delta| \simeq 1$ at the maximum intensity and this value is hardly changed on the position where the energy level is shifted by $\hbar\Gamma/2$ from the values on the heart line. From Equations 6.4, 6.3 and 6.5, we thus find that in the high intensity regions of the hollow beam, dressed ground states have a high content of excited state, high rates of dressed state changes and thus generate much spontaneous diffusion. In the optimal axicon configuration, the high detuning suppresses these effects to minimize the heating due to spontaneous diffusion in the high intensity focusing region.

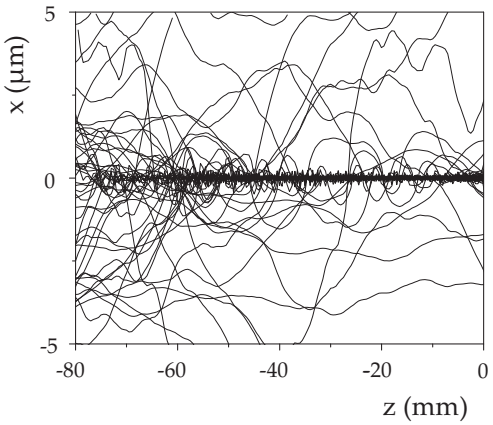

Figure 6.10: *Particle trajectories of a 10 μm atom beam in a axicon light field with waist of 8 mm, a power of 1 W, a detuning of -4 (2π) GHz, with global Doppler cooling.*

The optimisation of the axicon light field shows promising results assuming a global cooling, but as discussed in the start of this section that will be practically impossible. We therefore look at more realistic alternatives. Cooling of the central focusing region is difficult, as the cooling of dressed states requires a multi-colour dressed atom cooling picture. To have an upper limit of the possibilities we investigate the situation where we Doppler cool atoms in the central region where the energy shift of the dressed ground state is less than $\hbar\Gamma/2$ relative to the global minimum. It should be noted that this region is much smaller than the region depicted in Figure 6.9, where the energy level is relative to the local z-dependent minimum, in fact it is a volume of about 0.1 μm radius and 3 mm length along the central axis, nearly negligible compared to the size of the focusing field. This cooling setup leads to a poorly focused beam of $FWHM = 2.2$ μm, only focusing 0.7% of all particles within a 100 nm radius. The second localized cooling option is to cool only outside the central region, in the positions where the dipole shift is less than $\hbar\Gamma/2$ relative to the zero field level. This area is larger but it excludes the central area of about 0.5 μm radius from the central axis. As this scheme does not cool in the area where atoms are focused, it leads to a poorly focused beam of $FWHM = 1.5$ μm, only focusing 1.5% of all particles within a 100nm radius. Localized cooling schemes thus do not provide an option for funneling.

Further options to avoid the complicating presence of multiple light fields, are the spatial or temporal switching of cooling and focusing fields. Since the first would require a complex setup, we propose the rapid temporal switching of cooling and focusing light fields. When switching the focusing field on and off, atoms undergo a change from undressed states to dressed states. We implement this by projecting the ground and excited state upon the dressed states (Equation 6.4) and using a Monte Carlo approach to determine the new state. This leads to additional heating effects, as atoms can be transferred to an excited state, before re-entering the focusing potential. By applying a delay time longer than the lifetime of the excited state

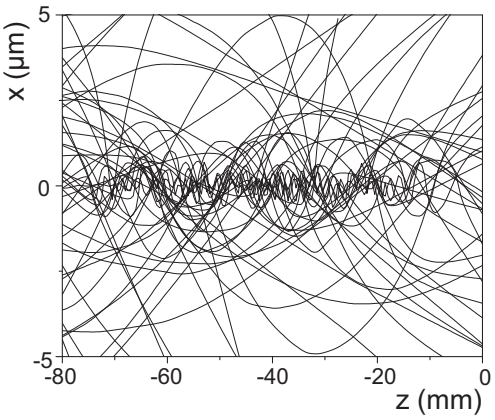

Figure 6.11: *Particle trajectories of a 10 µm atom beam in a configuration of switching focusing and Doppler cooling fields. The switch frequency is 0.66 (2π) MHz, $t_{\mathrm{cool}} = 70$ ns, $t_{\mathrm{focus}} = 110$ ns, $t_{\mathrm{delay}} = 60$ ns. The axicon light field has waist of 8 mm, a power of 1 W, a detuning of 4 (2π) GHz.*

without any fields present before turning on the focusing field, most particles will return to the ground state.

This setting obviously introducing many more parameters to the focusing scheme. We have applied this scheme only to the potential optimised for global cooling, as presented before. After optimizing the switching frequency and within each period the cooling time, the focusing time and the delay time, we find an optimum for a switching frequency of 0.66 (2π) MHz, a cooling time of $t_{\mathrm{cool}} = 70$ ns, a focusing time of $t_{\mathrm{focus}} = 110$ ns and a delay time of $t_{\mathrm{delay}} = 60$ ns, which are all longer than the natural upper state lifetime of 32 ns. This setting focuses the atom beam to a $FWHM = 0.31$ μm and focuses 2.0% of all particles within a 100nm radius; an overview of particle trajectories is given in Figure 6.11.

Comparing Figure 6.11 to Figure 6.10, where global cooling is assumed, it is obvious that in the time switching situation the atom beam is focused to a broader feature but that the beam also has a much larger background. The peak flux within 100 nm is only 25 times higher than the background flux at 5 μm radius, which could be a problem for any application of a focused beam to write structures. Switching cooling and focusing fields seems not to be a very promising solution to the cooling problem.

Concluding we can state that the axicon geometry is a promising focusing tool, if one would be capable of including a cooling scheme. However, such a scheme cannot be implemented using a localized cooling scheme or by switching cooling and focusing fields in the time domain.

6.8 Conclusions

In this article we have investigated the options of creating focused beams of sub-100 nm sizes from 10 μm sized thermal atom beams. Within the scope of this article, investigating blue detuned hollow TEM01* beam and red detuned axicon field configurations, we have found that it is not possible to create sub-100 nm sized atom beams. The main problem is the lack of suitable cooling schemes, which are sufficiently fast and applicable in conjunction with the focusing light fields. We have shown that using slowed atom beams can provide usable options for focusing as well as only using small capture ranges. The practical limit of laser power, poses a limit on focusing options and future increases in available laser power could provide better options for focusing schemes.

Appendix A: Axicon field

Equation 6.15 describes the electric field of the incoming laser beam:

$$\vec{E}_{incoming} = E_0 \cdot \mathrm{e}^{-r^2/w_0^2} \cdot (\hat{x} + i\hat{y}) \cdot \mathrm{e}^{ikz} \cdot \mathrm{e}^{-i\omega_L t}. \tag{6.15}$$

All light rays are assumed to represent a plane wave. In the plane of reflection, the direction of the light ray is defined by the angle ϕ between the light ray and the x-axis in the plane, as shown in Figure 6.2. The electric field of the reflected light ray is:

$$\begin{aligned} \vec{E}_{reflected} = E_0 \quad &\cdot \quad (-i\hat{x}\sin\phi + i\hat{y}\cos\phi + \hat{z}) \cdot \mathrm{e}^{-z^2/w_0^2} \\ &\cdot \quad \mathrm{e}^{ik(\hat{x}\cos\phi + \hat{y}\sin\phi)} \cdot \mathrm{e}^{-i\omega_L t} \cdot \mathrm{e}^{-i\phi}. \end{aligned} \tag{6.16}$$

The term $\mathrm{e}^{-i\phi}$ is a consequence of the circular polarization of the incoming light field. The r-dependence of the Gaussian incoming beam leads to a z-dependence after reflection.

The total field after reflection can be obtained by one-dimensional integration over the plane waves, leading to the following expression for the electrical field in a point (x, y, z) in the axicon:

$$\vec{E}(x, y, z) = \int_0^{2\pi} \vec{E}_{reflected}(z, \phi) d\phi. \tag{6.17}$$

After insertion of Eq.6.16 in Eq.6.17 the integral can be evaluated, leading to an expansion in J_0 and J_1 Bessel functions. For the chosen polarization, there is cylindrical symmetry in the result for the electric field vector except for a phase factor. As a result, the expression for the intensity of the light inside the axicon depends only on r and z:

$$\begin{aligned} I_{ax}(r, z) \quad \propto \quad & |E(rx, y, z)|^2 = C_0 z e^{-2z^2/w_0^2} \\ & \cdot \left\{ J_1^2(kr) \left(1 + \frac{1}{(kr)^2} \right) + \left(J_0(kr) - \frac{J_1(kr)}{kr} \right)^2 \right\}. \end{aligned} \tag{6.18}$$

Normalization of the intensity leads to determination of the constant C_0. Finally, the light intensity inside the axicon can be written as:

$$\begin{aligned} I_{ax}(r, z) \quad = \quad & \frac{2P_0 k}{w_0^2} \cdot z \mathrm{e}^{-2(\frac{z}{w_0})^2} \times \\ & \left\{ J_1^2(kr) + \left(J_0(kr) - \frac{J_1(kr)}{kr} \right)^2 + \frac{J_1^2(kr)}{(kr)^2} \right\}, \end{aligned} \tag{6.19}$$

Appendix B. Effects of parameters on hollow beam focusing

To understand the effects of the various parameters and to show that our setting is indeed optimal, we scan each parameter over a broad range while keeping the other parameters constant. These results are shown in Figures 6.12 - 6.15. All these figures show the FWHM of the beam in focus, modelled as if it were a Gaussian beam. Secondly the percentage of all particles that is focused to a radius of less than 100 nm is given. These two parameters give different information, as particles can move outside the funnel due to heating effects, leading to e.g. a tight focus of little particles.

In Figure 6.12 we can see that power is the limiting factor; if more power would be available, tighter focusing would be possible, however even at 2 W of power, the focused beam still focuses only 14% of all particles within a 100 nm radius and the beam-size has only decreased to $FWHM = 0.4$ μm. For high power it is clear from the particle trajectories, that heating effects are significant at high powers. If much more power would be available, a larger detuning would then be preferable to diminish heating effects.

In Figure 6.13 the influence of focus waist is shown. The influence of the waist on focusing is threefold. It gives the typical size of the potential, but it also gives the height of the potential as light intensity is inversely dependent on the square of the waist. Finally it also defines the Rayleigh length and thus has influence on the length over which the interaction between atom and light field is effective. As we have seen that maximal power and thus maximum intensity is optimal, a small waist will also be preferable. Only for a waist smaller than 20 μm, thus for a Rayleigh length smaller than 3 mm, the focusing is hindered by a lack in effective interaction length. This is clearly visible in the lower left image.

In Figure 6.14 we see the influence of the interaction length on the focusing. The optimum around 25 mm is robust, but at much shorter interaction length, the particles cannot be focused fast enough as can be seen in the lower left image. For long interaction lengths, the divergence of the atom beam is a problem. In the lower right image the particle trajectories show that there is hardly any focusing over the first 30 mm, while the divergence of the atom beam of 0.3 mrad will increase the beam size by 9 μm. This obviously hinders the focusing.

We show the effects of detuning in Figure 6.15. Here we see that a detuning of 150 (2π) MHz gives the smallest focus, but a detuning of 100 (2π) MHz gives slightly more particles within a 100nm radius. At small detuning, dressed state changes are likely, which leads particles out of the funnel. At large detuning, the lens strength is diminished, leading to a large focus, but as there is hardly any heating all particles remain in the focus.

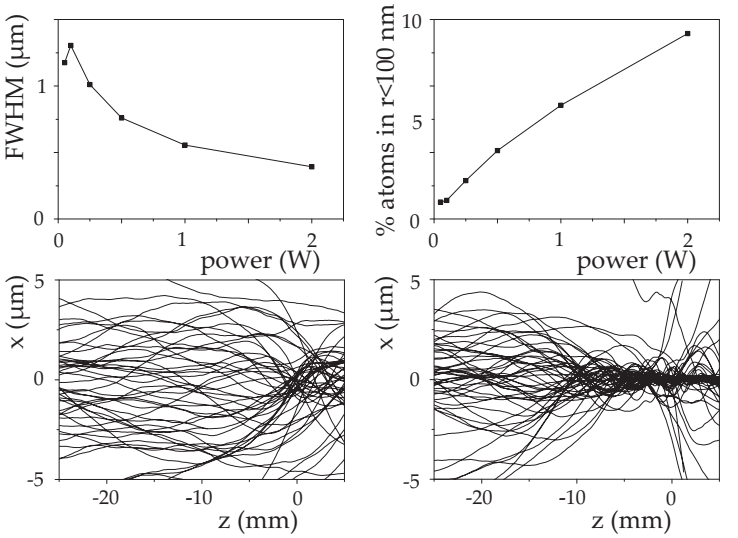

Figure 6.12: *Effect of used power on focusing of the atom beam. In the top left the FWHM of the focused beam as function of power is given, in the top right the percentage of all particles that is focused to a radius of less than 100 nm is given. In the bottom typical focusing trajectories for minimum power (0.05 W) and maximum power (2 W) is shown.*

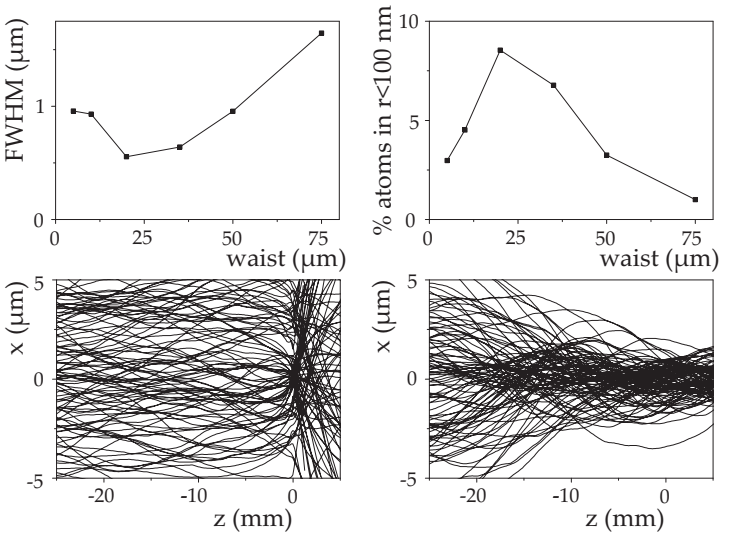

Figure 6.13: *Effect of laser waist size on focusing of the atom beam. In the top left the FWHM of the focused beam as function of waist size is given, in the top right the percentage of all particles that is focused to a radius of less than 100 nm is given. In the bottom typical focusing trajectories for minimum waist (5 μm) and maximum waist (75 μm) is shown.*

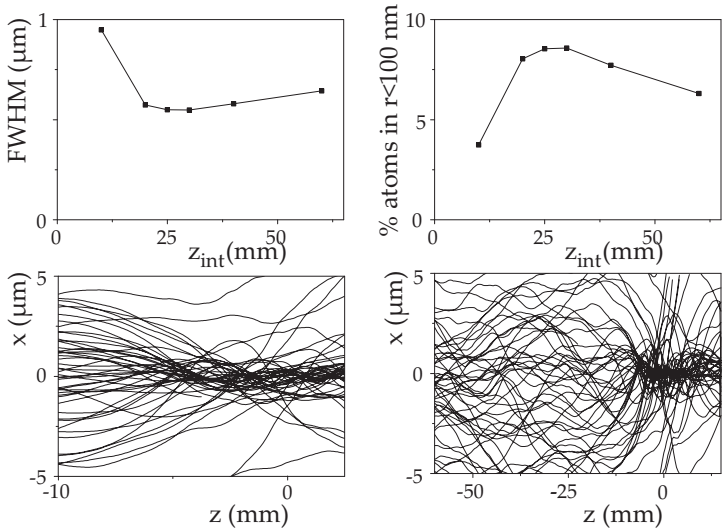

Figure 6.14: *Effect of the interaction length (z_{int}) of the atom beam in the optical potential. In the top left the FWHM of the focused beam as function of z_{int} is given, in the top right the percentage of all particles that is focused to a radius of less than 100 nm is given. In the bottom typical focusing trajectories for minimum (10 mm) and maximum (60 mm) interaction length is shown.*

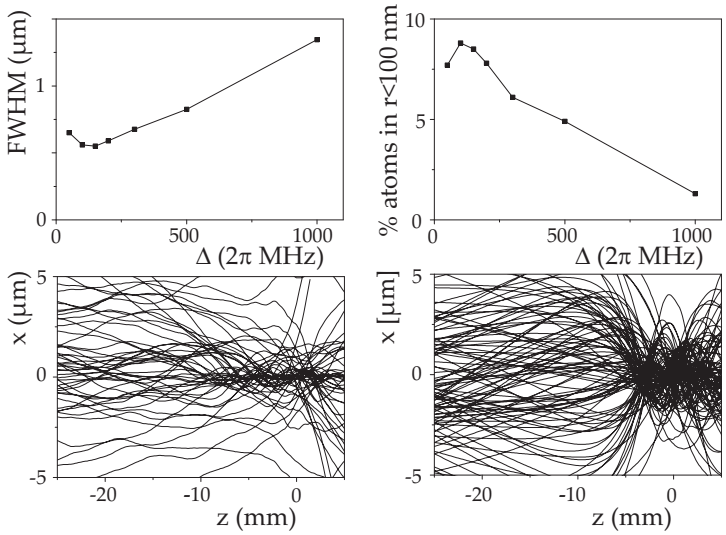

Figure 6.15: *Effect of used detuning on focusing of the atom beam. In the top left the FWHM of the focused beam as function of detuning is given, in the top right the percentage of all particles that is focused to a radius of less than 100 nm is given. In the bottom typical focusing trajectories for minimum detuning (50 (2π) MHz) and maximum detuning (1 (2π) GHz) is shown.*

Bibliography

[1] F.E. Wagner, S. Haslbeck, L. Stievano, S. Calogero, Q.A. Pankhurst, K.P. Martinek, Nature **407**(6805), 691 (2000)

[2] R. Frisch, Z.Phys. A **86**, 42 (1933)

[3] D.J. Wineland, R.E. Drullinger, F.L. Walls, Phys. Rev. Lett. **40**, 1639 (1978)

[4] S. Andreev, V. Balykin, V. Letokhov, V. Minogin, JETP Lett. **34**, 442 (1981)

[5] E.L. Raab, M. Prentiss, A. Cable, S. Chu, D.E. Pritchard, Phys. Rev. Lett. **59**, 2631 (1987)

[6] M.H. Anderson, J.R. Ensher, M.R. Matthews, C.E. Wieman, E.A. Cornell, Science **269**(5221), 198 (1995)

[7] G. Timp, R.E. Behringer, D.M. Tennant, J.E. Cunningham, M. Prentiss, K.K. Berggren, Phys. Rev. Lett. **69**(11), 1636 (1992)

[8] R. Gupta, J.J. McClelland, Z.J. Jabbour, R.J. Celotta, Appl. Phys. Lett. **67**(10), 1378 (1995)

[9] U. Drodofsky, J. Stuhler, T. Schulze, M. Drewsen, B. Brezger, T. Pfau, J. Mlynek, Appl. Phys. B, Lasers Opt. **65**, 755 (1997)

[10] E. Jurdik, G. Myszkiewicz, J. Hohlfeld, A. Tsukamoto, A.J. Toonen, A.F. van Etteger, J. Gerritsen, J. Hermsen, S. Goldbach-Aschemann, W.L. Meerts, H. van Kempen, T. Rasing, Phys. Rev. B **69**(20), 201102 (2004)

[11] D. Jürgens, A. Greiner, R. Stützle, A. Habenicht, E. te Sligte, M.K. Oberthaler, Phys. Rev. Lett. **93**(23), 237402 (2004)

[12] R. Gupta, J.J. McClelland, P. Marte, R.J. Celotta, Phys. Rev. Lett. **76**(25), 4689 (1996)

[13] M. Mützel, S. Tandler, D. Haubrich, D. Meschede, K. Peithmann, M. Flaspöhler, K. Buse, Phys. Rev. Lett. **88**(8), 083601 (2002)

[14] M. Mützel, M. Müller, D. Haubrich, U. Rasbach, D. Meschede, C. O'Dwyer, G. Gay, B. Viaris de Lesegno, J. Weiner, K. Ludolph, G. Georgiev, E. Oesterschulze, Appl. Phys. B, Lasers Opt. **80**(8), 941 (2005)

[15] J.J. McClelland, R.E. Scholten, E.C. Palm, R.J. Celotta, Science **262**(5135), 877 (1993)

[16] R.W. McGowan, D.M. Giltner, S.A. Lee, Opt. Lett. **20**(24), 2535 (1995)

[17] R. Ohmukai, S. Urabe, M. Watanabe, Appl. Phys. B, Lasers Opt. **77**, 415 (2003)

[18] E. te Sligte, B. Smeets, K.M.R. van der Stam, R.W. Herfst, P. van der Straten, H.C.W. Beijerinck, K.A.H. van Leeuwen, Appl. Phys. Lett. **85**(19), 4493 (2004)

[19] G. Myszkiewicz, J. Hohlfeld, A.J. Toonen, A.F.V. Etteger, O.I. Shklyarevskii, W.L. Meerts, T. Rasing, E. Jurdik, Appl. Phys. Lett. **85**(17), 3842 (2004)

[20] K.S. Johnson, J.H. Thywissen, N.H. Dekker, K.K. Berggren, A.P. Chu, R. Younkin, M. Prentiss, Science **280**(5369), 1583 (1998)

[21] P. Engels, S. Salewski, H. Levsen, K. Sengstock, W. Ertmer, Appl. Phys. B, Lasers Opt. **69**, 407 (1999)

[22] S. Petra, L. Feenstra, W. Hogervorst, W. Vassen, Eur. Phys. J. D **27**, 83 (2003)

[23] F. Lison, H.J. Adams, D. Haubrich, M. Kreis, S. Nowak, D. Meschede, Appl. Phys. B, Lasers Opt. **65**, 419 (1997)

[24] B. Smeets, R.W. Herfst, L.P. Maguire, E. Te Sligte, P. Van Der Straten, H.C.W. Beijerinck, K.A.H. Van Leeuwen, Appl. Phys. B, Lasers Opt. **80**, 833 (2005)

[25] B. Smeets, Magnetic nanostructures by atom optics. Ph.D. thesis, Eindhoven University of Technology (2005)

[26] E. te Sligte, Atom lithography of iron. Ph.D. thesis, Eindhoven University of Technology (2004)

[27] R. Skomski, *Simple models of magnetism* (Oxford University Press, 2008)

[28] Getzlaff, *Fundamentals of Magnetism* (Springer-Verlag, 2008)

[29] S.S.P. Parkin, M. Hayashi, L. Thomas, Science **320**(5873), 190 (2008)

[30] T. Hansch, B. Couillaud, Opt. Commun. **35**(3), 441 (1980)

[31] J.C.J. Koelemeij, W. Hogervorst, W. Vassen, Rev. Sci. Instrum. **76**, 033104 (2005)

[32] W. Demtroder, *Laser spectroscopy, basic concepts and instrumentation* (Springer-Verlag, 1980)

[33] B. Smeets, R. Bosch, P. van der Straten, E. te Sligte, R. Scholten, H. Beijerinck, K. van Leeuwen, Appl. Phys. B, Lasers Opt. **76**, 815 (2003)

[34] P. Atkins, *Atkins Physical Chemistry* (Oxford University Press, 2002)

[35] D.R. Lide, *CRC Handbook of Chemistry and Physics* (CRC Press/Taylor and Francis, 2009)

[36] D. Meschede, H. Metcalf, J. Phys. D **36**(3), R17 (2003)

[37] V. Balykin, P. Melentiev, Nanotechnologies in Russia **4**, 425 (2009)

[38] M.D. Hoogerland, J.P.J. Driessen, E.J.D. Vredenbregt, H.J.L. Megens, M.P. Schuwer, H.C.W. Beijerinck, K.A.H. van Leeuwen, Appl. Phys. B, Lasers Opt. **62**, 323 (1996)

[39] S. Rehse, R. McGowan, S. Lee, Appl. Phys. B, Lasers Opt. **70**, 657 (2000)

[40] B. Smeets, P. van der Straten, T. Meijer, C. Fabrie, K. van Leeuwen, Appl. Phys. B, Lasers Opt. **98**, 697 (2010)

[41] J. Dalibard, C. Cohen-Tannoudji, J. Opt. Soc. Am. B **2**(11), 1707 (1985)

[42] R.C.M. Bosch, H.C.W. Beijerinck, P. van der Straten, K.A.H. van Leeuwen, Eur. Phys. J.-Appl. Phys. **18**(03), 221 (2002)

[43] W. Anderson, C. Bradley, J. McClelland, R. Celotta, Phys. Rev. A **59**(3), 2476 (1999)

[44] E. te Sligte, K.M.R. van der Stam, B. Smeets, P. van der Straten, R.E. Scholten, H.C.W. Beijerinck, K.A.H. van Leeuwen, J. Appl. Phys. **95**(4), 1749 (2004)

[45] E. Jurdik, T. Rasing, H. van Kempen, C.C. Bradley, J.J. McClelland, Phys. Rev. B **60**(3), 1543 (1999)

[46] J. Zhong, J.C. Wells, Y. Braiman, J. Vac. Sci. Technol. B **20**(6), 2758 (2002)

[47] T.N. Tun, M.H.T. Lwin, H.H. Kim, N. Chandrasekhar, C. Joachim, Nanotechnology **18**(33), 335301 (2007)

[48] A. Nesmeyanov, *Vapor Pressure of the Chemical Elements* (Elsevier Publishing Company, 1963)

[49] R.E. Behringer, V. Natarajan, G. Timp, D.M. Tennant, J. Vac. Sci. Technol. B **14**(6), 4072 (1996)

[50] C. Guillaume, *Invar and elinvar, Nobel Lectures, Physics 1901-1921* (Elsevier Publishing Company, 1967)

[51] C. Guillaume, Comptes Rendus de l'Academie de Sciences **125**, 235 (1897)

[52] Wasserman, *Ferromagnetic Materials: a handbook on the properties of magnetically ordered materials, Volume 5* (Elsevier, 1990)

[53] J. Crangle, G.C. Hallam, Proc. R. Soc. A **272**, 119 (1963)

[54] O.E. Buckley, L.W. McKeehan, Phys. Rev. **26**, 261 (1925)

[55] R. Skomski, D. Sellmeyer, *Handbook of Advanced Magnetic Materials, volume 1* (Springer Verlag, 2006)

[56] K. Sumiyama, Y. Nakamura, Phys. Status Solidi (A) **81**(2), K109 (1984)

[57] J.H. He, H.W. Sheng, P.J. Schilling, C.L. Chien, E. Ma, Phys. Rev. Lett. **86**, 2826 (2001)

[58] Y. Kakehashi, T. Uchida, M. Yu, Phys. Rev. B **56**, 8807 (1997)

[59] J.W. Freeland, I.L. Grigorov, J.C. Walker, Phys. Rev. B. **57**, 80 (1998)

[60] B. Glaubitz, S. Buschhorn, F. Bruessing, R. Abrudan, H. Zabel, J. Phys. Condens. Matter **23**(25), 254210 (2011)

[61] M. Shaw, J. Gelorme, N. LaBianca, W. Conley, S. Holmes, IBM J. Res. Dev. **41**, 81 (1997)

[62] M. Corporation. Su8 datasheet

[63] A. Prenen, Polymeric microfilters by interference holography. Ph.D. thesis, Eindhoven University of Technology (2009)

[64] J. Goldstein, R. Ogilvie, Trans.Metall.Soc.AIME **233**, 2083 (1965)

[65] Gradmann, *Handbook of magnetic materials, Volume 7* (Elsevier, 1993)

[66] R. Cowburn, J. Phys. D: Appl. Phys. **33**, R1 (2000)

[67] D. Tulchinsky, M. Kelly, J. McClelland, R. Gupta, R. Celotta, J. Vac. Sci. Technol. A **16**(3), 1817 (1998)

[68] M. Oberthaler, T. Pfau, J. Phys. Cond. Matt. **15**(6), R233 (2003)

[69] URL `llgmicro.home.mindspring.com/`

[70] J. Oster, M. Kallmayer, L. Wiehl, H.J. Elmers, H. Adrian, F. Porrati, M. Huth, J. Appl. Phys. **97**, 014303 (2005)

[71] A. Sugawara, T. Coyle, G.G. Hembree, M.R. Scheinfein, Appl. Phys. Lett. **70**, 1043 (1997)

[72] S.K. Arora, B.J. O'Dowd, P.C. McElligot, I.V. Shvets, P. Thakur, N.B. Brookes, J. Appl. Phys. **109**, 07B106 (2011)

[73] H.M. Hwang, J.H. Kang, J. Lee, J.Y. Choi, H.H. Lee, Electrochemical and Solid-State Letters **11**(1), K7 (2008)

[74] T. Schmitte, K. Theis-Brohl, V. Leiner, H. Zabel, S. Kirsch, A. Carl, J. Phys. Condens. Matter **14**(32), 7525 (2002)

[75] C. Shearwood, S.J. Blundell, M.J. Baird, J.A.C. Bland, M. Gester, H. Ahmed, H.P. Hughes, J. Appl. Phys. **75**, 5249 (1994)

[76] R.M. Bradley, J.M.E. Harper, J. Vac. Sci. Technol. A **6**, 2390 (1988)

[77] Q.F. Zhan, S. Vandezande, C.V. Haesendonck, K. Temst, Appl. Phys. Lett **91**(12), 122510 (2007)

[78] F. Bisio, R. Moroni, F.B. de Mongeot, M. Canepa, L. Mattera, Appl. Phys. Lett. **89**, 052507 (2006)

[79] F. Büttner, K. Zhang, S. Seyffarth, T. Liese, H.U. Krebs, C.A.F. Vaz, H. Hofsäss, Phys. Rev. B **84**, 064427 (2011)

[80] G.J. Strijkers, J.H.J. Dalderop, M.A.A. Broeksteeg, H.J.M. Swagten, W.J.M. de Jonge, J. Appl. Phys. **86**, 5141 (1999)

[81] Q. Liu, C. Gao, J. Xiao, D. Xue, J. Magn. Magn. Mater. **260**(1-2), 151 (2003)

[82] G.C. Han, B.Y. Zong, P. Luo, Y.H. Wu, J. Appl. Phys. p. 9202 (2003)

[83] J. Swerts, S. Vandezande, K. Temst, C.V. Haesendonck, Solid State Commun. **131**(6), 359 (2004)

[84] V. Ng, J.F. Hu, A.O. Adeyeye, J.P. Wang, T.C. Chong, J. Appl. Phys **91**, 7206 (2002)

[85] Y.P. Zhao, R.M. Gamache, G.C. Wang, T.M. Lu, G. Palasantzas, J.T.M.D. Hosson, J. Appl. Phys. **89**, 1325 (2001)

[86] A.E. LaBonte, J. Appl. Phys. **40**, 2450 (1969)

[87] M. Schneider, S. Mueller-Pfeiffer, W. Zinn, J. Appl. Phys. **79**(11), 8578 (1996)

[88] Y.K. Kim, M. Oliveria, J. Appl. Phys. **74**, 1233 (1993)

[89] A. Hubert, R. Schafer, *Magnetic domains: the analysis of magnetic microstructures* (Springer Verlag, 1998)

[90] M. Klaui, J. Phys.: Cond. Mat. **20**(31), 313001 (2008)

[91] T. Schulze, T. Muther, D. Jurgens, B. Brezger, M.K. Oberthaler, T. Pfau, J. Mlynek, Appl. Phys. Lett. **78**, 1781 (2001)

[92] F. Atoneche, D. Malik, A. Kirilyuk, A.J. Toonen, A.F. van Etteger, T. Rasing, J. Phys.: Conf. Ser. **303**, 012046 (2011)

[93] E. Wolf, *Nanophysics and Nanotechnology* (Wiley, 2004)

[94] I. Utke, P. Hoffmann, J. Melngailis, J. Vac. Sc. Technol. B **26**(4), 1197 (2008)

[95] F. Tantussi, A. Camposeo, M. Alderighi, N. Puccini, E. Andreoni, M. Allegrini, E. Arimondo, F. Fuso, Mat. Sci. Eng. C **27**(5-8, Sp. Iss. SI), 1418 (2007)

[96] V. Natarajan, R.E. Behringer, G. Timp, Phys. Rev. A **53**(6), 4381 (1996)

[97] J. Bjorkholm, R. Freeman, A. Ashkin, D. Pearson, Phys. Rev. Lett. **41**(20), 1361 (1978)

[98] V. Balykin, V. Letokhov, Opt. Commun. **64**(2), 151 (1987)

[99] G. Gallatin, P. Gould, J. Opt. Soc. Am. B **8**(3), 502 (1991)

[100] B. Dubetsky, P. Berman, Phys. Rev. A **58**(3), 2413 (1998)

[101] V. Balykin, V. Klimov, V. Letokhov, J. Physique II **4**(11), 1981 (1994)

[102] J. McClelland, M. Scheinfein, J. Opt. Soc. Am. B **8**(9), 1974 (1991)

[103] V. Balykin, V. Minogin, J. Exp. Theor. Phys. **96**(1), 8 (2003)

[104] S. Petra, K. van Leeuwen, L. Feenstra, W. Hogervorst, W. Vassen, Appl. Phys. B, Lasers Opt. **78**, 133 (2004)

[105] A. Siegman, *Lasers* (Oxford University Press, 1986)

[106] O. Steuernagel, Phys. Rev. A. **79**(1), 013421 (2009)